POLITECNICO DI MILANO
DEPARTMENT OF PHYSICS
DOCTORAL PROGRAMME IN PHYSICS

GROUP-IV TELLURIDES AS A PLAYGROUND FOR ENHANCED PERFORMANCES IN SPIN AND ANGLE-RESOLVED PHOTOEMISSION SPECTROSCOPY

Doctoral Dissertation of:
Luca Nessi

Supervisor:
Prof. Matteo Cantoni

Tutor:
Prof. Riccardo Bertacco

The Chair of the Doctoral Program:
Prof. Marco Finazzi

2020/2021 – XXXIV

Acknowledgements

I thank the Nanomagnetism group of Physics department of Politecnico di Milano for hosting me as Ph.D. student and in particular Prof. Matteo Cantoni, Prof. Riccardo Bertacco and Dr. Christian Rinaldi for the support and the supervision during my studies.

I thank CNR-IOM for the fundings that supported my scholarship and my activities, and the team of the APE beamline at Elettra synchrotron of Trieste.

Finally, I thank Prof. Pietro Gambardella and his team for welcoming me as a visiting student in their group at ETH Zürich laboratories and IDEA League for the IDEA League Student Grant 2021, won with the project *Towards full electric control of magnetism by spin-orbit torque in devices based on the Ferroelectric Rashba Semiconductor GeTe*.

Summary

SPINTRONICS attention in the last two decades was devoted to look for methods to manipulate the magnetisation of ferromagnets alternative to external magnetic fields. The idea to integrate spin functionalities in electronic devices was lead by dimensions scaling and elimination of magnetic stray fields which magnetic writing heads impose severe limitations for. Moreover, with an all-electric system, it is possible to guarantee high energy efficiency. This was initially achieved by spin-transfer torque, i.e., exploiting spin-polarised currents to transfer momentum to orient the magnetisation of ferromagnetic films in magnetic memories. Recently, a new way to control magnetism emerged. It is called spin-orbit torque which, instead, exploits non magnetic materials with large spin-orbit coupling to generate spin currents to be injected in the ferromagnetic layer. A great effort in terms of research in material science was done to identify new appropriate classes of materials for such a scope. This process involved wider areas of fundamental physics and gave the possibility to develop new measurement techniques.

Among all, in 2013, ferroelectric Rashba semiconductors (FERSC) were discovered to possess very intriguing spin properties which can be tuned by means of the ferroelectric polarisation and could represent a valid candidate for spintronic devices. The father compound of this class is germanium telluride, already well-known as phase-change material. In the last years, its properties were widely studied and the interplay between spin transport and ferroelectricity was very recently demonstrated, also at room temperature. This represents an important goal in order to make this material interesting for applications. In general, group-IV tellurides are eligible members for such a class, but the experimental research on other compounds different from GeTe is still unexplored.

This thesis presents two case studies: SnTe and GeTe. Indeed, also SnTe was very well-known to belong to another class of materials, namely topological crystalline insulators. This work tries to shed a new light on this material and to investigate its physics looking for properties which make it a FERSC materials, exploiting the possibility of doping this compound with germanium. This study was conducted from a fundamental point of view, optimising the growth and doping process and performing spectroscopic experiments. The results obtained showed the possibility to observe at room temperature bulk Rashba bands and, indirectly, ferroelectricity. Moreover, opportunely tuning

the Ge concentration, it was demonstrated the possibility to continuously modulate such properties.

While SnTe needed still a fundamental characterisation as a FERSC, previous studies on GeTe allow to exploit it into devices and study its spin transport properties. GeTe films are studied in this work, unveiling the signature of a rich spin texture and showing the presence of non-reciprocal charge transport, validating the glimpsed opportunity to exploit them into devices.

Since the fundamental investigation of such materials passes for a spectroscopic analysis which is unequivocally the most direct way to retrieve their band structure, spin and angle-resolved photoemission spectroscopy was the main technique exploited in this work. Even if the state-of-art of technology in this kind of measurements made a lot of progresses in last years in what regards spin detection, it remains a very time-consuming technique because of the low sensitivity in measuring the spin degree of freedom and the pointwise nature of the current set-ups. In this thesis, a new conception of spin detection is proposed and realised through a prototype device based on a matrix of magnetic free-standing membranes grown on graphene. The deposition process of magnetic materials on ultra-thin graphene monolayers was optimised together with an investigation on the mechanical reliability of such a system. Then, these membranes were characterised both mechanically and from the magnetic point of view.

This could represent a new way to reconstruct the spin dependence of electronic band structure and, thanks to the intrinsic bidimensionality of such a device, a way to drastically speed up this spectroscopic technique and increase its performances. The study of FERSC and other new classes of materials which sustain complex spin textures could benefit from this device which would guarantee an increased resolution of the measurements and a much smaller duration of the experiments under similar conditions of signal-to-noise ratio.

Preface

The present thesis describes part of the work of the author, starting from the beginning of his Ph.D. studies in November 2018 (XXXIV cycle) up to October 2021. The supervisor of the activity was Professor Matteo Cantoni. The results reported in this work were mainly carried out in two research centres. The first one, where the principal part of the work was conducted, is the department of Physics of Politecnico di Milano (Italy) and in particular the nanotechnology research facility Polifab and the associated Nanomagnetism laboratory. The second one is the Department of Materials of ETH Zürich in the laboratory of the Intermag group led by Professor Pietro Gambardella for a period of four months (March 2021 – May 2021 and September 2021).

The Ph.D. activities resulted in the following published works:

[1] S. Varotto, **L. Nessi**, S. Cecchi, J. Sławińska, P Noël, S. Petrò, A. Novati, M. Cantoni, D. Petti, E. Albisetti, M. Costa, R. Calarco, M. Buongiorno Nardelli, M. Bibes, S. Picozzi, J.-P. Attané, L. Vila, R. Bertacco and C. Rinaldi, *Room-temperature non-volatile control of spin-to-charge conversion in the ferroelectric semiconductor GeTe*, Nature Electronics, 4, pages 740–747 (2021), doi: org/10.1038/s41928-021-00653-2.

[2] M. Asa, C. Rinaldi, **L. Nessi**, D. Petti, E. Albisetti, R. Bertacco, and M. Cantoni, *Epitaxy and controlled oxidation of Chromium ultrathin films on ferroelectric BaTiO3 templates*, Journal of crystal growth 558, 126012 (2021), doi: 10.1016/j.jcrysgro.2020.126012.

[3] M. Ghirardello, V. Otero, D. Comelli, L. Toniolo, D. Dellasega, **L. Nessi**, M. Cantoni, G. Valentini, A. Nevin and M. J. Melo, *An investigation into the synthesis of cadmium sulfide pigments for a better understanding of their reactivity in artworks*, Dyes and Pigments, 108998 (2020), doi: 10.1016/j.dyepig.2020.108998.

[4] S. Varotto, **L. Nessi**, S. Cecchi, R. Calarco, R. Bertacco and C. Rinaldi, *Investigation of charge-to-spin conversion in GeTe*, Proc. SPIE 10732, Spintronics XI, 107320C (2018), doi: 10.1117/12.2320502.

And in the following conference contributions:

Sep 2021 Trends in MAGnetism, Cefalù, Italy, oral presentation "Graphene-based ultra-thin magnetic membranes for spin polarimetry";

Dec 2020 Joint European Magnetic Symposia (JEMS 2020), Lisbon, Portugal, oral presentation "Design of a spin filter device with free-standing graphene-based magnetic membranes";

Sep 2020 106° Congresso Nazionale, Società di Fisica Italiana 2020, oral presentation "Spin polarimetry with graphene-based free-standing magentic membranes";

Aug 2019 Joint European Magnetic Symposia (JEMS 2019) Uppsala, Sweden, poster presentation "Free-standing magnetic membranes for spin polarimetry".

Contents

1 Introduction **1**
- 1.1 Motivations . . . 2
  - 1.1.1 Ferroelectric Rashba semiconductors . . . 2
  - 1.1.2 Spin- and angle-resolved photoemission spectroscopy: state-of-art of technology . . . 4
- 1.2 Thesis outline . . . 5

2 Ferroelectric Rashba semiconductors: a theoretical introduction **9**
- 2.1 Ferroelectricity . . . 9
  - 2.1.1 Phenomenology and theory of ferroelectricity . . . 10
- 2.2 Rashba effect . . . 11
  - 2.2.1 Theory of Rashba effect . . . 12
  - 2.2.2 Topological surface states . . . 13
- 2.3 Spin-to-charge interconversion phenomena . . . 13
  - 2.3.1 Spin Hall effect . . . 13
  - 2.3.2 Rashba-Edelstein effect . . . 15
  - 2.3.3 Bilinear magnetoelectric resistance . . . 17
  - 2.3.4 Spin currents to manipulate magnetism: spin-orbit torques . . . 18
- 2.4 Case studies: GeTe and SnTe . . . 19
  - 2.4.1 Germanium telluride . . . 19
  - 2.4.2 Tin telluride . . . 21

3 Interaction of polarised electrons with materials: a survey on spin detectors **23**
- 3.1 Introduction . . . 23
- 3.2 Interactions with matter of a polarised electron beam . . . 25
- 3.3 Spin detectors: a survey . . . 26
  - 3.3.1 Mott detector . . . 27
  - 3.3.2 Very low-energy electron diffraction . . . 28
  - 3.3.3 Very low-energy electron transmission spin detector . . . 28

4 Experimental techniques **31**

4.1 Deposition techniques . . . 31
4.1.1 Molecular beam epitaxy . . . 32
4.1.2 Magnetron sputtering . . . 33
4.2 Fabrication techniques . . . 33
4.2.1 Optical lithography . . . 33
4.2.2 Ion beam etching and contact deposition . . . 35
4.2.3 Devices fabrication recipe: Hall bar geometry . . . 36
4.3 Spin- and angle-resolved photoemission spectroscopy . . . 36
4.4 Magnetoelectric characterisation: harmonic Hall measurements . . . 38
4.5 Magnetic characterisation of free-standing films: Faraday effect set-up . . . 40
4.6 Spin-polarised electron gun . . . 41

5 Spin- and angle-resolved photoemission spectroscopy and bands engineering in Ge-doped SnTe films 45
5.1 Samples growth, preparation and post-treatments . . . 46
5.2 XPS and SARPES measurements on Ge-doped SnTe . . . 48
5.2.1 Doping concentration . . . 48
5.2.2 Mapping the energy band structure . . . 49
5.2.3 Spin-resolved ARPES of bulk Rashba bands and surface states . . . 52
5.3 Discussion . . . 53

6 Design of a two-dimensional spin detector based on free-standing magnetic membranes 55
6.1 Growth of free-standing magnetic films . . . 56
6.1.1 Design of the heterostructure and choice of the materials . . . 56
6.1.2 Deposition parameters . . . 57
6.2 Mechanical reliability analysis . . . 58
6.2.1 Preliminary definitions and parameters of the analysis . . . 58
6.2.2 Discussion . . . 59
6.3 Mechanical characterisation . . . 60
6.4 Magnetic characterisation . . . 63
6.5 Transmission and spin-filtering characterisation . . . 65
6.5.1 Experiment design and definition of the set-up . . . 65
6.5.2 Discussion of transmission measurements . . . 66
6.5.3 Spin filtering characterisation . . . 67
6.6 Conclusions . . . 68

7 Transport properties of GeTe films and heterostructures 71
7.1 Introduction . . . 71
7.2 Samples preparation . . . 72
7.3 Magnetoresistance of GeTe monolayers . . . 72
7.3.1 Measurements . . . 72
7.3.2 Discussion . . . 75
7.4 Conclusions . . . 77

8 Conclusions 79

A Angular dependencies of torques and thermal effects in angle scans 81

A.1 Spin-Orbit torques in angle scans 81
A.1.1 xy scan 82
A.1.2 xz scan 83
A.1.3 yz scan 83
A.2 Thermal effects in angle scans 83

B Decapping protocol for group-IV tellurides capped with tellurium **87**
B.1 Introduction 87
B.2 Decapping protocol 87

Bibliography **93**

CHAPTER 1

Introduction

In his Nobel lecture, given in December 1946, Wolfgang Pauli described how the bases for a theory of the 'hidden rotation' of the electron were designed in his mind together with the exclusion principle. This idea laid the foundations of modern quantum physics.

> In the autumn of 1924 I [...] proposed the assumption of a new quantum theoretic property of the electron, which I called a 'two-valuedness not describable classically'. [...] The physicists found it difficult to understand the exclusion principle, since no meaning in terms of a model was given to the fourth degree of freedom of the electron. The gap was filled by Uhlenbeck and Goudsmit's idea of electron spin, which made it possible to understand the anomalous Zeeman effect simply by assuming that the spin quantum number of one electron is equal to 1/2. [5] [6]

Actually, even when the electron spin was still unknown, the interplay between spin and orbital degrees of freedom was already studied and it intrigued condensed matter scientists since the beginning of the century [7]. Only in the late Twenties, relativistic quantum mechanics really gave the insights for the microscopic comprehension of spin and of *spin-orbit coupling* (SOC). In modern material science, this is now understood to be ubiquitous and to underlying a wide spectrum of phenomena, e.g., magnetocrystalline anisotropy, anomalous Hall effect, Rashba effect, topological states, Majorana fermions [8, 9, 10, 11], involving all kind of materials, from semiconductors, to standard metals, to insulating oxides, to more exotic state of matter.

The boost received by the development of new technologies in governing thin films depositions and in tayloring the composition of new materials opened new horizons rapidly passing from *spintronics* (i.e., spin-electronics) to *spin-orbitronics* (i.e., electronics which exploits spin-orbit interaction-based effects). This new field has intensified its interest in materials with strong SOC, glimpsing the possibility to engineer them by integrating the conventional electronics with spin functionalities. The most challenging proposals cover the fields of storage and computing. The former deals with the replacement of magnetic fields in writing information in magnetic memories (typically composed by nanomagnets

with a writeable magnetisation [12]) which suffer of scaling and relative slow operations via *current-induced spin torques* produced by injecting a spin current into a ferromagnetic material, moving to fully electrically controlled systems [13].[1] From the computing perspective, the aim consists in the replacement of CMOS technology with a *scalable spintronic logic device* that operates via spin–orbit transduction for an all-in-one platform with enhanced performances in terms of scalability and energy consumptions, paving the way towards exploiting it in new computing paradigms such as *artificial intelligence*, as proposed by Intel in 2019 [1, 16].

In the framework scientific and technological challenge, the work which follows deals with a new class of materials, namely ferroelectric Rashba semiconductors (FERSC), strongly promising for these applications and, in general, for spin-orbitronics. They are a recently discovered family of materials [17] and they are object of an investigation which spans from a more fundamental perspective of material science and solid state physics, even stimulating the development of new instrumentation technology in order to deeply characterise them, to a very applicative field, in which they are raised to new materials for beyond-CMOS computing [1].

The challenge faced in this work is twofold. The study of the properties of FERSC and the tayloring of their functionalities oblige to cope with the state-of-art of performances of spectroscopic experiments: the engineering of materials electronic band structures goes hand in hand with the validation through spin- and angle-resolved photoemission spectroscopy (SARPES) experiments. Hence, a fundamental investigation of FERSC materials (in particular, GeTe and SnTe) is presented, including the growth process, the structural and the spectroscopic characterisation. At the same time, the proof-of-concept of a new paradigmatic way to access to the spin resolution of energy bands is sketched and realised by exploiting graphene-based free-standing magnetic membranes.

In this introductory chapter, the breakthrough introduced by FERSC is discussed in terms of their multi-functional properties and their potential applications in spin-orbitronics. Then, the role of spin detection in spectroscopic experiments and its importance in modern material science is faced as well, and the necessity of a new technological solution is briefly discussed.

1.1 Motivations

1.1.1 Ferroelectric Rashba semiconductors

Phenomenology

Rashba effect is a momentum-dependent splitting of the energy bands according to their spin polarisation [10, 18], generated by the presence of SOC and a *structural inversion asymmetry* (SIA). In particular, it generates bands which have the peculiarity of the so-called *spin-momentum locking*, i.e., the angle between the momentum and the spin of the electrons is constant and fixed. This property gives a unique opportunity to control the spin transport in materials or heterostructures that sustain it.

[1] Spin torques can be differentiated into two families, *spin transfer torques* (STT) and *spin-orbit torques* (SOT). While in the former a spin-polarised current flows into the ferromagnetic material, in the latter the spin current absorbed by the ferromagnet is generated from a current which flows in the material with large SOC. In the present discussion, the interest is in the second set of torques. They guarantee better performances in terms of shorter switching times, endurance of the devices (since the charge current does not directly flow into the ferromagnetic junction) and employment of different class of magnetic materials (e.g., magnetic insulators [14] and antiferromagnets [15]).

Giant bulk Rashba effect actually was not born with FERSC. In 2011, the polar semiconductor BiTeI was proved to display large splitted bulk Rashba bands [19, 20]. The fundamental role of ferroelectricity and the actual discovery of FERSC is more recent [17, 21]. In 2013, with density functional theory (DFT) calculations a giant bulk Rashba effect was found to be sustained by electronics bands in ferroelectric GeTe. It was also shown that the chirality of the spin texture of such an effect was strictly related to the ferroelectric polarisation vector direction, both theoretically and experimentally [22]. After that, several other materials joined this new class. In particular, oxide perovskite Bi_2WO_6 [23] and in general group IV monochalcogenides [24], e.g., SnTe.

The peculiar features of FERSC are summed up in figure 1.1. Their properties can be listed as:

- *Ferroelectricity* consists in the displaying of a fixed polarisation vector even without the presence of an external electric field. As in the case of ferromagnets, the ferroelectricity is displayed up to a critical temperature, known as Curie temperature (for the case of GeTe is predicted to be $\sim 720\,\mathrm{K}$). This is due to a lattice distorsion which provokes the space inversion symmetry breaking of the crystal which is the fundamental ingredient to have:

- *Rashba bulk bands splitting*, i.e., the spin splitting of energy bands according to the momentum of electrons. Two sub-bands are created which carry an opposite spin chirality (as pictorially shown in the bottom-left circle).

- They are typically narrow-gap *semiconductors* ($\epsilon_{\mathrm{gap}} = 0.8\,\mathrm{eV}$ for GeTe) and they can be epitaxially grown on silicon and hence they are compatible with standard electronics.

Applications

Exploiting again the comparison with ferromagnets, a metastable state such as the non-zero remanent polarisation in ferroelectrics, naturally makes FERSC interesting for *memory* elements [25]. Furthermore, the intrinsic link between polarisation and chirality of the spin texture makes them valuable candidates for spin-to-charge conversion processes. In particular, the generation of a spin current from a charge one can be a direct consequence of the presence of Rashba bands through the so-called Rashba-Edelstein effect (REE) [26] or can be produced by the presence of large SOC through spin Hall effect (SHE) [27][2].

As previously discussed, the control of the magnetisation through an electric current via current-induced spin torques represents a very hot topic nowadays. The prototypical heterostructures ferromagnet (FM)/normal metal (NM), hystorically made by Co/Pt [30], can be replaced by the structure FM/FERSC. Thanks their ferroelectric behaviour, this can overcome the lack of electric tunability of the writing process in FM/NM, i.e., the possibility to taylor the conversion process (between charge and spin) in magnitude and sign. This was demonstrated for two-dimensional electron gases (2DEG) at the $LaAlO_3/SrTiO_3$ interface [31] and also for more complex heterostructures involving ferroelectric materials and heavy metals [32]. FERSC represent a unique possibility to join the non-volatility of

[2] Actually, there is a plethora of phenomena which allow to generate spin currents in materials, they can arise in several situations, e.g., by pumping with polarised light [28] or by applying thermal gradients [29]. For the cases treated in this work one can rely on two phenomena, namely the Rashba-Edelstein effect and the spin Hall effect.

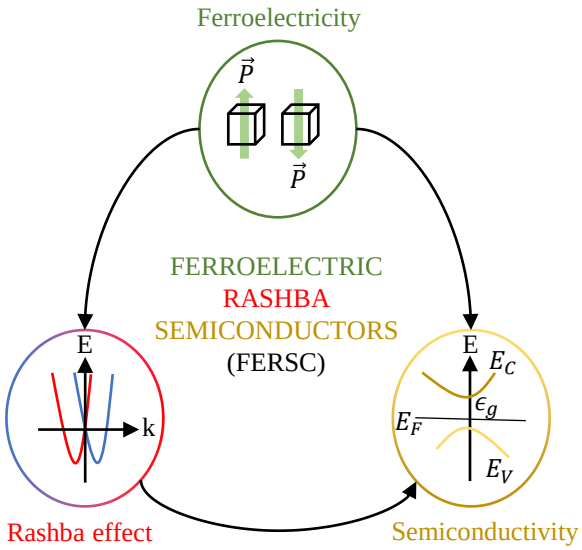

Figure 1.1: *Ferroelectric Rashba semiconductors display the coexistence of ferroelectricity, giant bulk Rashba effect and they are typically narrow-gap semiconductors. Both the spin and the charge transport are influenced by ferroelectricity.*

such a mechanism to a semiconductive platform which is – on the contrary with aboved-mentioned systems – easily integrable with standard silicon electronics.

A deeper investigation is needed both from the fundamental and the applicative point of view. In this thesis these two aspects will be faced, firstly dealing with materials beyond the prototypical father compound (GeTe), in particular focusing on SnTe, then trying to exploit GeTe, whose fundamental properties have been already quite well understood both theoretically and experimentally, in a device deeply studying their physics.

1.1.2 Spin- and angle-resolved photoemission spectroscopy: state-of-art of technology

The motivations presented in the previous section imply the capability to deal with the spin degree of freedom of electrons and to manage their transport in solids. It becomes of fundamental importance the knowledge of the electronic distribution in such materials, together with the relation between spin and momentum of the carriers. As mentioned above, SARPES represents the most powerful tool which allows a complete investigation of the set of quantum numbers useful to describe electronic bands in solids. Moreover, the surface sensitivity of such a technique makes it a highly demanded tool to investigate nanostructures. The actual limiting factor in this kind of experiment is the poor efficiency of spin detectors which makes the measurements incredibily time-consuming.

Several mechanisms were exploited in spin detectors in order to retrieve the spin polarisation of an incoming beam of electrons. They span from Mott scattering [33], based – again – on spin-dependent scattering caused by SOC, to very low energy electron diffraction (VLEED), which relies on exchange interaction-based scattering in ferromagnetic

materials [34, 35, 36].

Two factors actually matter in speeding up such an experiment. One is the capability to measure a large asymmetry A, given a certain spin polarisation P, which is quantified by a parameter called *Sherman function* S defined as $S := A/P$ and a figure of merit (FOM) defined as $\eta := S^2 I/I_0$ (where I is the intensity of scattered electrons, while I_0 is the intensity of incident ones). The other one is the possibility to work with several channels in parallel, namely to acquire electrons with different k vectors at the same time. Nowadays, VLEED represents the state-of-art of spin detectors. The Sherman function is $S \sim 0.40$ with respect to the one in Mott scattering which is $\sim 0.1 - 0.2$, the FOM is drastically larger, passing from 1×10^{-4} for Mott detectors to $\sim 2 \times 10^{-2}$ for VLEED [35]. The development of a multichannel VLEED (MCVLEED) achieved in ref. [37], allowed to push the efficiency of the detection $\sim 5 \times 10^5$ times larger than a Mott detector.

Nevertheless, MCVLEED solution implies a great effort in managing the deflection of electrons with a suitable system of electrostatic lenses, which makes the experimental apparatus very complex. In 2017, Övergaard *et al.* proposed in ref. [38] a solution based – as VLEED is – on exchange interaction, but exploiting *transmission* of electrons instead of reflection (in the following this methodology will be called *very low electron energy transmission spin detection* (VLEETSD)). The idea is briefly sketched in figure 1.2 (a). This translates in the development of free-standing magnetic membranes, recalling to the seminal works of Siegmann and co-workers [39, 40]. The transmission of electrons depends on the relative direction between their spin and the membrane magnetisation. The idea was implemented building up a matrix of membranes which can allow for a multichannel detection, as for the case of MCVLEED. The crucial role of lithography is evident: in order to fabricate such a device, it is necessary to exploit processes commonly used for microelectromechanical systems (MEMS), with sacrificial layers and selective etching processes. The whole workflow becomes far from straightforward and the device presents al lot of drawbacks. Despite these difficulties, this two-dimensional spin detector is calculated to push forward the efficiency of the detection, with a FOM of $\sim 1 \times 10^2$ (in figure 1.2 (b) is plotted the FOM of different detectors employed nowadays (VLEED, SPLEED, MOTT) with respect to the operational energy, compared to predicted new two-dimensional one).

From the previous discussion, it is very clear that the route for a new efficient way to do spin detection is drawn, but a practical realisation is still missing. This is the challenge which is tackled in the work that follows.

1.2 Thesis outline

This chapter gave a general introduction to a very new field of research which lays its foundations in fundamental physics, but has strict applications to material science and modern electronics, linking them indissolubly. The most important results which motivated this work were reviewed, trying to underlining how spin-orbitronics is affecting the work of many scientists, from spectroscopists to engineers. The aim of this thesis is ambitious: it tries to cover this chain, drawing a line between two extremities, using a novel platform, such as group-IV tellurides as a playground.

The work is organised as follows:

- Chapter 2 gives a general theoretical overview on ferroelectric Rashba semiconduc-

Spin detectors				
Technique	Figure of merit (FOM) (η)	Sherman function (S)	Operation voltage	Ref.
Mott	$\sim 3.0 \times 10^{-5}$	$0.1 - 0.2$	$100 - 150\,\mathrm{kV}$	[33]
Mott	$\sim 1.6 \times 10^{-4}$	$0.15 - 0.25$	$20 - 25\,\mathrm{kV}$	[41]
SPLEED[a]	not reported	0.27 ± 0.03	$100\,\mathrm{V}$	[42]
VLEED	7.0×10^{-4}	0.2	$4 - 6\,\mathrm{V}$	[34]
VLEED	2.2×10^{-3}	$0.23 - 0.3$	$13.5\,\mathrm{V}$	[43]
VLEED	3.3×10^{-2}	0.5	$6\,\mathrm{V}$	[36]
2D SPLEED	1.7 (# of channels not reported)	0.43	$26\,\mathrm{V}$	[44]
MCVLEED	57.7 (with 6,786 channels)	0.225	$6\,\mathrm{V}$	[37]
VLEETSD	67.2 (with 11,106 channels)	0.41	$2 - 10\,\mathrm{V}$	[38]

Table 1.1: *Performances of state-of-art spin detectors with different detection techniques, namely: Mott, SPLEED, VLEED and VLEETSD. For further comparison, see figure 1.2 (b).*

[a]SPLEED stays for *spin-polarised low energy electron diffraction*. These kind of detectors operates through SOC interaction-based scattering too, but the energy of the electrons impinging on them is an order of magnitude higher with respect to VLEED detectors.

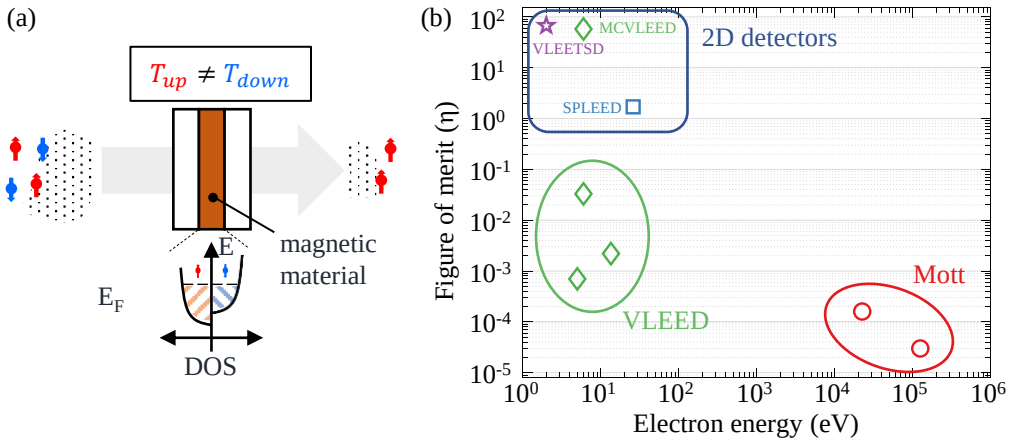

Figure 1.2: *(a) Sketch of the physical principle underlying the idea for new generation spin detectors, based on the idea presented in ref. [38]. The transmission of an electron beam impinging on a magnetic ultra-thin target depends on the relative direction between the spin of the electrons and the magnetisation vector of the active layer; (b) Comparison between state-of-art spin detectors, according to the operation voltage used and the respective figure of merit η.*

tors and their principal properties, namely ferroelectricity, bulk Rashba physics and spin-momentum locking, focusing on GeTe and SnTe, as pratical examples;

- Chapter 3 provides an introduction to spin filtering properties of magnetic thin films and their application in modern spin detectors, reviewing the state-of-art of this kind of technology;
- Chapter 4 describes the main experimental techniques employed during the thesis, i.e. the deposition and fabrication techniques of magnetic membranes, the set-ups for their magnetic characterisation and for their spin filtering characterisation; the fabrication of GeTe-based devices and the set-up for magnetoelectric transport measurements; the deposition of SnTe films and their spectroscopic characterisation;
- Chapter 5 focuses on the spin and angle-resolved photoemission spectroscopy experiments made on Ge-doped SnTe. The optimisation of the growth and the doping of thin films is discussed and the demonstration of the presence at room temperature of bulk Rashba bands and ferroelectricity is provided;
- Chapter 6 moves from the motivations arisen in chapter 5 to present the design of a two-dimensional spin detector employable in SARPES experiments based on ultrathin free-standing magnetic membranes using from 2 to 8 graphene monolayers as mechanical support. All the workflow of deposition and characterisation is covered;
- Chapter 7 deals with a more applicative topic, after a fundamental investigation on SnTe compounds and a technological proposal of a new spin detector concept presented in previous chapters, it reviews transport experiments made on GeTe-based samples, the father compound of group-IV tellurides, glimpsing the possibility to have an electric probe as a counterpart to spectroscopic experiments to have information about the spin texture of this kind of materials. In this sense, bilinear magnetoelectric resistance phenomenon is found to be of the order of 0.02% at 1.3 T;
- Chapter 8 draws the conclusions of the work and gives some future perspectives.

CHAPTER 2

Ferroelectric Rashba semiconductors: a theoretical introduction

This chapter is organised to provide a general overview on FERSC, in particular focusing on the properties investigated in chapters 5 and 7. In section 2.1 ferroelectricity is briefly discussed, while in section 2.2 the theory of Rashba effect is presented. Section 2.3 deals with spin-to-charge interconversion phenomena and related effects when these materials are employed in heterostructures. Finally, section 2.4 presents the two materials of interest of this thesis, namely GeTe and SnTe, reviewing their properties and the studies performed so far regarding their physics.

2.1 Ferroelectricity

Ferroelectricity deals neither with iron nor with magnetism but, when it was discovered in 1920 [45, 46] in Rochelle salts, it resembled very much ideas of ferromagnetism. The presence of a spontaneous polarisation vector which can be reversed by an external applied electric field instigated the curiosity in understanding new phase transition phenomena and to study what can be seen as an electric counterpart of ferromagnetism. In the Forties, the ferroelectric perovskite $BaTiO_3$ was discovered [47]. It displayed a robust ferroelectricity with a simpler crystal structure than Rochelle salts. This encouraged more theoretical works and the discovery of new materials showing similar features. The application to devices came soon: ferroelectric oxides became ceramics used for capacitors and they are even now key materials for this industry. In the Eighties, the possibility to produce thin films boosted their applications in integrated circuits [48] and in 2000 the first text about the ferroelectric memories appeared, opening the path to ferroelectric random access memories. In the last twenty years the interest in ferroelectric materials grew exponentially, developing an *ad hoc* quantum theory based on Berry phase [49, 50],

exploiting them in memories [25] and combining different disciplines and phenomena, such as ferroelectricity and magnetism leading to the world of *multiferroics* [51, 52], up to the discovery of exotic phenomena, such as polar skyrmions [53]. Ferroelectricity is a structural property of materials always accompanied by piezoelectricity and pyroelectricity. This link makes them also interesting for microelectronic devices such as microelectromechanical systems (MEMS), sensors, transducers and actuators [54, 55]. Because of their continuously tunable resistance, ferroelectric materials are also employed in neuromorphic computing applications, which is nowadays a very active field of research [56].

2.1.1 Phenomenology and theory of ferroelectricity

The presence of a *remanent polarisation* and a *coercive field* are the key properties which identify a ferroelectric material (they are depicted in figure 2.1(b)). Again in analogy with ferromagnetism, a phase transition can be observed between a state with a *spacial symmetry breaking* due to polarisation and a non polar state which is symmetric and paraelectric. The temperature which this transition happens at is called *Curie temperature*[1].

The polarisation is defined as the dipole moment per unit volume for a given charge distribution. This dipole arises from the structural distorsion of the lattice and the consequent displacement of ions, which breaks the symmetry and gives a permanent polarisation. One of the largest value of polarisation was observed in $BiFeO3$, with $\sim 150\,\mu C/cm^2$ [58].

From this discussion, it is clear that only non-centrosymmetric crystal groups can sustain a non-vanishing polarisation. Two main causes can distort the lattice of a crystal: external force and temperature. The presence of a polarisation due to an external stress is called *piezoelectricity*, while if the polarisation appears when the temperature changes the phenomenon is called *pyroelectricity*. Hence, given the 32 crystalline classes, 21 of them are non-centrosymmetric, 20 of which are piezoelectric. Among them, only 10 are pyroelectric. In this last class, there are some ferroelectric materials (see figure 2.1 (a)).

As mentioned in the introduction, the modern theory of polarisation is based on a quantum object called Berry phase, which has its foundations in *topology* [59].[2] Avoiding to introduce the intricacy of such a theory, it is possible to describe ferroelectricity from a macroscopic point of view through a mean-field theory, called Landau-Devonshire theory [60, 61]. It can be sketched as follows. Considering the thermodynamic state of a bulk ferroelectric material, the array of variables which characterise the system is composed by: temperature (T), polarisation (P) and external electric field (E). With the assumption that P is an independent variable, one can write the free energy in the neighborhood of the ferroelectric-paraelectric transition as follows:

$$f_{\mathrm{P}} = \frac{1}{2}a(T)P^2 + \frac{1}{4}b(T)P^4 - EP, \tag{2.1}$$

where an analytical free energy function is assumed. The expansion is trucated to the fourth order and only even terms are taken into account not to have a sign-dependent free

[1] Analogously to ferromagnets the Curie temperature spans over a very wide range, from few Kelvin to thousands of Kelvin [57].

[2] It is possible to show that polarisation should not written in terms of absolute values, but only *changes in polarisation* actually matter and are comparable to experimental results. If one treats the electronic states in the framework of quantum mechanics with Wannier functions, it is possible to realise that the polarisation difference directly depends on the *Berry phase* developed by the evolution of wave functions of the electronic states. This provides an elegant formalism and a theoretical framework useful also for density functional theory calculations.

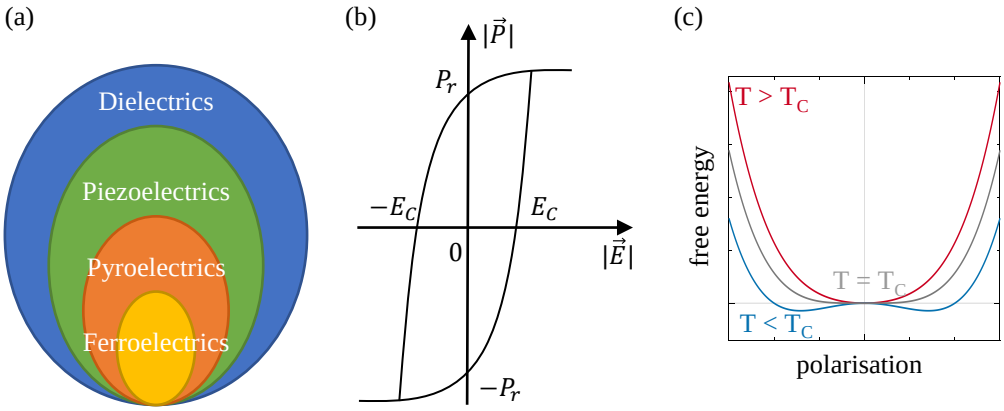

Figure 2.1: *(a) Classes of materials with nested sets of dielectrics, piezoelectrics,pyroelectrics and ferroelectrics; (b) Sketch of the salient properties of ferroelectrics, the hysteresis loop shows the remanent polarisation P_r and the coercive field E_c; (c) Eq. 2.4 for different values of the Curie temperature and for $E = 0$.*

energy. The equilibrium configuration is obtained with the minimisation of the thermodynamic potential, so imposing: $\partial f_P/\partial P|_{P=P_0} = 0$. This gives:

$$E = a(T)P_0 + b(T)P_0^3. \tag{2.2}$$

The simplest hypothesis that can be done on the coefficients appearing in 2.1 is the following:

$$\begin{cases} a(T) & = a_0(T - T_C) \\ b(T) & = b_0 \end{cases}, \tag{2.3}$$

where the sign of a_0 is positive, while the sign of b_0 is considered positive as well, according to the fact that one is facing a second-order phase transition. Hence the free energy reads:

$$f_P = \frac{1}{2}a_0(T - T_C)P^2 + \frac{1}{4}b_0P^4 - EP. \tag{2.4}$$

In figure 2.1(c) is plotted f_P for different values of T_C at remanence ($E = 0$). For $T > T_C$ the system is paraelectric with just one minimum for $P = 0$. For $T < T_C$ one can see two minima with a polarisation different from zero which represent the two metastable states with remanent polarisation. This simple theory cannot address the limit for $T = T_C$.

This theory represents a useful starting point which can explain the salient physics of ferroelectrics and it is useful to address the main features of the materials studied in this work.

2.2 Rashba effect

In a crystal with inversion symmetry, moving electrons obey to time-reversal symmetry, hence $E(\uparrow, \mathbf{k}) = E(\uparrow, -\mathbf{k})$ and $E(\uparrow, \mathbf{k}) = E(\downarrow, -\mathbf{k})$. These equalities lead to a degeneracy between spin up ($\uparrow$) and spin down ($\downarrow$) bands, i.e., $E(\uparrow, \mathbf{k}) = E(\downarrow, \mathbf{k})$, for a fixed k vector. In quantum mechanics this is known as Kramers theorem [62]. This happens, for example, for a light metal such as copper [63] (see figure 2.2(a)). This degenaracy

can be lifted by a symmetry breaking. In particular, two different cases may arise. When *bulk inversion asymmetry* (BIA) is present, i.e., when one considers a crystal without an inversion point, this gives rise to the so-called Dresselhaus effect [64] (discovered in zinc blende structures). When *structural inversion asymmetry* (SIA) is present due to, for example, an asymmetric interface or a polarisation vector, Bychkov-Rashba (or more simply just Rashba) effect arises [18]. This effect can appear both for surface and bulk states, e.g., in the prototypical case of Au(111) (see figure 2.2(a)) surface states [63] or, as discussed in chapter 1, in polar materials such as BiTeI [19] or GeTe[21]. Both these effects have the consequence to give a spin polarised character to energy bands, which becomes of fundamental importance for spin-orbitronic applications. In the following of this section, the attention is focused only on Rashba effect, since in FERSC Dresselhaus-like behaviour was not reported.

2.2.1 Theory of Rashba effect

The foundations of Rashba effect lays in relativistic quantum physics. This effect is intimately related with spin-orbit coupling (SOC). The simplest system exhibiting Rashba effect is a two-dimensional electron gas (2DEG) with an applied electric field in the out-of-plane direction, i.e., $\mathbf{E} = E\mathbf{e}_z$ (being $\mathbf{e}_z$ the unitary vector pointing along the z direction), which accounts for the symmetry breaking (see top panel of figure 2.2(b) for the notation). If one considers a free and independent electron moving in an electric field, from relativistic dynamics it experiences a magnetic field in its frame of motion, as a consequence of Lorentz transformations. This field is called *spin-orbit field*. Hence, the spin of the electron interacts with this magnetic field through Zeeman interaction. It is possible to write down the Hamiltonian governing the system as follows:

$$H_{\mathrm{SO}} = -\frac{e\hbar}{4m^2c^2}\mathbf{E}\cdot(\boldsymbol{\sigma}\times\mathbf{p}), \tag{2.5}$$

where m is the electron mass, c is the speed of light, $\mathbf{p}$ is the momentum of the electron and $\boldsymbol{\sigma}$ is the vector of the Pauli matrices. Manipulating eq. 2.5, it is usually defined a Rashba parameter $\boldsymbol{\alpha}_{\mathrm{R}}$ that quantifies the strength of the Rashba effect and a Rashba Hamiltonian H_{R}, as follows:

$$H_{\mathrm{R}} = \alpha_{\mathrm{R}}\left(\mathbf{e}_z\times\mathbf{k}\right)\cdot\boldsymbol{\sigma}. \tag{2.6}$$

Solving the usual eigenvalues problem $\det(H_{\mathrm{R}} - E_{\pm}\mathcal{I}) = 0$, it is possible to show that the dispersion relation for Rashba bands has the form of:

$$E_{\pm}(k) = \frac{\hbar^2k^2}{2m} \pm \alpha_{\mathrm{R}}|k|, \tag{2.7}$$

where two sub-bands appear. It is important to notice that, as evident from the Hamiltonian in equation 2.6, the spin and the k vector of electrons are always perpendicular to each other. This phenomenon is known as *spin-momentum locking* and is of key importance in transport properties of such a systems. In the top panel of figure 2.2(b) eq. 2.7 in the E-k space is plotted, while in the bottom panel the Rashba contour unveiling spin-momentum locking in k space is displayed.

2.2.2 Topological surface states

Spin-momentum locking is a feature present also in other classes of materials, beyond Rashba systems. Topological insulators (TI), discovered in 2007 by Fu, Kane and Mele [65, 66], attracted immediately a fervid interest in spintronics. The recent study of ref. [67] shows that roughly 27% of the materials in Nature have topological properties and 11% of them are topological insulators. They are insulators in the sense that they have a bulk band gap which prevents conduction, but they present at the same time a conductive surface, due to the presence of *topological surface states* (TSS). These states are topological in the sense that they are protected by symmetry. This means that electron-electron interactions and transformations of the Hamiltonian which do not imply symmetry breaking do not modify such states. The theory of TSS does not allow to exploit a toy model as for the case of Rashba and goes beyond the scope of this work.

The Hamiltonian describing TSS resembles the form of the Rashba one, viz,

$$H_{\mathrm{TSS}} = \pm\hbar v_{\mathrm{F}} \left(\mathbf{e}_z \times \mathbf{k}\right) \cdot \boldsymbol{\sigma}, \tag{2.8}$$

where v_F is the Fermi velocity. The dispersion is linear as for a Dirac cone and it presents a certain chirality (i.e., the sense of circulation of the spins) which changes sign below and above the Dirac point, where the bands intersect each other. When surface states lay in the energy gap and they are crossed by the Fermi level, charge and spin transport can be treated as for a Rashba system (a prototypical example is shown in figure 2.2(c)).

It is noteworthy to mention that there are different classes of TI. In particular, standard TI, such as Bi_2Se_3 [68], $Bi_{1-x}Sb_x$ [69] or α-Sn [70] are protected by time-reversal symmetry and belong to the so-called $\mathbb{Z}_2$ class. It was discovered by Fu [71] a further class of TI, known as *topological crystalline insulators* (TCI) whose surface states are protected by crystal point group symmetry. This phenomenon can arise in three-dimensional topological insulators which have sixfold ($\mathcal{C}_6$) rotational symmetry, such as SnTe [72], which is investigated in this thesis.

2.3 Spin-to-charge interconversion phenomena

Since the seminal work of Karplus and Luttinger [73] about the anomalous Hall effect, it was very clear that SOC was an unavoidable ingredient in order to allow spin-dependent transport. SOC systems, such as FERSC, Rashba interfaces and heavy metals, became the ideal platform to generate, govern and detect spin currents.

In this section, the main physical mechanisms which allow the generation of spin currents are briefly overviewed. The focus is on spin Hall effect (SHE) in section 2.3.1 and Rashba-Edelstein effect (REE) in section 2.3.2. They are the mechanisms of interest in FERSC. In section 2.3.3 it is discussed a magnetoresistance effect know as bilinear magnetoelectric effect (BMER), which is a direct consequence of the presence of Rashba states, while in section 2.3.4 is described how spin currents can interact with ferromagnets through spin-orbit torques (SOT) in order to electrically control their magnetisation. This is of fundamental importance from the point of view of applications in real devices.

2.3.1 Spin Hall effect

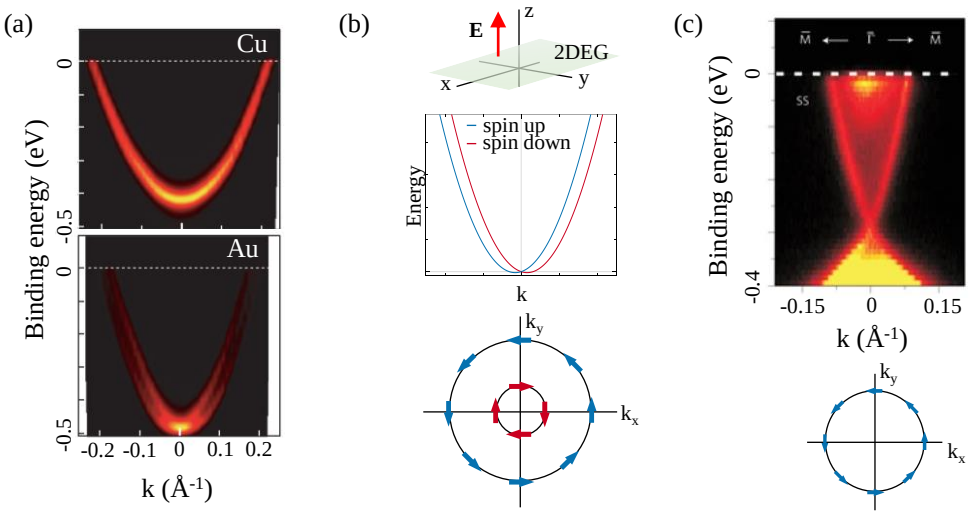

Figure 2.2: *(a) (top) ARPES measurement of nearly-free electrons in Cu valence band, (bottom) ARPES measurement of Rashba states in Au(111) surface (adapted from ref. [63]); (b) (top) 2D electron gas with an out-of-plane electric field, (middle) spin-dependent energy splitting of eq. 2.7, due to Rashba effect, (bottom) spin-dependent energy splitting in the k space; (c) (top) ARPES of topological surface states in Bi_2Se_3, (bottom) spin-dependent energy splitting in the k space for a topological insulator (adapted from ref. [68]).*

If ordinary Hall effect consists in the generation of an accumulation of charge in the direction perpendicular to the external magnetic field and the applied electric field, SHE creates a spin current and a consequent spin accumulation transverse to the applied electric field, without the need of a magnetic field. As for the case of anomalous Hall effect, SHE is caused by the spin-dependent deflection of electrons moving in the material which produces no transverse voltage (see figure 2.3). According to Onsager reciprocal relations, it is possible to observe the opposite effect, named inverse spin Hall effect (iSHE) as the production of a transverse charge current due to the injection of a spin one. After its discovery in 1971 by Dyakonov and Perel [74], it was studied by Hirsch [75] and experimentally observed for the first time in GaAs semiconductor by Kato *et al.* [76].

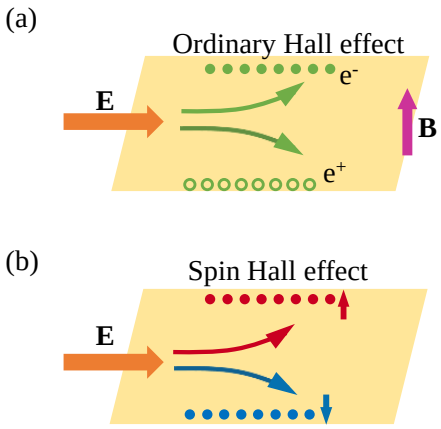

Figure 2.3: *(a) Ordinary Hall effect, the perpendicular field provides the accumulation of charge at the edges of the sample; (b) Spin Hall effect, a spin accumulation is created just by injecting a current.*

In analogy with ordinary Hall effect, one can write a figure of merit for SHE. This parameter is known in literature as *spin Hall angle* θ_{SHE}, it connects the injected charge current density to the generated spin current one:

$$\mathbf{j}_c = \theta_{\mathrm{SHE}} \left(\mathbf{j}_s \times \boldsymbol{\sigma} \right), \tag{2.9}$$

where $\mathbf{j}_\mathrm{c}$ and $\mathbf{j}_\mathrm{s}$ stay for charge and spin current densities, while $\boldsymbol{\sigma}$ is the spin polarisation unitary vector. In terms of the elements of the spin Hall conductivity tensor σ_{ij}^k (where the indexes can be x, y or z and, while i and j account for the standard component of the conductivity tensor, k indicates the spin polarisation direction), θ_SHE reads:

$$\theta_\mathrm{SHE} := \frac{\sigma_{ij}^k}{\sigma_{xx}}. \tag{2.10}$$

Since SHE is directly related to SOC, heavy metals have a relatively large spin Hall angle. Typical examples are Pt [77], Ta [78] and W [79]. Two contributions appear in SHE, one intrinsic and one extrinsic. The first one is related, as for the case of anomalous Hall effect, to the presence of an anomalous velocity of carriers, while the second one is related to spin-dependent scattering caused by impurities mediated by SOC.

Intrinsic SHE

As mentioned before, this mechanism can arise even in absence of scattering with defects or impurities [27, 80, 81]. It actually has a more fundamental origin in the band structure of materials. In particular, carriers gain an anomalous contribution to their velocity in presence of an electric field (namely, a charge current flowing into the material) strictly related to *Berry curvature*, which for large SOC materials is a spin-dependent quantity which cops with the topology of the bands (it is sketched in figure 2.4(a)).

Extrinsic SHE

The spin-dependent scattering from defects or impurities was widely discussed in order to explain anomalous Hall effect. Two main mechanisms arise: *skew* and *side-jump* scattering. They account for non-diagonal terms in the conductivity tensors. The first one [82] describes a SOC-mediated process which leads to an asymmetric scattering, changing the k vector of electrons according to their spin, so their are deflected in opposite directions. The second one [83] has a quantum nature and consists in a discontinuous and finite side-jump due to a central potential, again in presence of SOC. This scattering process preserves the magnitude of the k vector of electrons, but changes its direction. The two mechanisms are depicted in figure 2.4(b)-(c))

2.3.2 Rashba-Edelstein effect

Another mechanism which produces a spin current is Rashba-Edelstein effect (REE) [26]. As for the case of SHE, it is possible to define the reciprocal phenomenon as inverse Rashba-Edelstein effect (iREE). In order to observe this process it is necessary to deal with a specific Fermi contour, which presents spin-momentum locking. For this purpose, it is possible to consider both Rashba systems and TSS, which present the same locking angle (90°) between spin and momentum (for the case of topological states the effect is simply called Edelstein effect). Hence, the discussion which follows can be applied to both of them. This effect was firstly experimentally observed in semiconductor quantum well structures and it was called spin Galvanic effect [84][3].

[3] Even if this notation is widely used in the spintronics community, in this work this effect is addressed with the name of Rashba-Edelstein effect.

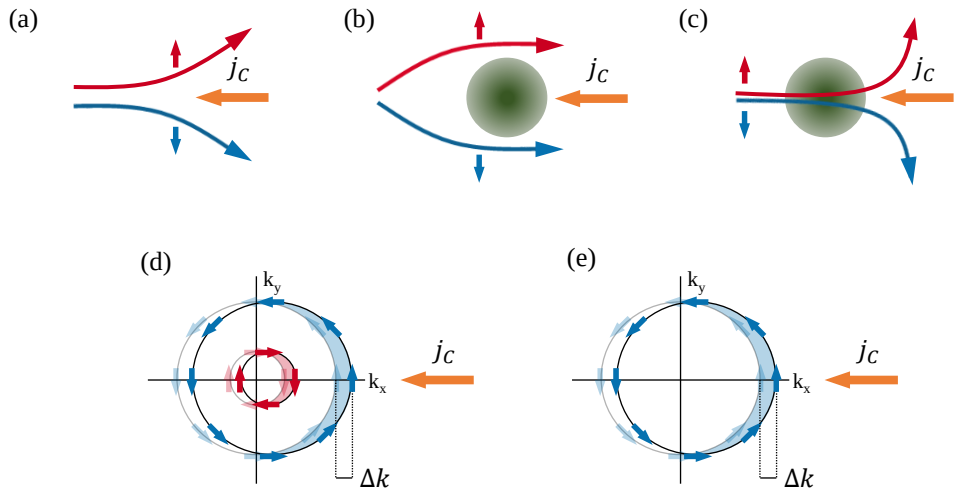

Figure 2.4: *Cartoons of: (a) Intrinsic SHE; (b) Skew scattering extrinsic mechanism in SHE; (c) Side-jump extrinsic mechanism in SHE; (d) Rashba-Edelstein effect in Rashba system. The two contours are shifted of an ammount Δk giving opposite spin polarisations; (e) REE in TSS, the spin accumulation is given by the shift of just one band.*

When a charge current density $\mathbf{j}_c$ is injected in such a system, for example along the $-x$ axis, a Coulomb force acts on carriers due to an electric field $\mathbf{E} = \mathbf{j}_c/\sigma$. This arises as a rigid shift of the Fermi contour (both contours, if it is the case of a Rashba system [85]). Panels (d) and (e) of figure 2.4 represent Rashba bands and TSS, respectively. This shift Δk is given by:

$$\Delta k = \frac{\tau q j_c}{\hbar \sigma}, \tag{2.11}$$

where τ is the electron scattering time and q is charge of the carrier. Due to this shift, a spin accumulation appears (reduced in the case of a Rashba system, since the two contours have opposite chirality). If this spin accumulation relaxes to an adjacent layer, a net pure spin current flows perpendicular toward this interface.

As for the case of SHE, one can define a figure of merit for the REE, which in this case has unit of length (since typical Rashba systems and TSS are two-dimensional) and it is defined as:

$$\lambda_{\mathrm{REE}} := \frac{j_s^{3D}}{j_c^{2D}}. \tag{2.12}$$

It is possible to make a rough estimation of the efficiency of charge-to-spin conversion for a 2DEG Rashba system [85, 86]. The total spin accumulation is: $\langle \delta S \rangle = \delta S_+ + \delta S_-$, where the two opposite contours are taken into account. The two contours have also different relaxation times $\tau_\pm$, Fermi k vector $k_{F\pm}$ and give rise to a total produced current $j_c^{2D} = j_+ + j_-$. Hence, in terms of the Rashba parameter α_R, one can obtain after few calculations and approximating to first order:

$$j_c^{2D} = \frac{q \alpha_R}{\hbar} \langle \delta S \rangle \tag{2.13}$$

and finally, using the fact that $j_s^{3D} = q \langle \delta S \rangle / \tau$:

$$\lambda_{\mathrm{REE}} = \frac{\alpha_R \tau}{\hbar}. \tag{2.14}$$

Hence, larger are the Rashba parameter and the relaxation time, larger is the overall efficiency of the conversion process. So giant Rashba effect, as for the case of FERSC, seems to go in right direction to maximise this kind of effect.

The possibility to modulate and control this kind of effect is very intriguing for spin-orbitronics applications and it is offered by complex heterostructure. For example, in the case of LaAlO3/SrTiO3 interface, a 2DEG is created and an iREE was shown to be tuned by applying a gate voltage [31]. In FERSC, both SHE and REE can play a fundamental role in spin transport. For the case of GeTe, it was shown that iSHE can be modulated in sign by applying a gate voltage, up to room temperature, relying on the possibility to write the ferroelectric polarisation state unambiguously [1].

2.3.3 Bilinear magnetoelectric resistance

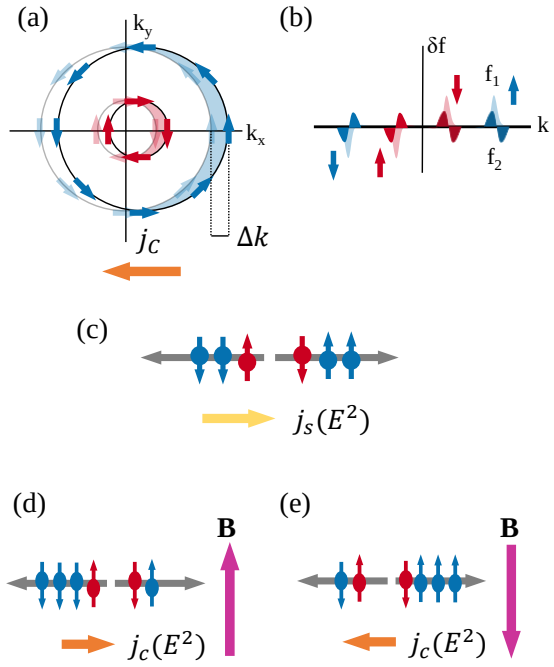

Figure 2.5: *(a) Rashba contour with an injected charge current* $\mathbf{j}_c$*; (b) First and second order corrections to the distribution function; (c) The second order correction gives rise to a spin current; (d-e) When a magnetic field is applied along* $\pm y$ *direction there is a partial spin-to-charge conversion which produces a second order charge current which is summed or subtracted, giving opposite contributions to the resistance.*

As discussed in previous sections, Rashba contours trigger spin transport in materials, so a possible method to study this kind of systems is through magnetoelectric measurements. It was shown in 2018 that a second order magnetoelectric effect arises when measuring bare TI materials and it was called bilinear magnetoelectric resistance (BMER) [87]. Up to now, there is not a clear microscopic explanation of the phenomenon, because different mechanisms seem to compete [88, 89]. Nevertheless, it can be understood by qualitatively looking at the Rashba (or TSS) contours. As explained in section 2.3.2 a charge current allows the bands to rigidly shift and this produces a spin polarisation (figure 2.5(a)). One can write the distribution function of carriers as an expansion of the form: $f = f_0 + f_1 + f_2$, where $f_{0,1,2}$ are the Fermi-Dirac distribution, the first and the second order corrections to the equilibrium distribution, respectively. f_1 (pictorially described by panel (a)) and f_2 are plotted in panel (b) in light and dark colours, respectively.

When an electric field is applied (in the $-x$ direction, for example) a second order non-equilibrium longitudinal spin current $\mathbf{j}_s(\mathbf{E}^2)$ is generated (see figure 2.5(c)), due to spin-momentum locking. When an external magnetic field is applied parallel or anti-parallel to the spin direction (which means $\pm y$) of this pure spin current, $\mathbf{j}_s(\mathbf{E}^2)$ is partially converted in a longitudinal charge current whose sign depends on the direction of the external magnetic field (as depicted in figure 2.5(d)-(e)). This current is summed up to

the overall current flowing into the material resulting in the appearance of two states with higher and lower resistance with respect to the case in which the field is orthogonal to the spin direction ($\pm x$ or $\pm z$ directions). BMER amplitude is linear both with respect to magnetic field amplitude and to current density.

BMER was detected firstly in TI Bi_2Se_3, then in some other systems, such as $SrTiO_3$ [90], Ge(111) [91], α-Sn [92] and it was shown that it can be a very useful instrument to quantitatively estimate the Rashba parameter [93]. In 2021, also in GeTe devices was possible to measure BMER [94]. In chapter 7 this phenomenon is investigated more deeply and some questions about its physical origin are addressed.

2.3.4 Spin currents to manipulate magnetism: spin-orbit torques

In previous sections, some mechanisms exploited to generate spin currents were discussed. In this section, the interaction between them and the magnetisation vector in ferromagnetic (FM) materials is explored. Spin accumulations at the interface generated by SOC-mediated effects are source of angular momentum which can be transferred to FM by so-called *spin-orbit torques* (SOT). This effect was discovered and studied in heavy metal/FM systems firstly in refs. [30, 78].

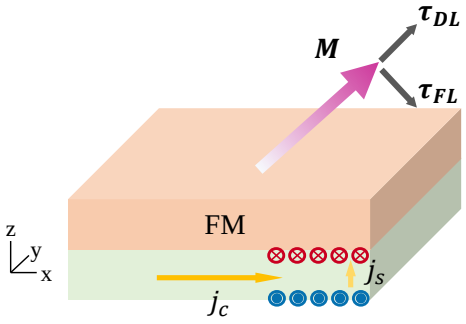

Figure 2.6: *A spin current generated in the bottom material creates a spin accumulation (in this case along y) which acts on the magnetisation of the ferromagnet through SOT, composed by two components, namely damping-like torque and field-like torque.*

The discussion of the microscopic mechanism is beyond the scope of this work and it is actually not completely well understood. Several attempts and approaches were employed for this aim, one of the most addressable is magnetoelectronic circuit theory [95, 96]. Here the interest is in understanding the effect of a spin accumulation on the magnetisation dynamics, this can be studied looking at the Landau-Lifshitz-Gilbert equation, which reads:

$$\frac{\mathrm{d}\mathbf{M}}{\mathrm{d}t} = -\gamma_0 \mathbf{M} \times (\mathbf{H} + J\mathbf{m}) + \alpha \mathbf{M} \times \frac{\mathrm{d}\mathbf{M}}{\mathrm{d}t}, \tag{2.15}$$

where $J\mathbf{m}$ represents the additional effective field, due to exchange coupling, between the spin accumulation $\mathbf{m}$ and the local magnetisation $\mathbf{M}$, while $\mathbf{H}$ contains all the other effective fields terms (external, demagnetising, anisotropy), γ_0 is the gyromagnetic ratio and α is the Gilbert damping. It is clear that only transverse accumulation acts on $\mathbf{M}$. One can define two different components of the accumulation in the transverse plane with respect to the magnetisation, viz:

$$J\mathbf{m}_\perp = a\mathbf{m} \times \mathbf{M} + b\mathbf{m}, \tag{2.16}$$

where a and b depend on the properties of the interface. These two terms represent two simultaneous spin torques. The first one, of the form $a\mathbf{M} \times (\mathbf{m} \times \mathbf{M})$, with an effective field which depends on the magnetisation direction, has a similar effect of the Gilbert damping and it is called *damping-like* torque $\boldsymbol{\tau}_{\mathrm{DL}}$. The second one is of the form $b\mathbf{M} \times \mathbf{m}$

and it is equivalent to an effective field $b\mathbf{m}$ which tends to align along it the magnetisation, this contribution is called *field-like* torque $\boldsymbol{\tau}_{\mathrm{FL}}$. The two components of the torque are depicted in figure 2.6.

Hence, whatever is the character and the direction of the spin accumulation at the interface, a two-component torque is generated on the magnetisation, driving its dynamics. Measuring SOT in heterostructures allow to infer information about the physical origin of these processes together with an indirect characterisation of the material which generates SOT. The large variety of phenomena which attends in a bilayer forces to develop an experimental method to measure and disentangle all these contributions. This can be done by exploiting harmonic Hall detection of first and second order resistance, injecting in a Hall bar device an oscillating current [97, 98] (see section 4.4).

SOT are intensively studied nowadays [13, 99, 100] and represent one of the most promising route in beyond-CMOS storage elements [101].

2.4 Case studies: GeTe and SnTe

Chalchogenides and in particular tellurides are very well known materials in material science. They have been exploited for very different applications, spanning from photovoltaic cells (CdTe [102]) to thermoelectric elements (PbTe [103]). GeTe and mostly $Ge_2Sb_2Te_5$ are very well-known phase change materials, used for the implementation of memory elements [104, 105, 106]. This means that they can undergo a reversible crystalline-to-amorphous phase transition by current pulses which allows to have two states with very different properties. This phenomenon is widely exploited in the so-called phase change memories [107]. In the following, the discussion focuses on GeTe and SnTe, which are group-IV tellurides, presenting them in a very different light.

2.4.1 Germanium telluride

Despite the variety of applications which chalchogenides are involved in, GeTe has been also known to be ferroelectric since a long time [110]. Moreover, all the requirements to display giant Rashba effect (namely: (i) lack of inversion symmetry; (ii) the valence band maximum (VBM) and the conduction band minimum (CBM) that have the same symmetry character; (iii) large SOC; (iv) it is a narrow-gap semiconductor) are satisfied [20]. In 2013, through DFT calculations, it was predicted that the structural distorsion which gives rise to ferroelectricity also brings a giant bulk Rashba effect [17, 21]. Opposite distorsions provoke opposite sign of the polarisation vector as well as opposite Rashba spin textures. This was also experimentally validated in 2018 [22, 108].

Ferroelectricity in GeTe is characterised by a Curie temperature of $\sim$ 720 K and a phase transition from the rhombohedral phase (α-GeTe) to the paraelectric cubic phase (β-GeTe). The ferroelectric polarisation arises along the (111) direction from the shift of Ge and Te atoms from the cubic position and its value is $\sim 60\,\mu C/cm^2$ [109] (see figure 2.7 (a)-(b)).

GeTe is also a narrow-gap semiconductor ($\epsilon_{\mathrm{gap}} \sim 0.8\,\mathrm{eV}$) with a high density of holes as free carriers ($N \sim 3 \times 10^{20}\,\mathrm{cm}^{-3}$). This is due to an intrinsic heavy p-doping due to the structural presence of Ge vacancies[4]. This unusually high conductivity makes GeTe

[4]The author, during his Ph.D. activity, was also involved in the preparation of GeTe samples in which a doping compensation was performed by co-evaporating indium to obtain $In_xGe_{1-x}Te$. The samples were then characterised with standard techniques

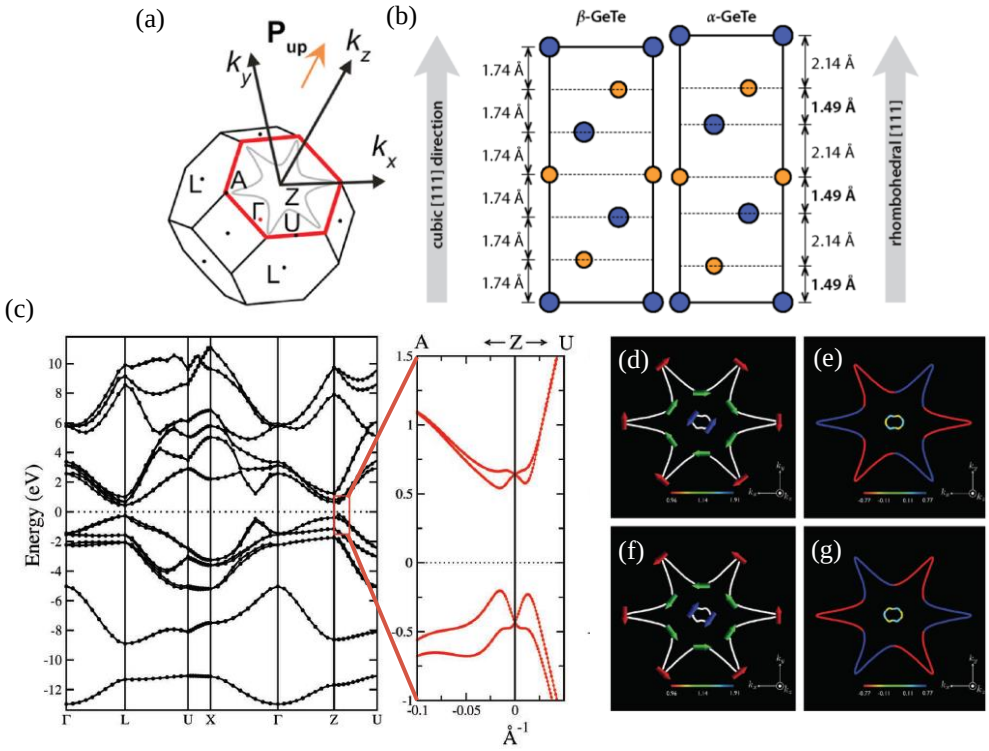

Figure 2.7: *(a) First Brillouin zone of GeTe, the polarisation vector points along the (111) direction, while k_x and k_y point along ZA and ZU, respectively; (b) Atoms position along the (111) direction in the β-phase (cubic and paraelectric) and in the α-phase (rhombohedral and ferroelectric); (c) Bands diagram calculated by DFT, the in zoomed panel, the direction of interest ZA and ZU; (d-e) In-plane and out-of-plane spin textures in the case of outward polarisation vector; (f-g) In-plane and out-of-plane spin textures in the case of inward polarisation vector (adapted from refs. [21, 108, 109]).*

to be associated to *polar metals* and makes the control of the polarisation by gate voltage very hard [111]. In 2021, the author and coworkers in ref. [1] succeeded in demonstrating (by joining piezoresponse force microscopy and electrical detection) the possibility to perform gating in micrometric structures and control the polarisation vector in GeTe thin films by correlating the polarisation switching to a consequent change in the conductive properties.

As mentioned before, the Rashba effect in GeTe is said to be giant. This is due to the large Rashba parameter which has not any counterpart in other materials, $\alpha_{\mathrm{R}} \sim 5\,\mathrm{eV\,\AA}$ (BiTeI has $\alpha_{\mathrm{R}} \sim 3.8\,\mathrm{eV\,\AA}$ [20, 19]). As written before, the polarisation vector is along the (111) direction which means, in term of first Brillouin zone directions, along the ΓZ direction. The giant Rashba splitting affects the band around the Z point, in the plane perpendicular to ΓZ, which is identified by the hexagonal face with principal directions ZA and ZU. The Rashba Hamiltonian for GeTe can be expressed as:

$$H_{\mathrm{R}} = \alpha_{\mathrm{k}} \left(\sigma_x k_y - \sigma_y k_x\right) + \lambda \left(k_+^3 + k_-^3\right) \sigma_z, \tag{2.17}$$

with $k_\pm := k_x \pm i k_y$, $\alpha_{\mathrm{k}} := \alpha_{\mathrm{R}} \left(1 + a k^2\right)$, k_x and k_y represent the ZA and ZU directions,

(diffractometry, spectroscopy, piezoresponse force microscopy) and found to be crystalline and ferroelectric and a giant Rashba was displayed as well. The samples were still p-doped, but a lighter carrier concentration would allow to a better control of ferroelectricity by gating. Further investigations are still needed.

respectively and λ accounts for the so-called *hexagonal warping* of the bands. Even if the dominant component of the spin texture is the in-plane component of the spin, it also present a small out-of-plane component, not detected so far from the experimental point of view. Both the in-plane and the out-of-plane components are reversed by reversing the sign of the polarization (the DFT calculations are plotted in figure 2.7(c)-(d)-(e)-(f)-(g), together with the spin textures for opposite directions of the polarisation vector).

2.4.2 Tin telluride

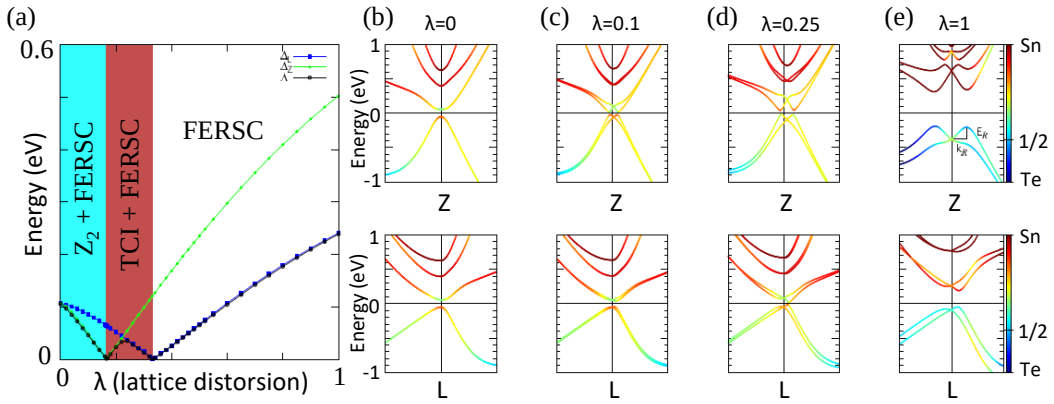

Figure 2.8: *(a) Coexistence of different states changing the λ parameter (the lattice distorsion) and the relative band gap for such a configurations; DFT calculations along the most remarkable directions at (b) $\lambda = 0$; (c) $\lambda = 0.1$; (d) $\lambda = 0.25$; (e) $\lambda = 1$ (adapted from ref. [112]).*

SnTe shares a lot of properties with GeTe, it is a narrow-gap semiconductor ($\epsilon_{\text{gap}} \sim 0.2\,\text{eV}$ [113]), it shows ferroelectric polarisation along the (111) direction ($\sim 40\,\mu\text{C/cm}^2$ [112]) in the α-phase and in the same phase it matches the conditions for a giant Rashba splitting. Increasing the temperature, it undergoes to a phase transition very similar to the one of GeTe (at $T_C \sim 100\,\text{K}$ [113, 114, 115]) to a cubic bulk SnTe stable in the paraelectric β phase which is very well known as a TCI [72, 116], already exploited in SOT devices [102].

In 2016, it was discovered that the Curie temperature can be enhanced up to $\sim 270\,\text{K}$ going towards the ultra-thin film limit which stabilises the polarisation vector in the in-plane direction [117].

Even more interesting, it was investigated by density functional theory (DFT) calculation the possibility to engineer the band structure of β-SnTe, which is a TCI at room temperature [112]. Spanning the λ parameter, which represents the lattice distorsion, from 0 (cubic phase) to 1 (rhombohedral phase) it is possible to obtain a coexistence of state, from TCI+FERSC, passing to $\mathbb{Z}_2$+FERSC and finally to FERSC only (the band structures for different values of the λ parameter are depicted in figure 2.8, in particular panel (a) shows the transition between different states of matter and how the band gap of the semiconductor changes with λ).

One of the goals of this work moves from this idea. DFT calculations constructed a linear path between two crystal structures. As explained before, α-GeTe belongs to the rhombohedral space group (R3m) and it is a FERSC, while SnTe to the cubic one (Fm3m). So, a possible way to draw a line between these two extreme states is to dope

tin telluride with germanium constructing a continuous transformation between the two compounds. Ge doping naturally makes the crystal tend to a lattice with a distorsion. The alloy $Sn_xGe_{1-x}Te$ is expected to combined the properties of the two extreme conditions ($x = 0, 1$) in a way which resembles the idea of ref. [112]. In chapter 5 this task is tackled experimentally together with a comparison with new DFT calculations.

CHAPTER 3

Interaction of polarised electrons with materials: a survey on spin detectors

Unluckily, it is not possible to spatially separate the two spin states of a free electron using a magnetic field. What Stern and Gerlach did in their famous experiments with neutral silver atoms [118, 119] is not reproducible with charged particles, as electrons are, due to Lorentz force which directly acts on their trajectories. Other solutions must be found in electron-matter interaction which introduces scattering mechanisms that play a fundamental role to properly investigate this elusive quantum number.

In order to provide the basic concepts about the interaction of polarised electrons with matter and the mechanisms which intervene in such a complicate process, this chapter is organised in three sections. After the introductory section 3.1 stating some definitions, the interaction with magnetic materials is reviewed in section 3.2, while section 3.3 provides a survey on the most common spin detectors and the physical principles governing them. As emerged in chapter 1, the need of a new paradigm for spin detection is discussed, shedding light on the purposes of this thesis work.

3.1 Introduction

As mentioned before, the spin of a particle was first investigated in neutral silver atoms in 1922. The possibility to study free electrons spin remained debated until, in 1929, Mott suggested the possibility to scatter electrons from heavy nuclei targets to have spin separation [120]. This process is possible because of SOC. Even if the realisation of such an idea is quite simple, the efficiency is not so large, so after Mott's idea the scientific community started to move towards exchange interaction. Hence, the mechanisms which arise when polarised electrons impinge on magnetic materials became of great interest.

In order to proceed further with the discussion of interactions between polarised electrons and matter, it is necessary to state some preliminary definitions [121]. It is well-known that the wavefunction of an electron can be written as:

$$\psi(\mathbf{r}, t, \mathbf{s}) = \chi C e^{i(\mathbf{k}\cdot\mathbf{r}-\omega t)}, \tag{3.1}$$

where χ accounts for the spin part of the wavefunction. In order to describe an ensemble of electrons, it useful to introduce a quantity called *polarisation vector* $\mathbf{P}$. Its components (x, y, z) are the difference between the number of up and down electrons along the quantisation axis defined by the component. This vector and the number of electrons completely describe a beam. The interest in studying the interactions between polarised electrons and matter is to know how this two quantities change in time. Pauli provided the formal tools to address this question, namely *spinors* and *spin matrices*.

A single electron can be described by:

$$\begin{cases} \chi_{\text{up}} & = |\uparrow\rangle = |+\rangle = \begin{pmatrix} 1 \\ 0 \end{pmatrix} \\ \chi_{\text{down}} & = |\downarrow\rangle = |-\rangle = \begin{pmatrix} 0 \\ 1 \end{pmatrix} \end{cases}. \tag{3.2}$$

With this definition, it is possible to described any direction of space for the spin:

$$\chi = u_1 |\uparrow\rangle + u_2 |\downarrow\rangle = \begin{pmatrix} u_1 \\ u_2 \end{pmatrix}. \tag{3.3}$$

With the usual definition for Pauli matrices:

$$\sigma_x := \begin{pmatrix} 0 & 1 \\ 1 & 0 \end{pmatrix}, \qquad \sigma_y := \begin{pmatrix} 0 & -i \\ i & 0 \end{pmatrix}, \qquad \sigma_z := \begin{pmatrix} 1 & 0 \\ 0 & -1 \end{pmatrix}, \tag{3.4}$$

it is possible to define the expectation value for the spin direction as $\langle\sigma_i\rangle = \langle\chi| \sigma_i |\chi\rangle$ and then:

$$\mathbf{P} = \begin{pmatrix} \langle\sigma_x\rangle \\ \langle\sigma_y\rangle \\ \langle\sigma_z\rangle \end{pmatrix}. \tag{3.5}$$

So, for a single electron the direction of $\mathbf{P}$ is the direction of its spin and $|\mathbf{P}|= 1$.

In real experiments, one deals with a beam of electrons. The following definitions hold: if all the spins are polarised in the same direction, $|\mathbf{P}|= 1$, meaning that the beam is completely polarised and it is said to be in a *pure state*; if they point in different directions, $0 < |\mathbf{P}|< 1$ and the beam is said to be in a *mixed state*. One can obtain the polarisation along a certain quantisation axis, summing up the probabilities of having spin up or spin down of each electron. This means:

$$n^{\uparrow} := \sum_k |u_1^k|^2, \qquad n^{\downarrow} := \sum_k |u_2^k|^2. \tag{3.6}$$

If each electron is described by a *coherent* superposition of $|\pm\rangle$ states, the sum in eq. 3.6 represents an *incoherent* superposition of the coherent polarisation properties of each

electron. Hence, the degree of spin polarisation of an electron beam along a certain quantisation axis is defined as:

$$P_i = \frac{n^{\uparrow} - n^{\downarrow}}{n^{\uparrow} + n^{\downarrow}}, \tag{3.7}$$

and $N := n^{\uparrow} + n^{\downarrow}$ is the total number of electrons.

When one is dealing with polarised electrons interacting with a magnetic material, it is a common practice not to define an absolute direction for the $\mathbf{P}$ vector, but the relative position with respect to the magnetisation vector $\mathbf{M}$[1]. Hence, defining I as the relative intensity, the polarisation relative to the magnetisation axis becomes:

$$P = \frac{I^{\uparrow\downarrow} - I^{\uparrow\uparrow}}{I^{\downarrow\uparrow} + I^{\uparrow\uparrow}}, \tag{3.8}$$

where the relative directions of the arrows represent parallel and anti-parallel orientation.

3.2 Interactions with matter of a polarised electron beam

In this section the most relevant spin-dependent interaction mechanisms and their main consequences on spin polarisation are briefly presented. There are four principal processes that intervene in this discussion. They are schematically illustrated in figure 3.1. In the following, an incident electron beam with polarisation $\mathbf{P}^0$ is assumed to impinge on a material. The quantisation axis is along z and it is defined by the direction of the effective magnetic field $\mathbf{H}$ (it is the magnetisation for a ferromagnet and the external field for a normal metal). The mechanisms can be grouped as follows [122]:

(i) **Spin precession.** When immersed in a external magnetic field, every particle possessing a magnetic moment is subjected to *Larmor precession*. This means that $\mathbf{P}$ preceeds about the magnetisation axis at frequency ω_{L}, known as Larmor frequency, without changing its magnitude. Hence, the time scale of this process is inversely dependent on the magnetic field, through: $\tau_{\mathrm{L}} = 1/\omega_{\mathrm{L}} = \hbar/(2\mu_{\mathrm{B}}|H|)$, where μ_{B} is the Bohr magneton (see figure 3.1(a)).

(ii) **Spin exchange scattering.** The most relevant process which gives rise to spin exchange in a normal metal is electron-electron scattering. This occurs in a redistribution of the spin polarisation over the states available in the material. In a ferromagnetic material, where the so-called *two-currents model* holds, an energy splitting is present between spin up and spin down states. Spin exchange scattering consists in a *spin-flip* transition, with a characteristic relaxation time. The polarisation vector rotates, while its magnitude may be preserved constant (see figure 3.1(b)).

(iii) **Spin dephasing.** When electrons are precessing about the effective field, their spins are initially aligned, but after a characteristic dephasing time their motion becomes out of phase. This leads to a decay of the transverse component (perpendicular to the quantisation axis) towards zero. In normal metals this could produce a complete spin randomisation (see figure 3.1(c)).

(iv) **Spin selective absorption.** When an electron beam is transmitted through a ferromagnetic material, the differences in spin up and spin down densities of states may

[1] According to the common definition of $\mathbf{M}$, it always points along the direction defined by *minority spins*.

produce different scattering in spin channels. The minority spins are preferentially scattered because of the presence of more unfilled states, hence the absorption for this channel increases. Since the loss is asymmetric the polarisation vector rotates towards the z direction. Also its magnitude changes (see figure 3.1(d)).

It is possible to do an evaluation *a posteriori* to quantify the relative contribution of these four mechanisms. What turns out is that, together with *spin precession*, the dominant process in the transmission of spin-polarised electrons is *spin selective absorption*.

The *Poincaré formalism* helps in describing polarisation changing of a beam (of electrons, of light,...) due to the interaction with an external magnetic field. This treatment holds both for transmission and reflection (the analogous phenomena when light is used instead of electrons are called Faraday and Kerr effects). The interaction is phenomenologically described through a complex *interaction matrix* $\mathbf{I}$:

$$\mathbf{I} = \begin{pmatrix} \sqrt{1+A}e^{i\varphi/2} & 0 \\ 0 & \sqrt{1-A}e^{-i\varphi/2} \end{pmatrix}, \tag{3.9}$$

where the constants A and φ account for the two processes analysed before, namely absorption and precession, while the off-diagonal terms are set to zero because spin-flip events are demonstrated to be sufficiently rare [123, 124]. A is called *spin asymmetry parameter*, it describes the relative trasmission/reflection of up and down spins interacting with a material. Its definition is analogous to the definition of polarisation of eq. 3.8:

$$A := \frac{I^{\uparrow\downarrow} - I^{\uparrow\uparrow}}{I^{\downarrow\uparrow} + I^{\uparrow\uparrow}}. \tag{3.10}$$

By definition, $0 \leqslant |A| \leqslant 1$. If one considers a polarised electron beam (i.e., $|P_0| \leqslant 1$) perpendicular to the magnetisation, after the interaction the polarisation vector becomes:

$$\mathbf{P} = \begin{pmatrix} P_0\sqrt{1+A^2}\cos\varphi \\ P_0\sqrt{1-A^2}\sin\varphi \\ A \end{pmatrix}. \tag{3.11}$$

This corresponds to a twofold motion: a precession by an angle φ around the magnetisation and a rotation into the direction of the magnetisation, due to the selective absorption of spins, where minority spins are more attenuated than majority ones. The angle θ of this rotation is given by [40]:

$$\tan\theta = \frac{A}{P_0\sqrt{1-A^2}}. \tag{3.12}$$

3.3 Spin detectors: a survey

As mentioned in the preliminary discussion of chapter 1, there are several mechanisms that can be exploited in order to build up a spin detector. The physical principles underlying them are basically two: Mott scattering and exchange scattering (treated in the former section). In the following, the working principle of three spin detectors is analysed and their advantages and disadvantages are discussed.

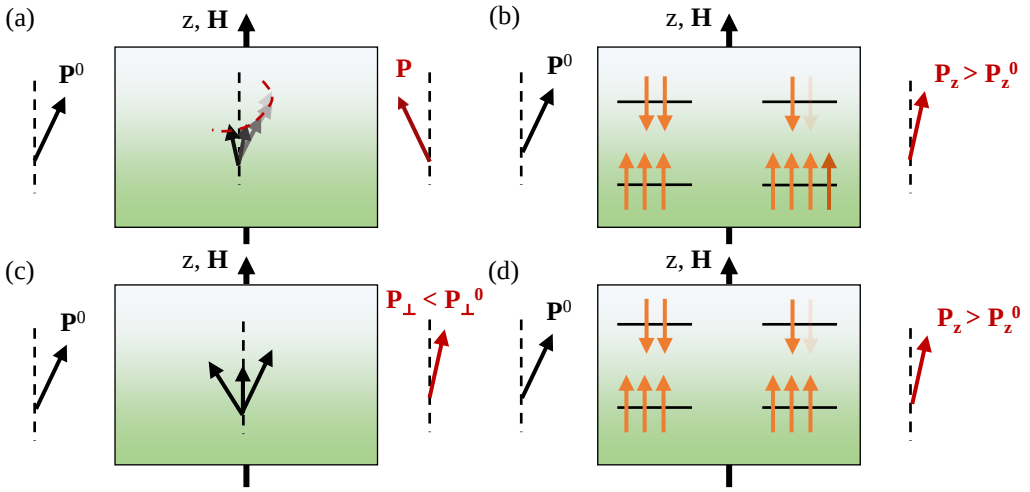

Figure 3.1: *(a) Spin precession: every spin preceeds about the quantisation axis in a coherent way, so the magnitude of the polarisation is preserved, while the direction is not; (b) Spin exchange scattering: with an effective magnetic field, the two spin states are not degenerate in energy, a spin-flip event may occur leading to a change of the z component of the polarisation vector; (c) Spin dephasing: after a characteristic dephase time the precession of panel (a) becomes incoherent and the spins may become randomised. This gives rise to a decrease (or even a suppression) of the perpendicular component of the polarisation vector; (d) Spin selective absorption: the minority spins are preferentially absorbed since there are more unfilled states. This leads to a decrease of the number of spins pointing in this direction and to a consequent change of magnitude of the polarisation vector.*

3.3.1 Mott detector

Mott detector relies on the very first idea of separate electrons according to their spins, as conceived by Mott in 1929 [120]. It consists in exploiting the SOC in the scattering of electrons with Coulomb field of heavy atoms (which are typically gold or thorium atoms [125]). The electrons are prepared at $\sim 100\,\mathrm{keV}$, so that they can penetrate deeply in the Coulomb field of the heavy atoms. Due to relativistic theory, in the rest frame of electrons, the moving electric field of atoms generates a magnetic field, whose lines are circular. Given a certain direction of the magnetic moment of the electron $\boldsymbol{\mu}$ – e.g., up – if it passes on the right it is parallel to the magnetic field, so the force[2] pushes the electron towards the left, where the field is stronger. The same holds for an electron with the same spin, passing on the left of the nucleus, since the moment and the magnetic field are antiparallel the force pushes it again to the left, where the field is weaker. The opposite happens for electrons with spins pointing down: they are scattered to the right. Mott scattering is founded on this principle (it is sketched in figure 3.2).

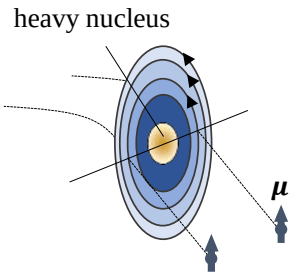

Figure 3.2: *Cartoon of the field lines as seen by the moving electron going towards a heavy nucleus. If the momentum is pointing up, it is always scattered to the left.*

Now, if one puts two detectors at the same angle θ, one on the right and the other on

[2]The force applied to a magnetic moment, by an inhomogeneous field $\mathbf{H}$ reads: $\mathbf{F} = \nabla(\boldsymbol{\mu} \cdot \mathbf{H})$.

the left, it is possible to collect electrons which have a preferred spin direction. Hence, the scattering *asymmetry* is given by:

$$A = \frac{I^{\text{right}} - I^{\text{left}}}{I^{\text{right}} + I^{\text{left}}}, \tag{3.13}$$

where $I^{\text{right,left}}$ are the currents measured by the two detectors. A is proportional to the beam polarisation P through the so-called *Sherman function* $S = S(\theta, E)$: $A = S(\theta, E)P$, where E is the electron energy. This function can be calculated for a specific geometry [121, 126]. For instance, in the central field approximation for gold atoms, with electrons at $E = 150\,\text{keV}$ and $\theta \sim 120°$, $S = 0.4$ [127].

Although the set-up for Mott polarimetry seems to be quite simple, there are some drawbacks which do not make it the ideal candidate for spin polarimetry. Indeed, even if Sherman function values can approach unity, the maxima in $S(\theta, E)$ occur near local minima of the differential scattering cross section,[3] where the scattering efficiency is very low [125, 128]. This results in a very poor figure of merit (defined as $\eta = S^2 I/I_0$) of the order of $\sim 1 \times 10^{-4}$ [125].

3.3.2 Very low-energy electron diffraction

In the Nineties, a great effort was done in order to replace Mott detection to enhance the performances of spin polarimeters. The new framework aimed at exploiting exchange scattering instead of spin-dependent scattering due to SOC.

As reviewed in section 3.2, among the several effects which arise when a polarised beam interacts with a magnet, two of them, namely precession and selective absorption, are preponderant. While precession induces a rotation of the polarisation vector, selective absorption drastically changes its magnitude. This was exploited by Bertacco *et al.* in refs. [34, 129] to obtain a large asymmetry both in the absorbed and in the reflected current in MgO/Fe(001)-p(1×1)O samples. The oxidation of iron and the surface reconstruction obtained increased the asymmetry with respect to the bare iron surface, which reaches the values of 13% in absorption and 45% in reflection in the range $8 - 12\,\text{eV}$ [129].

This idea was exploited in several SARPES set-ups [35, 36] in which the target MgO/Fe was prepared *in situ* and exploited in reflection mode, and took the name of very low-energy electron diffraction (VLEED). It represents the state-of-art in spin polarimetry measurement. Such a configuration produces a higher Sherman function and it drastically increases the figure of merit to $\sim 1 \times 10^{-2}$ [34, 35, 43]. In 2016, Ji *et al.* in ref. [37] designed a two-dimensional VLEED detector consisting in a system of electrostatic lenses which transfers the electron beam image from the exit plane of the ferromagnetic target to a two-dimensional electron detector made by microchannel plates (see figure 3.3(a)). This could allow producing the first multi-channel VLEED (MCVLEED) detector with 6,786 parallel channels which further enhanced the figure of merit to ~ 60.

3.3.3 Very low-energy electron transmission spin detector

Reflection is not the only way to exploit the exchange scattering which produces the asymmetry between different spin channels (scheme in figure 3.3(b)). The transmission

[3] The differential scattering cross section $d\sigma/d\Omega$ can be calculated analytically. The reference for this calculations is the book by Kessler [121].

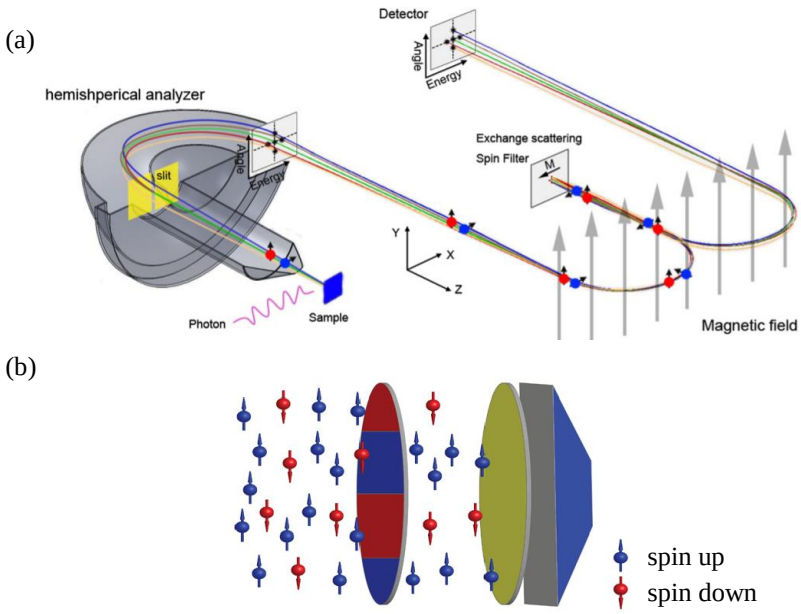

Figure 3.3: *(a) Schematic representation of the MCVLEED detector. The image of electrons coming out from the hemispherical energy analyser (HEA) are guided towards the ferromagnetic target and then to the detector, preserving information about their trajectories; (b) Electrons are differently transmitted by regions with different magnetisation and then their are directly counted by a detector (adapted from refs. [37, 38]).*

of a spin polarised beam through a ferromagnetic thin layer was extensively studied in the Nineties [40, 130, 131, 132], but it was never employed integrated in a SARPES set-up, probably also due to the fabrication issues of such structures, since nanometric thick films are difficult to be kept free-standing and also to be miniaturised to micrometric lateral dimensions.

Also thanks to the boost in MEMS fabrication and the consequent capability to realise suspended features with reliable fabrication techniques, in 2017 the first spin detector based on a matrix of free-standing cobalt films was proposed [38]. This device promises a very large figure of merit $\sim$ 67 (at very low energy $E \sim 2\,\mathrm{eV}$), also avoiding the complex apparatus of electrostatic lenses of the MCVLEED set-up. Nevertheless, this proof-of-concept device has never been integrated in a SARPES set-up and presents a not trivial fabrication process composed by several selective etching steps and the use of sacrificial layers.

In this time-line, this thesis work intervenes. The idea is to further exploit the concept of a selective spin transmission with the aim of overcoming the issues introduced by fabrication, with a free-standing membrane grown on suspended graphene, which is very well-known to display a high robustness, even in the atomic monolayer limit. Chapter 6 deals with the deposition and the characterisation of such devices embedded in a two-dimensional matrix.

CHAPTER 4

Experimental techniques

This chapter is devoted to the presentation of the principal experimental techniques employed for this thesis work. In particular, thin film deposition technologies are described in section 4.1, the fabrication of devices for magnetoelectrical measurements is presented in section 4.2, section 4.3 describes the spin- and angle-resolved photoemission spectroscopy experiments, section 4.4 briefly describes the set-ups for the magnetoelectical characterisation, section 4.5 the set-up for the magnetic characterisation of free-standing films and finally section 4.6 is devoted to the presentation of the development of a spin-polarised electron gun.

4.1 Deposition techniques

This thesis deals with two different topics and both of them strongly rely on the deposition of thin films. Group-IV tellurides, GeTe and SnTe are grown by molecular beam epitaxy (MBE) (the process for GeTe is well-established [133] and was not carried out during this work specifically, while the one of SnTe will be matter of discussion in chapter 5). Free-standing magnetic membranes can be deposited both by MBE and magnetron sputtering. So both techniques are reviewed here together with the main relevant parameters involved in these processes. Both technologies can be performed in Polifab facility with *ad hoc* tools.

The system which allows for film deposition by MBE and the *in situ* characterisation of thin films by electron diffraction and photoelectron spectroscopy is sketched in figure 4.1 [134]. It is composed by five vacuum chambers and a sample of dimensions up to $10 \times 10\,\mathrm{mm}^2$ can move through, without breaking the vacuum. Chamber #1 is the introduction chamber, which is a load-lock used to move samples either to the samples preparation and MBE chamber (#2) or to the pulsed laser deposition chamber (#3) (not

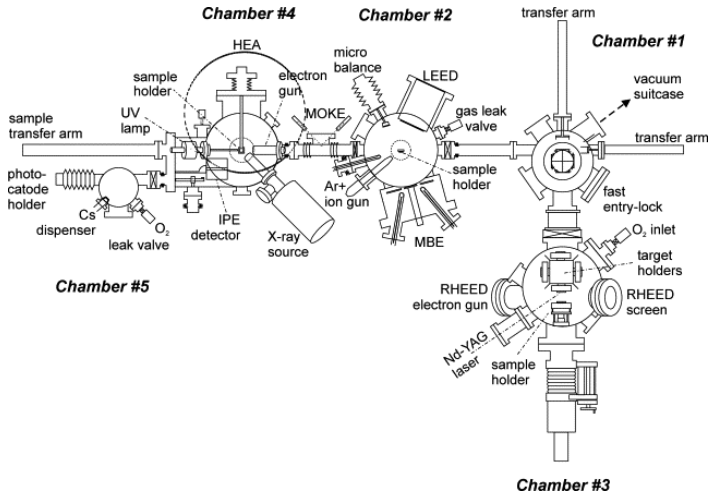

Figure 4.1: *Schematic picture of the deposition and characterisation cluster tool present in Polifab facility composed by five vacuum chambers (from [134]).*

employed in this work). For substrate pre-treatment, the sample preparation chamber is equipped with a filament for thermal annealing and with an argon-ion sputtering. There are seven evaporators for MBE and the possibility to perform controlled oxidation processes. A low-energy electron diffraction (LEED) set-up is present as a characterisation tool. Chamber #4 is the measurement chamber used for spectroscopy. A X-ray source (with Al and Mg anodes) is present, together with a He ultraviolet lamp. These can be used to excite photoelectrons that can be collected and analysed by a hemispherical electron analyser (HEA). A set-up for spin-resolved inverse photoemission spectroscopy (SPIPE) is also present [135], this is treated in detail in section 4.6, together with Chamber #5 which is used for the preparation of photocathodes. Chambers are isolated with gate valves and chambers #2, #4, #5 are in ultrahigh vacuum (UHV) regime (i.e., pressure $< 1 \times 10^{-9}$ mbar), which is of fundamental importance both for deposition processes and for spectroscopic experiments.

4.1.1 Molecular beam epitaxy

MBE was used for the deposition of SnTe films measured in chapter 5, for the re-preparation of GeTe heterostructures analysed in chapter 7 and for the deposition of magnetic thin films (heterostructures based on Co) for magnetic membranes presented in chapter 6.

In MBE, the target material (i.e., a high purity metallic rod or a metallic crucible containing the material) is heated up in UHV causing either its evaporation or sublimation. A flux of atoms which travels towards the sample and gets deposited on it is established. This process can be achieved heating up the target with a resistive filament and/or applying high voltages to the target in order to obtain an electron-beam flux [136]. The former option can be applied to metals which present low vapour pressure and semiconductors, while the latter is used mainly for metals with high vapour pressure and oxides. UHV conditions allow for very few contaminant agents in the chamber, a very large mean free path for atoms emitted from the target and they guarantee almost zero scattering events to them. MBE turns out to be a highly directional process and allows for the growth of

ordered epitaxial thin films. MBE is commonly used for the growth of single-crystalline metals and oxides. In order to achieve this crystal quality, deposition rates are of the order of few Å/min.

The MBE confocal cells of the system in chamber #2 are equipped with a tungsten filament which can be made incandescent with a suitable current ($3 - 6\,\mathrm{A}$), producing free electrons by thermoionic emission which are accelerated towards the target by a positive high voltage ($0.5 - 3\,\mathrm{kV}$) applied to the target material. The deposition rate can be checked moving a quartz microbalance in place of the sample position.

4.1.2 Magnetron sputtering

Magnetron sputtering was used to deposit heterostructures for magnetic free-standing membranes. The materials exploited were CoFeB, Co, Ta, Ru and MgO. Magnetron sputtering was performed in a commercial AJA ATC Orion 8 machine present in Polifab facility.

In magnetron sputtering, a negative high voltage is applied to the target material, while the vacuum chamber is filled with an inert gas (argon is typically used for this purpose). Under certain appropriate partial vacuum conditions, the negative bias creates an avalanche process of ionisation of charge particles (Ar^+ ions and electrons) which establishes a *plasma*. The positive ions are then accelerated towards the negative target and they transfer their momentum to the lattice of the solid. Neutral clusters (or atoms) are ejected and travel to the surface of the sample. Some permanent magnets are placed behind the target material in order to confine the charge particles of the plasma. They follow helical trajectories which allow producing more collisions with neutral gas atoms and so increasing the deposition rate performances.

The sputtering can be performed either in DC mode or in RF mode. The second one is preferred in case of oxides because the high DC voltage bias would charge up the insulating target preventing the correct hitting of charge particles on the material. During the deposition process the sample can be heated up to a certain temperature and it is kept in rotation in order to guarantee a better uniformity on the surface. The deposition rates are of the order of few nm/min and can be checked with a quartz microbalance in place of the sample.

4.2 Fabrication techniques

In order to produce suitable devices to perform magnetoelectric characterisation, after the deposition, the sample is processed. In particular, for the studies presented in the following chapters, standard Hall bars were fabricated on GeTe heterostructures. The entire workflow consists of three steps: optical lithography to pattern the samples, ion beam etching to remove the excess of material which is not needed for the device and finally thermal evaporation to deposit metallic contacts for bondings with an external chip.

4.2.1 Optical lithography

The idea of using ultraviolet (UV) light to selectively modify polymers to pattern devices dates back to the Forties, but it is still the most widely used form of lithography in the integrated circuits industry [137]. It consists in transferring a two-dimensional geometry

on the surface of a wafer using a mask and a *photoresist*, which is a polymeric material that changes its solubility properties when exposed to UV light. The result of a lithographic process is that the geometry is transferred on the sample in regions where the unsoluble photoresist is present and regions where it is not. This allows for successive deposition or etching steps on selected areas.

The steps of a lithographic process are the following [138] and they are depicted in figure 4.2:

(i) **Sample cleaning.** (figure 4.2 (a)) Contaminants could compromise the correct adhesion of the photoresist and so the efficacy of the lithography. The workflow takes place in a cleanroom and the sample is typically cleaned by ultrasonic agitation while it is immersed in acetone. This procedure is followed by a rinse in isopropanol, then the sample is dried and soft baked at $120 - 140\,°C$ to desorb water.

(ii) **Deposition of the photoresist.** (figure 4.2 (b)) The photoresist is deposited by spin coating. The sample is placed into a resist spinner where it is held by a vacuum chuck. The rotation is essential to have a uniform surface. The photoresist thickness depends on the choice of the speed and on the viscosity of the polymer. The resist used for the processes described in this work is the image reversal photoresist AZ5214E from Micro- Chemicals GmbH, with a thickness of $\sim 1.4\,\mu m$. After the deposition, a soft bake is performed at $100 - 120\,°C$ for one minute to evaporate the solvent and to increase the adhesion on the sample surface.

(iii) **Exposure.** (figure 4.2 (c)) The exposure to UV radiation changes the chemical properties of the photoresist. In the case of AZ5214E, the exposed regions become more soluble and they can be easily removed by development. The mask used to pattern the device could be a physical mask (typically made of chromium). Alternatively, one can use a maskless aligner (MLA) which focuses a laser in order to pattern the needed geometry without any mask (this is the case for the present work, performed with Heidelberg MLA100 instrument with a laser wavelength of 365 nm). The resolution of this step is about $1\,\mu m$.

It is also possible to proceed with an *inverse* lithography to obtain the negative of the patterning designed. This can be accomplished both with a proper negative photoresist or with a different procedure still with a positive one. In the latter case, the sample undergoes another baking process, said *reversal baking* (typically at $110 - 130\,°C$) for about $90 - 100\,s$. This procedure favours the diffusion of amines in the exposed regions, they neutralise the byproduct of the photodecomposition and make these areas resistant to further changes. Then, a flood exposure to UV light occurs and the areas not previously exposed become now soluble and the inversion of the pattern is reached.

(iv) **Photoresist development.** (figure 4.2 (d)) The development process is performed by a dedicated chemical agent, that removes the part of the photoresist which was made soluble. For the case of AZ5214E, the right agent is AZ726 MIF Developer from MicroChemicals GmbH. The typical development time is $30 - 50\,s$.

(v) **Etching or deposition process.** (figure 4.2 (e)) After the lithographic process, one can either etch the remaining part of the sample or perform a deposition process

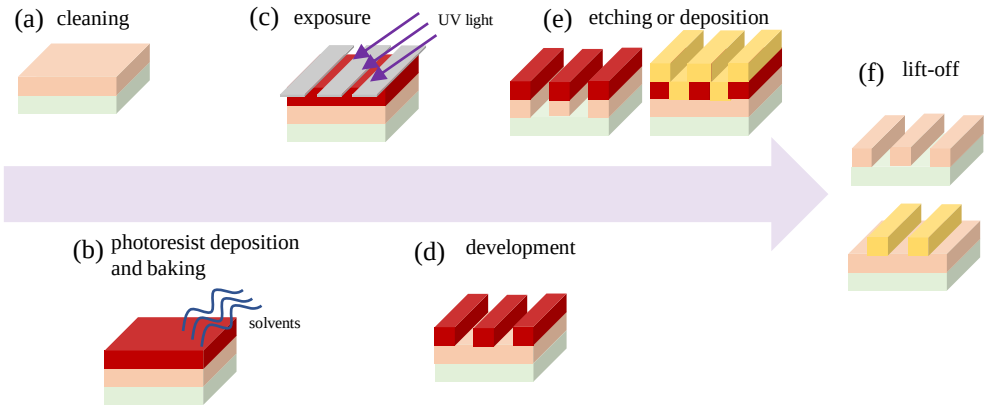

Figure 4.2: *Lithography workflow. (a) Sample cleaning; (b) Photoresist deposition and soft bake; (c) Exposure to UV light with a mask; (d) Photoresist development; (e) Etching or deposition process; (f) Lift-off procedure.*

(see next section). The photoresist protects the device from etching and prevents the adhesion of further material.

(vi) **Lift-off process.** (figure 4.2 (f)) Finally, it is possible to remove the photoresist through a lift-off or strip process. Also in this case, dedicated chemical agents can be used, from acetone to more specific products (for the case of AZ5214E, AZ100 Remover from MicroChemicals GbmH is suitable).

4.2.2 Ion beam etching and contact deposition

The technique of ion beam etching (IBE) is very similar to the one presented in section 4.1.2. It is a dry etching consisting in the sample material removal by transfer of momentum of accelerated argon ions towards the sample, which becomes now their target, in a vacuum chamber. In a discharge chamber, a hot cathode filament emits electrons by thermoionic effect, while the positively charged walls of the chamber act as anode. Electrons move towards them and ionised argon atoms. An accelerator grid forces the ions to move towards the sample, starting the etching process. Hence, the plasma generation and the acceleration are decoupled. During the process the sample is kept in rotation through the holder and the tilting angle between the sample and the incident flux can be opportunely tuned (being typically at 30°) in order to avoid that the etched material is redeposited onto the sample. The IBE process done in this work was performed with a Kaufman and Robinson KDC 160 Ion Source present in Polifab facility.

The deposition of metallic contacts relies on a process very similar to the one described in section 4.1.1. They were grown by thermal evaporation, in which sublimation of the target material is reached by heating it up by means of Joule heating with a DC current (without applying any high voltage). The deposition is carried out in a vacuum chamber and the rate of process can be monitored by two quartz microbalances. The system employed is a Moorfield MINILAB-080 present in Polifab facility as well.

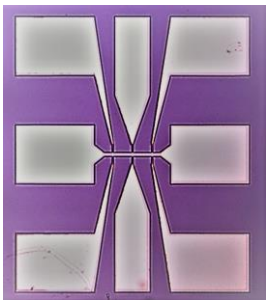

Figure 4.3: *A Hall bar device examined through an optical microscope after the whole fabrication process.*

4.2.3 Devices fabrication recipe: Hall bar geometry

As mentioned before, the devices needed for the investigation presented in the following are Hall bars. These structures allow for the injection of a current through a channel and for the possibility of detecting the transverse and the longitudinal resistance of it. The length of the channel is 100 µm, while the width 10 µm. The device is designed to have three transverse branches. In order to fabricate these devices two lithographic steps are needed. The final product is reported in figure 4.3. The recipe used is illustrated in the following.

1st step: inverse lithography for the definition of the Hall bar.

(i) Sample cleaning with acetone, followed by isopropanol;

(ii) Spin coating with AZ5214E photoresist with 6,000 rpm and 500 rpm/s (speed and acceleration) for 60 s. Soft bake at 110 °C for 90 s;

(iii) Exposure with MLA, with a dose of 25 mJ/cm^2. Reversal bake at 115 °C for 90 s and flood exposure with a dose of 125 mJ/cm^2;

(iv) Development with AZ 726 MIF developer for 30 s and water rinse;

(v) IBE to remove the uncovered regions of the sample for 30 min and photoresist stripping.

2nd step: direct lithography for the contact pads deposition.

(i) Sample cleaning with acetone, followed by isopropanol;

(ii) Spin coating with AZ5214E photoresist with 6,000 rpm and 500 rpm/s (speed and acceleration) for 60 s. Soft bake at 110 °C for 90 s;

(iii) Exposure with MLA, with a dose of 230 mJ/cm^2;

(iv) Development with AZ 726 MIF developer for $50 - 55$ s and water rinse;

(v) Thermal evaporation of the heterostructure composed by: Cr(10)/Cu(200)/Au(50) (numbers in nanometers) and photoresist stripping.

4.3 Spin- and angle-resolved photoemission spectroscopy

Photoemission spectroscopies are currently the most valuable tools to evaluate chemical composition and electronic properties of materials. Spin- and angle-resolved photoemission spectoscopy (SARPES) allows for mapping the electronic band structure in the

momentum space, reconstructing also the spin polarisation of such a bands. This is of fundamental importance in modern material science and spintronics. SARPES technique was exploited for the measurements of chapter 5, where the investigation on SnTe is illustrated together with the possibility of engineering its electronic properties. This section briefly illustrates the physical principle underlying ARPES (the spin polarisation detection is illustrated in chapter 3).

SARPES is able to retrieve the information needed to reconstruct the band structure from the analysis of photoemitted electrons. When light with a certain photon energy $h\nu$ irradiates a sample, electrons can be photoemitted. This happens when $h\nu$ overcomes the binding energy E_b and the potential barrier at the surface, namely the work function Φ. The kinetic energy, the outcoming angle of emission and the spin polarisation of electrons are directly linked to the set of quantum numbers describing the starting electronic state. A HEA permits the analysis of such a parameters, together with a suitable spin detector (the geometry is sketched in figure 5.4(a)). UHV conditions are needed both to avoid contaminations on the surface and to preserve photoemitted electrons from multiple scattering processes.

Even if the correct framework to treat ARPES process is a full-quantum approach, known as *one-step model* for photoemission spectroscopy, the physical principle can be easily understood relying on the so-called *three-steps model*, where the entire mechanism is splitted and approximated into three independent processes: the optical excitation of an electron, its propagation towards the surface and the emission in vacuum [139].

(i) **Photoexcitation.** If one considers a non-interacting electron system, the transition probability to witness the photoexcitation of an electron from an initial state ψ_i with energy E_i to a final state ψ_f with energy E_f is given by the Fermi golden rule:

$$W_\mathrm{if} = |M_\mathrm{if}|^2 \delta\left(E_\mathrm{f}(\mathbf{k}_\mathrm{f}) - E_\mathrm{i}(\mathbf{k}_\mathrm{i}) - h\nu\right), \tag{4.1}$$

where the delta-function accounts for energy conservation and the transition is assumed to vertical (i.e., $\mathbf{k}_\mathrm{i} = \mathbf{k}_\mathrm{f} =: \mathbf{k}$), while M_if is the matrix element of the Hamiltonian describing the interaction process ($H' \sim e/m\mathbf{A}\cdot\mathbf{p}$, with $\mathbf{A}$ the electromagnetic vector potential): $M_\mathrm{if} := \langle\psi_\mathrm{i}(\mathbf{k}_\mathrm{i})|\, H' \,|\psi_\mathrm{f}(\mathbf{k}_\mathrm{f})\rangle$. Thus, the internal photocurrent reads:

$$I(E_\mathrm{i}, \nu, \mathbf{k}) = \sum_{\mathrm{i,f}} |M_\mathrm{if}|^2 \delta\left(E_\mathrm{f}(\mathbf{k}_\mathrm{f}) - E_\mathrm{i}(\mathbf{k}_\mathrm{i}) - h\nu\right). \tag{4.2}$$

(ii) **Propagation.** Once electrons are excited, they are free to travel across the sample as free particles. The intensity in eq. 4.2 is reduced by the elastic and inelastic scattering processes. The characteristic length at which these scattering processes occur is the so-called *inelastic mean free path* (IMFP), which is an energy-dependent quantity generally described by a universal curve [140]. Its general expression is:

$$\lambda_\mathrm{IMFP}(E_\mathrm{kin}) = \frac{A}{E_\mathrm{kin}^2} + B\sqrt{E_\mathrm{kin}}, \tag{4.3}$$

with A and B coefficients which in general depend on the nature of the sample (metal, oxide, element, compound,...). For this kind of experiments $\lambda_\mathrm{IMFP} \sim 1$ nm. Hence, the transport probability factor reads:

$$D(E_\mathrm{kin}, d) = \exp\left(-\frac{d}{\lambda_\mathrm{IMFP}(E_\mathrm{kin})}\right), \tag{4.4}$$

where d is the distance travelled.

(iii) **Escape.** The escape is effective only if electrons overcome the work function of the material, which means that the kinetic energy of the photoemitted electron is:

$$E_{\mathrm{kin}} = h\nu - \Phi - E_{\mathrm{b}}, \tag{4.5}$$

as illustrated in figure 5.4(b). Since the surface represents a symmetry breaking with respect to the symmetry of the crystal, the wavevector of the electron is conserved only in its parallel component (see figure 5.4(a)). Hence, $\mathbf{k}_{\parallel}^{\mathrm{f}} = \mathbf{k}_{\parallel}^{\mathrm{i}} =: \mathbf{k}_{\parallel}$ and:

$$\mathbf{k}_{\parallel} = \sqrt{\frac{2mE_{\mathrm{kin}}^2}{\hbar}} \left[(\sin\theta\cos\varphi)\,\mathbf{e}_x + (\sin\theta\sin\varphi)\,\mathbf{e}_y \right], \tag{4.6}$$

with the angles defined in figure 5.4(a). So, the parallel component of the initial wavevector is easily obtained. The perpendicular component is not conserved, hence the initial value can be related to the measured one by:

$$k_{\perp,\mathrm{i}} = \sqrt{\frac{2m}{\hbar^2}\left(E_{\mathrm{kin}}\cos^2\theta + V_0\right)}, \tag{4.7}$$

where V_0 is a constant called *inner potential* and can be determined by photon-dependent measurements, fitting the periodicity along the $k_\perp$ direction [141]. In this way also the last component of the wavevector can be reconstructed. The energy dispersion relation is now fully mapped. Finally, the overall photocurrent reads:

$$I_{\mathrm{f}} = I(E_{\mathrm{kin}}, \nu, \mathbf{k}_{\parallel}) D(E_{\mathrm{kin}}, d) T(E_{\mathrm{kin}}, \mathbf{k}_{\parallel}), \tag{4.8}$$

where $T(E_{\mathrm{kin}}, \mathbf{k}_{\parallel})$ is the probability the electron has to escape through the surface.

In SARPES experiments the light source is typically chosen in the UV ($6 - 120\,\mathrm{eV}$) and the measurements are generally performed at normal emission, so the perpendicular component of the k vector is fixed by the photon energy, while the parallel is related to the photoemission angle. In this way the output of a typical measurement is the dispersion along $k_{\parallel}$ at point with a certain $k_\perp$.

The experiments collected in this thesis were performed during several beam-times at the Advanced Photoelectric Effect experiments (APE) beam-line of Elettra synchrotron in Trieste, Italy.

4.4 Magnetoelectric characterisation: harmonic Hall measurements

The technique described in this section regards transport measurements conducted during the period as visiting Ph.D. student of the author at ETH Zürich. It deals with harmonic Hall detection of magnetoresistive effects, measuring the longitudinal and the transverse components of the resistance. As discussed before, the devices investigated in this work have the geometry of Hall bars. With this kind of design it is possible to probe at the same time longitudinal and transverse resistance, while a current is injected through the channel. In a real experiment, what one can measure is the voltage drop between two contacts. In addition to linear effects (i.e., when the voltage measured is directly proportional to the current injected), a non-linear behaviour is expected for some signals. Hence, one

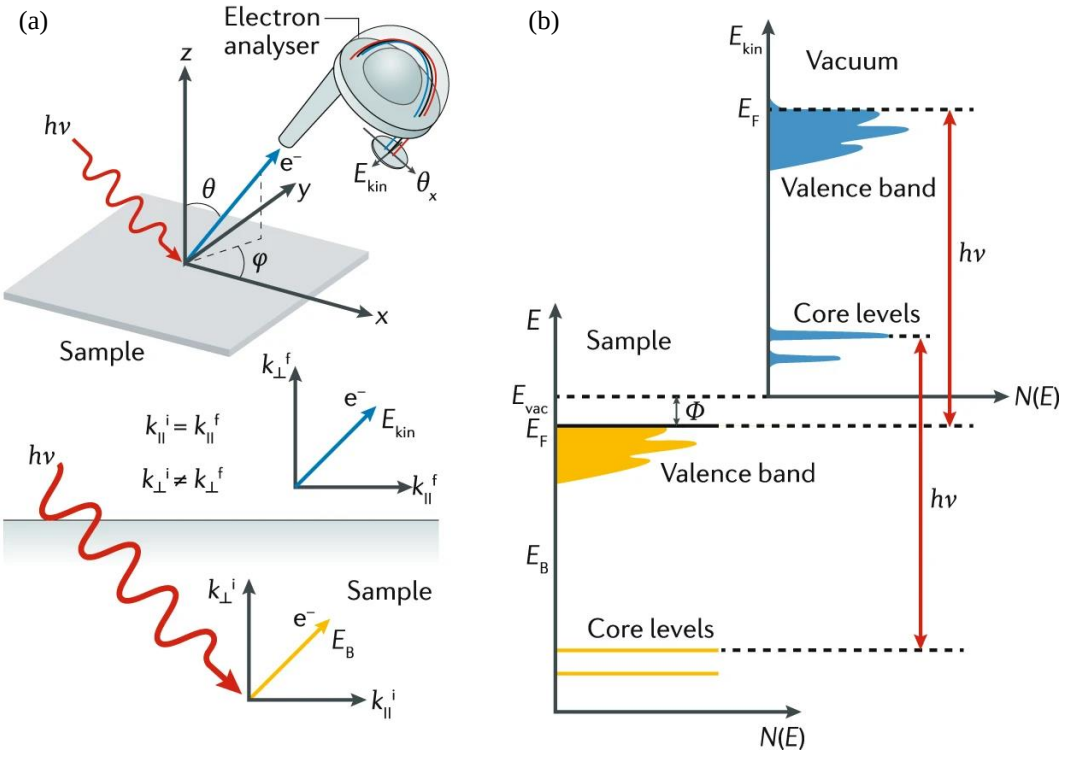

Figure 4.4: *(a) In the top part of the panel, geometry of ARPES experiment. When the light impinges on the sample a photoelectron is excited and collected by a HEA. In the bottom part of the panel, scheme of the k vector conservation when the electron crosses the surface; (b) Scheme of the energy levels of a photoelectron and graphical illustration of the Einstein rule for photoelectric effect described by eq. 4.5 (adapted from [141]).*

can write: $V_{\text{meas}} = \sum_i n_i V^i$, where n_i is the coefficient corresponding to the i-th order response. For the interests of this work, it is worth mentioning only second order contributions, which are induced by the applied current, as shown below. In sections 2.3.3 and 2.3.4, BMER for bare Rashba systems and SOT in bilayer heterostructures were reviewed. Both of them are current-induced effects appearing in the second order response of the resistance. Moreover, since measurements are performed constantly injecting a current, a Joule heating is induced in the material and, as a consequence, a temperature gradient ∇T develops into the device. Its direction is not known *a priori*. Since the heating process is proportional to the power generated, which in turn is proportional to the square of the current, thermal effects appear in the second order response as well. This makes them a possible issue in disentangling BMER and SOT contributions [97].

In order to conduct this kind of detection, either an AC or a DC current can be injected, but for the AC mode the signal-to-noise ratio is typically larger. Hence, this approach will be employed in the rest of the work. Independently of the geometry (longitudinal or transverse), an AC current of the form $I(t) = I_0 \sin(\omega t)$ generates a time-dependent voltage which reads [97]:

$$V(t) = R(t) I_0 \sin(\omega t), \tag{4.9}$$

where $R(t)$ is the (transverse or longitudinal) resistance which contains all linear and

non-linear contributions. One can write the resistance as:

$$R(t) = R(\mathbf{B}_0 + \mathbf{B}_I(t)), \tag{4.10}$$

where $\mathbf{B}_0$ accounts for all the static contributions such as the external, the effective anisotropy and the demagnetising fields, while $\mathbf{B}_I(t)$ all the current-induced (and hence dynamical) contributions and hence as the same oscillating functional dependence as the current. Expanding eq. 4.10 to the first order, one obtains:

$$R(t) \simeq R(\mathbf{B}_0) + \frac{\mathrm{d}R}{\mathrm{d}\mathbf{B}_I} \cdot \mathbf{B}_I \sin(\omega t). \tag{4.11}$$

Assuming a linear relation between the field $\mathbf{B}_\mathrm{I}$ and the current and substituting in eq. 4.9, one has:

$$V(t) \simeq I_0 \left[R_0 + R_\omega \sin(\omega t) + R_{2\omega} \cos(2\omega t)\right], \tag{4.12}$$

where the following definitions were introduced: $R_0 := \frac{1}{2}\frac{\mathrm{d}R}{\mathrm{d}\mathbf{B}_I} \cdot \mathbf{B}_I$, $R_\omega := R(\mathbf{B}_0)$ and $R_{2\omega} := -\frac{1}{2}\frac{\mathrm{d}R}{\mathrm{d}\mathbf{B}_I} \cdot \mathbf{B}_I$. It is noteworthy that R_ω is the conventional resistance given by a DC measurement, while $R_{2\omega}$ represents the modulation of the resistance due to current-induced non-linearities.

In appendix A the analytical expressions for SOT and thermal effects for the second order response are derived. All symmetries are clarified and it is possible to establish a methodology to disentangle the various contributions.

The set-up used for the measurements reported in the following chapters consists of an AC-DC constant current source Keithley 6221 to generate the AC current in the device, a National Instrument PXI 4461/4462 to acquire the signals, a motorised stage for the sample holder and an electromagnet able to generate fields up to 2 T, together with its power supply.

4.5 Magnetic characterisation of free-standing films: Faraday effect set-up

Since the free-standing samples described in chapter 5 have nanometric thicknesses, they present a low reflectivity making the Kerr response to polarised light very low. As a matter of fact, light is much more transmitted than reflected. Moreover, standard characterisation techniques such as vibrating sample magnetometry (VSM) or SQUID magnetometry catch a global signal not only due to free-standing magnetic films but also to magnetic material deposited on their support, making the two contributions not separable. So, one must rely on the measurement of the Faraday effect in order to magnetically characterise such devices.

Faraday effect causes the rotation of the polarisation of a linearly polarised light beam which is proportional to the projection of the magnetisation along the light path. This is caused by right and left circularly polarised light (which gives the linear polarisation) propagating at different velocities (the two refraction indexes are different). This phenomenon is known as circular birefringence and produces a *rotation* of the principal axis and the appearance of a non-zero *ellipticity*. It was discovered in 1845 by Faraday and can be completely understood, as Kerr effect, in the framework of the theoretical tools developed by Maxwell. The strength of the effect can be easily expressed through the relation: $\beta = VBd$, where V is called *Verdet constant* and depends on the material, B

is the effective magnetic field and d is the path where light and magnetic field interact. In terms of optical parameters, it is possible to obtain information about both the rotation and the ellipticity of light through standard Jones calculus.

In order to measure the magnetic response of the magnetic membranes, a Faraday set-up was developed during the thesis and it is depicted in figure 6.8. It consists in a laser light source at $\lambda = 635\,\text{nm}$, followed by a polariser placed at $\alpha = 0°$ (see figure) in order to obtain a linearly polarised light. The sample is mounted on a holder with a suitable hole and placed in such a way that the membrane is just in correspondence of the hole, to allow the light to cross it. Two coils surround the sample to generate the magnetic field which is swept from negative to positive values during the measurements. The angle θ can be changed to probe in-plane or out-of-plane magnetisation in order to always have a projection parallel to the light path, $\theta = 0°$ was used for out-of-plane configuration, while $\theta \simeq 17°$ for the in-plane one (this angle was optimised for the set-up to have the maximum possible projection). After that, a photoelastic modulator (PEM) working at 50 kHz is positioned, followed by another polariser placed at $\alpha = 45°$ and finally, the signal is detected by a photodetector. The presence of the PEM allows increasing the signal-to-noise ratio as well as giving the possibility to retrieve both polarisation rotation and ellipticity of the transmitted beam. They are proportional to the first and the second harmonic response, respectively [142].

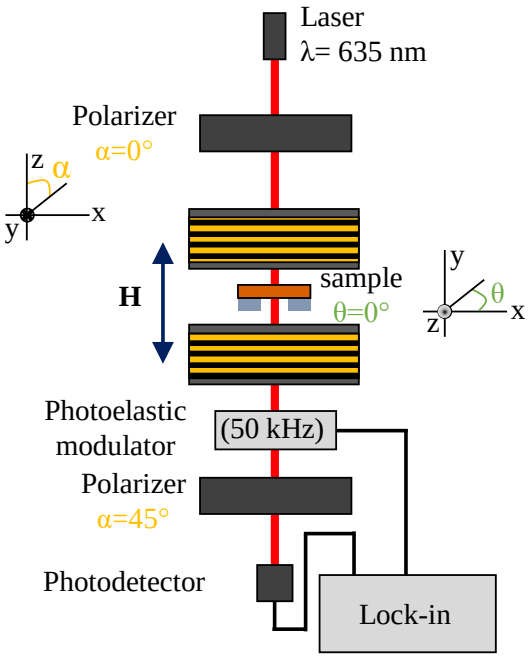

Figure 4.5: *Sketch of the optical set-up developed in order to detect Faraday effect in free-standing films.*

4.6 Spin-polarised electron gun

In the present section, the working principle of the spin-polarised electron gun described in [135] is presented. During the thesis activity, the author worked in order to restore the set-up and its performances and to carry out the spin filtering characterisation of the free-standing magnetic films.

The set-up is composed by a photocathode of GaAs in conditions of negative electron affinity (NEA) (prepared in chamber #5, see figure 4.1) which acts as spin-polarised electron source and by an electron gun made of a series of electrodes that can be set at different voltages (in the range $0 - 500\,\text{V}$) which focus the electron beam on the sample, in the same way that a series of lenses would do with a light beam (see figure 4.7). On the sample-holder it is possible to measure the absorbed current as well as the transmitted current through a Faraday cup electrode placed beyond the sample and kept at constant

positive bias ($\sim$ 30 V).

GaAs represents the most common choice to generate spin-polarised electrons. They are produced by exciting GaAs substrate with a laser radiation which is resonant or larger than the gap (1.422 eV at room temperature) and photoemitted after a vertical transition from the valence band maximum (VBM) to the conduction band minimum (CBM). The valence band is composed by atomic 4p-wavefunctions of As which suffer of SOC resulting in a splitted band structure. The CBM is composed by atomic 4s-wavefunctions of Ga, giving rise to a $4s_{1/2}$ state. With a suitable photon energy ($\sim$ 1.5 eV) one can just select the $4p_{3/2} \rightarrow 4s_{1/2}$ transition (see figure 4.7(a)). The initial state is fourfold degenerate ($m_i = \pm 3/2, \pm 1/2$). The selection rules for angular momenta permit only transitions with specific differences between quantum numbers. Due to angular momentum conservation, if one exploits circularly polarised light, the only transitions allowed are the ones with $\Delta m_i = \pm 1$. For instance, with left-handed circularly polarised (LCP) light, only $\Delta m_j = -1$ are allowed, so the transitions: $4p_{3/2}$ ($m_j = +3/2$) $\rightarrow$ $4s_{1/2}$ ($m_j = +1/2$) and $4p_{3/2}$ ($m_j = +1/2$) $\rightarrow$ $4s_{1/2}$ ($m_j = -1/2$). Hence, both spin states ($\pm$ 1/2) are present in the conduction band after the excitation. Nevertheless, the probability for the former transition is three-times larger with respect to the latter one (the scheme of the bands is sketched in figure 4.7(a)). Therefore, one can obtain a spin polarisation of $P = (3-1)/(3+1) = 0.5$,[1] with the sign dependent on the chirality of the light polarisation (LCP or RCP) which is established by a standard Pockels cell. The $+$ sign indicates that $+1/2$ electrons are the dominant channel, when the polarization is reversed to RCP, P results -0.5 and $-1/2$ electrons dominate. In the present set-up, the value of the polarisation experimentally measured is $P = 0.25 \pm 0.02$, with a wavelength of the excitation laser of 808 nm (the value does not reach the expected maximum both because the energy is not precisely resonant and a depolarisation process occurs in the gun). In order to obtain the NEA conditions, heavily p-doped GaAs substrates are chosen and then their surface is treated to get a layer of Cs_xO_y with a tested procedure [143] consisting in alternating Cs and O_2 exposures producing an increasing but oscillating photocurrent (due to the overexposure of both Cs and O_2), until a plateau is reached.

Once electrons are photoemitted, they have the spin normal to the surface. An electron gun allows to collect them and rotate their momentum, without changing their spin polarisation. In this way, it is possible to have the spin perpendicular to momentum. So, in-plane magnetised samples can be probed with the beam impinging normally to the sample surface. In order to study the propagation of a beam of charge particles such as electrons, the Liouville theorem can be exploited. Supposing that the current is not too large, the assumption that the charges are not interacting with themselves holds. In this situation, it is possible to simulate the behaviour of the electrons when electrostatic lenses, which are composed by two cylindrical electrodes, are acting on them [135]. As illustrated in figure 4.7(b), the photocathode is kept at ground, the electrons are emitted and accelerated through an anode (A) and a Herzog plate (HP) to $\sim$ 300 eV, then a spherical capacitor with an internal and an external sphere (Si and Se) allows the rotation by 90° of the beam. In this way, the momentum is perpendicular to their spin. Then, a system composed by three electrostatic lenses (E1, E2 and E3) slows down the electrons at $\sim$ 70 eV and finally the last two electrodes (E4 and E5) together with an external one

[1] In this discussion the case of a cubic GaAs crystal is taken into account. Actually, it is possible to enhance the polarisation up to $P = 1$ using a distorted lattice. This is not considered for the aims of this work, since only cubic crystals were exploited.

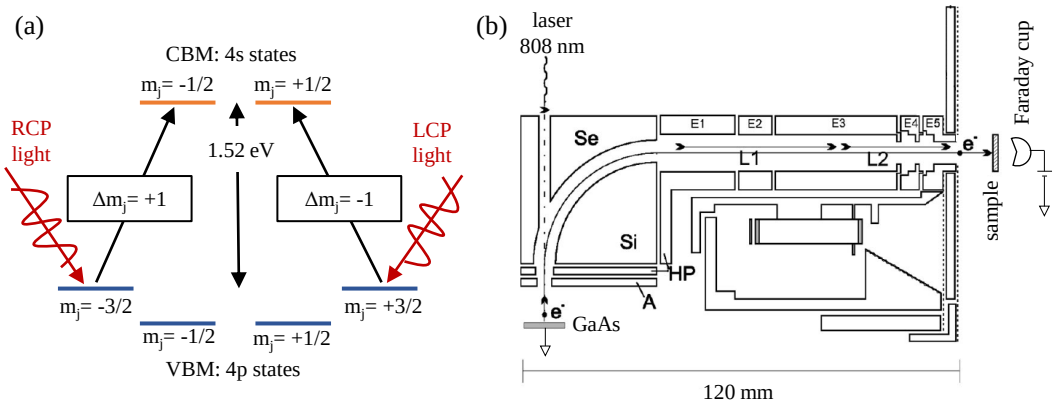

Figure 4.7: *(a) Band diagram near the band-gap of GaAs and allowed transitions in the case of RCP and LCP laser light of energy* $\sim$ 1.5 eV*; (b) Schematic of the spin-polarised electron gun (adapted from [135]).*

determine the final energy of the beam, which is between $\sim 5 - 50$ eV, and the focus on the sample. The bias of the sample is then spanned through the range $\sim 2 - 25$ eV, that is the final energy which electrons hit the sample with, to perform energy scans. The typical value of the photoemitted current is $\sim 10\,\mu$A, while both the transmission and the full width at half maximum (FWHM) of the beam spot (which has a gaussian profile) are energy-dependent. The optimised values are $\sim 70\%$ and ~ 1 mm for electrons kinetic energies larger than ~ 10 eV.

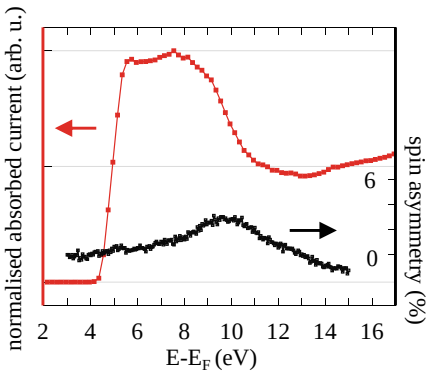

Figure 4.6: *Absorbed current spectroscopy of MgO/Fe(001)-p*(1×1)*O sample, together with the measurement of the asymmetry in correspondence with the gap present in the conduction band where minority and majority spins are splitted.*

The set-up was tested performing an absorbed current spectroscopy (ACS) measurement, preparing a very common sample, which is MgO/Fe(001)-p(1×1)O. This sample is known to have a large spin asymmetry in coincidence with the appearance of a gap in its conduction band structure [34, 129]. In figure 4.6 the result of the measurement is reported, the absorbed current presents a steep edge at 4.5 eV due to the work function of the material, then around 10 eV it decreases down to half of the maximum value, due to a gap in the conduction band, meaning that there are less states to let the electrons absorbed. At this gap the the minority and majority bands are splitted and this produces the asymmetry depicted. The measurement was performed modulating the applied voltage to the Pockels cell and so switching between RCP and LCP light and detecting the absorbed current demodulating with a lock-in amplifier.

CHAPTER 5

Spin- and angle-resolved photoemission spectroscopy and bands engineering in Ge-doped SnTe films

In this chapter the growth and the spectroscopic measurements on Ge-doped SnTe thin films are presented. As discussed in chapter 2, this material was shown to provide a multi-functional platform for new phenomena. This is possible due to the coexistence of several mechanisms at the same time.

A lot of works were published in the past ten years, but all of them are focused on the prototypical nature of SnTe as TCI [72, 144, 145]. The low Curie temperature (98 K, for bulk SnTe) made ferroelectricity not exploitable in devices. The interest in employing SnTe as a ferroelectric material was raised in refs. [113, 117], showing the possibility to obtain a stable polarisation vector at room temperature in the ultra-thin film limit.

The engineering of energy bands seems to reveal promising effects on SnTe thin films. In particular, in ref. [112] it is shown how, changing the distorsion parameter of the lattice, it is possible to span through different states which bring non-trivial topology (see section 2.4 for details) together with the appearance of ferroelectricity and bulk Rashba effect (the material becomes a FERSC). The purpose of this chapter is to show, exploiting germanium as a dopant element, how it is possible to distort the bulk SnTe lattice in order to obtain intermediate configurations in which different phases coexist also at room temperature in the bulk crystal alloy $Sn_{1-x}Ge_xTe$. The two extremes of the series are SnTe ($x = 0$), which is a paraelectric TCI and GeTe ($x = 1$), which is well-known to be a FERSC. Density functional theory (DFT) calculations performed by co-workers for this systems are employed in order to compare the results of SARPES experiments. Some intermediate configurations were obtained, showing the possibility to tune the bulk Rashba bands and, indirectly, ferroelectricity.

This platform represents also an ideal playground to display at the same time Rashba effect and topological surface states (TSS) resembling the TCI properties which SnTe is well-known for. The presence of two channels which in principle can be sources of spin currents could bring a breakthrough in spin-orbitronics, with a lot of potential application in SOT-based device where spin-to-charge conversion plays a fundamental role.

The growth optimisation and the structural characterisation was performed at Polifab facility of Politecnico di Milano with the help of Alessandro Novati and Federico Belponer (Master students) who also contributed to the spectroscopic characterisation. The SARPES and XPS experiments were performed at APE beam-line of Elettra synchrotron of Trieste and were in part performed also with the help of Federico Fagiani (Ph.D. student).

The chapter is organised as follows: in section 5.1 the deposition process of such films is presented, then the doping process with germanium is studied in section 5.2.1. The spectroscopic measurements are presented in section 5.2.2 for what regards angle-resolved spectroscopy and in section 5.2.3 for what regards spin-resolved measurements. A discussion of the results together with a comparison with theoretical calculations is presented in section 5.3.

5.1 Samples growth, preparation and post-treatments

Since the aim of this preparation is the possibility to dope SnTe films with germanium with different concentrations and to try to stabilise a ferroelectric phase also at room temperature to unveil the FERSC nature of such a compound, the most natural choice for the substrate is GeTe(111) grown on Si(111) [133]. GeTe in the rhombohedral α phase has a very similar structure to α-SnTe. The lattice constants are comparable ($a_{\mathrm{GeTe}} = 4.373$ Å and $a_{\mathrm{SnTe}} = 4.537$ Å, with a lattice mismatch of just $\sim 4\%$) and, even more interestingly, the intrinsic ferroelectric polarisation of α-GeTe could contribute – by dipolar interaction – to the stabilisation of the α phase of SnTe which is ferroelectric too.[1]

Starting from GeTe(18 nm) substrates capped with a layer of Te, they were re-prepared with a reliable decapping protocol in UHV (composed by Ar^+ ions sputtering and thermal annealing (at 250 °C for $\sim$ 30 min), crossed-checked with XPS measurements) which is described in details in appendix B. When the pristine GeTe surface is restored, SnTe stoichiometric film was evaporated by MBE on this substrate, from a SnTe crystal. The pressure of the chamber during the process was $\sim 4 \times 10^{-10}$ mbar, while the sample was kept at 200 °C. The stoichiometry and the crystallinity of the samples were checked by XPS and X-ray photoelectron diffraction (XPD). Figure 5.1(a) shows the comparison between normalised XPS intensities between GeTe substrate and the SnTe film deposited, while figure 5.1(c-d) presents the crystal structure along ZA direction and the relative XPD signal, revealing a high crystal quality, with the main crystallographic directions showing a clear peak (empty symbols for the pre-annealed film). XPD unfortunately does not allow to distinguish between α and β phases, since the predicted shift is just 0.3°

[1] There are other possible choices for the substrate. Firstly, it was shown the possibility to grown epixial SnTe on Si(111) in ref. [145]. Then, another natural choice for is BaF_2 (111). Such a substrate is commonly employed to deposit high quality (111)-oriented chalcogenides like Ge(Mn)Te [146] and Bi_2Te_3 [147] and group-IV compounds. The lattice parameter is 4.381 Å which almost perfectly matches the one of SnTe. The growth of samples on BaF_2 was optimised during the Ph.D. work to be exploited for transport measurements. The details of the deposition process as well as on the characterisation of such thin films is not treated in this work since the focus is on the engineering of band structure with doping and on SARPES measurements, which actually suffer from severe charging due to the insulating properties of BaF_2 with respect to GeTe, which is almost metallic.

while the resolution of the technique is around 1°. Afterwards, the surface morphology was imaged *ex situ* with AFM (the average roughness was < 1 nm) (see figure 5.1(b)).

The doping process was performed through a thermal annealing. When the sample is heated up to 250 °C, both Ge and Te atoms of the substrate can interdiffuse. This provokes a percentage of Ge to establish in the SnTe matrix, even substituting Sn atoms or filling Sn vacancies in the SnTe layer, naturally present in such a semiconductor. After this process, the stoichiometry is carefully checked again through XPS and also the crystallinity is investigated through XPD (see figure 5.1(d), full symbols). The crystal quality was found to be very high for SnTe thicknesses from 3 to 20 nm and the average roughness always less than 1 nm (measured on uncapped samples) similarly to the pre-annealed case. After spectroscopic and diffraction characterisation, samples were capped *in situ* with a film of $\sim$ 20 nm of Te, which resulted to be amorphous, in order to be carried to synchrotron facility to perform SARPES measurements, preserving their surfaces. The re-preparation of samples surface before spectroscopic experiments at the beam-line was performed again following the decapping protocol used for the substrates and illustrated in appendix B. It was able to restore the clean SnTe surface showing a high crystal quality (in figure 5.1(e) is shown the LEED hexagonal pattern).[2]

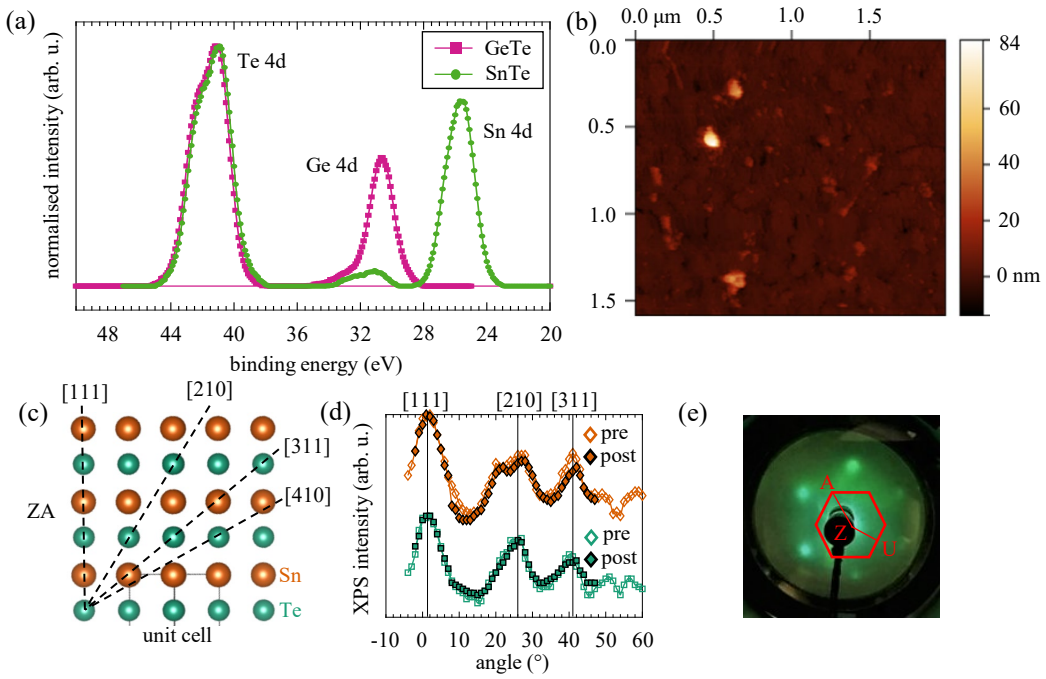

Figure 5.1: *Growth and preparation of SnTe samples. (a) Comparison between XPS spectra between the GeTe substrate before the growth and SnTe film after* 15 nm *deposition; (b) Morphology of the surface of a SnTe film measured by AFM ex situ; (c) Atomic arrangement in the crystallographic plane of SnTe corresponding to ZA direction; (d) XPD signal for Te and Sn peaks, pre- and post-annealing (empty and full symbols, respectively); (e) LEED pattern after the restoring of the SnTe surface, immediately before SARPES experiments.*

[2]For this re-preparation of the surface the samples undergo a second thermal annealing process at 250 °C. This is the temperature which the interdiffusion takes place at. Spectroscopic analysis confirmed the same stoichiometry ratio before and after this surface re-preparation, meaning that the equilibrium configuration of the crystal structure of the sample was reached and no more interdiffusion took place.

5.2 XPS and SARPES measurements on Ge-doped SnTe

In the following, spectroscopic measurements are presented in order to quantify the reached doping level of the sample and to investigate the band structures of such alloys. The first analysis was conducted by XPS, while the second one by SARPES. Both of them were performed exploiting synchrotron radiation after the decapping procedure and *in situ*.

5.2.1 Doping concentration

Exploiting the doping process with germanium described in the previous section, the amount of the dopant element was controlled by carefully tuning the thickness of the SnTe layer. In particular, given a fixed value for the thickness of the seed layer of GeTe equal to 18 nm, the amount of germanium which diffuses into this layer at a fixed temperature is constant. Hence, increasing or decreasing the thickness of the SnTe layer it is possible to vary the relative concentration of Ge, named x. The thickness of SnTe was spanned between 3 and 20 nm.

XPS measurements were performed in order to quantify the concentrations of the three different components of the alloy $Sn1-xGe_xTe$, namely Te, Sn and Ge. The spectra were acquired at different photon energies. The analysed peaks are the low binding energy peaks Te_{4d}, Sn_{4d} and Ge_{3d}. Their intensities were normalised by the IMFP, the cross section and the analyser transmission. The relative composition was retrieved with the following formula:

$$\frac{C_a}{C_a + C_b + C_c} = \frac{\left(\frac{I}{\sigma \lambda_{\mathrm{IMFP}} T}\right)_a}{\left(\frac{I}{\sigma \lambda_{\mathrm{IMFP}} T}\right)_a + \left(\frac{I}{\sigma \lambda_{\mathrm{IMFP}} T}\right)_b + \left(\frac{I}{\sigma \lambda_{\mathrm{IMFP}} T}\right)_c}, \tag{5.1}$$

where C stays for the concentration and labels a, b and c refer, case by case, to Te, Sn and Ge.

The photon energy chosen was 70 eV. The IMFP for the peaks taken into account covers a range from $\sim$ 0.44 to 0.55 nm. Hence, the technique is very surface sensitive and $t_{\mathrm{alloy}} > 5 \cdot \lambda_{\mathrm{IMFP}}$, for every sample. Hence, from now on, only the alloy is considered in the analysis, disregarding the contribution from the substrate (GeTe).

The samples which enter in this analysis are labelled ST1, ST2, ST3 and GT (which is a pure GeTe film employed as a reference sample) and are summed up in table 5.1. The XPS results at 70 eV are reported in figure 5.2, normalised to the cross sections, the IMFP, the analyser transmission and re-scaled to the tellurium 4d peak. The germanium concentrations given by eq. 5.1 are 31.3% $\pm$ 4.6%, 43.0% $\pm$ 3.0% and 54.2% $\pm$ 1.4%, for samples ST1, ST2 and ST3, respectively.

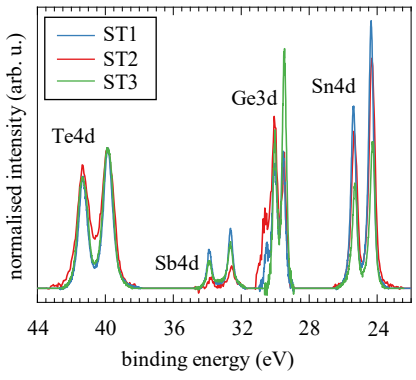

Figure 5.2: *XPS spectra of the $Sn1-xGe_xTe$ alloy measured at* 70 eV *normalised to the cross sections, the IMFP and the analyser transmission for samples ST1, ST2, ST3.*

Sample label	x (Ge concentration (%))
ST1	31.3 ± 4.6
ST2	43.0 ± 3.0
ST3	54.2 ± 1.4
GT (reference)	100

Table 5.1: *Ge-doped SnTe samples with the relative concentrations of Ge of the final compound* $Sn_{1-x}Ge_xTe$.

The concentrations were also checked varying the photon energy (up to 435 eV). This means sensing deeper regions of the crystal. The Ge concentration was observed to stay constant in the error bar reported in table 5.1, demonstrating that the samples are homogeneous with respect to the concentration of their elemental components. Since the thickness of the samples probed with ARPES is very similar to the one probed with X-ray at 70 eV, it is possible to rely on the concentration data reported above.

As a final remark, in figure 5.2, Sb_{4d} peak is also visible, this is the result of the interdiffusion of a monolayer of antimony used for the Van der Waals epitaxy of the GeTe substrate on Si(111) [133]. This arises because of the thermal annealing of the sample too. Previous experiments confirm that this additional element does not influence the output of spectroscopic measurements, so in the following it is not taken into account.

5.2.2 Mapping the energy band structure

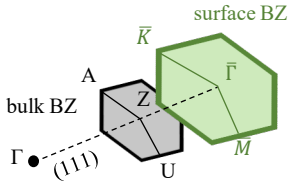

Figure 5.3: *Bulk and surface Brillouin zone of SnTe, showing only the* ΓZ *direction and the perpendicular ZAU plane and the relative plane for the surface states.*

Experiments regarding angle-resolved photoemission spectroscopy were carried out at APE beam-line at Elettra synchrotron of Trieste during several beam-times. In order to probe energy bands in the ZAU plane of the Brillouin zone (see figure 5.3), the photon energy for the experiments was selected in the range $h\nu = 14 - 25$ eV.[3] ARPES spectra for sample ST1 (which is the one with lowest concentration of Ge (31.3%), so the one which less resembles the behaviour of GeTe, the reference FERSC), acquired along the ZA direction and at $T \simeq 77$ K, are reported in figure 5.4. The photon energies used are 14, 16, 18, 20, 22.5 and 25 eV. Slightly changing the photon energy value and hence moving back and forward in the ΓZ direction, it is possible to identify two contributions in the energy range immediately below the Fermi level ($0 - 1.5$ eV):

- The first one (highlighted in purple) resembles the form of Rashba bulk bands (BB). It is completely visible at 25 eV and then it rigidly shifts towards the Fermi edge when the photon energy is decreased (the purple dashed line follows the top of this

[3] The distance ΓZ is not known *a priori*, but it is possible to rely on calculations on GeTe crystals where $3\Gamma Z = 2.73$ Å^{-1} and the actual photon energy value to probe the ZAU plane is $h\nu = 18$ eV. *A posteriori* a very similar value was found also for the samples analysed in this work.

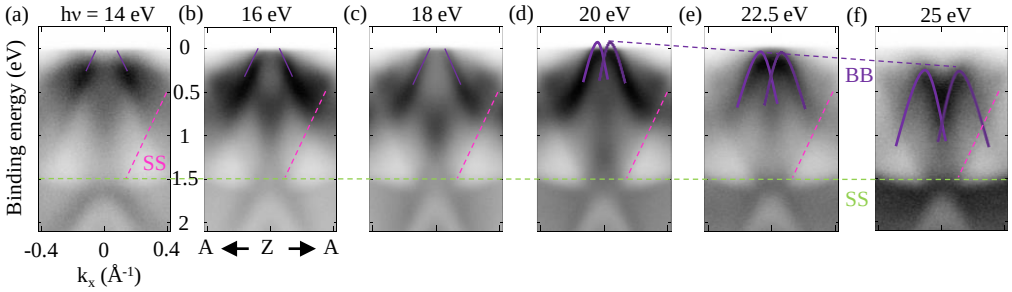

Figure 5.4: *ARPES measurements of Ge-doped SnTe samples. (a-f) Carpets along the ZA direction at different photon energies for the sample ST1, from* 14 *to* 25 eV. *The purple dotted line highlights the shift of bulk Rashba energy bands shown with solid lines, while pink and green dashed lines displays surface states which do not shift.*

contribution), making the vertices of the parabolas no more visible. At 14 eV only the tails of these states are below the Fermi level.

- The second contribution consists of bands marked by dashed pink and green lines and in the blurred states present close to the BB. These bands are not shifting with the photon energy. They are surface states (SS) which are present in three forms: a blurred band present at around 1.5 eV (green line), a cone-like shaped band (pink line), whose centre lays around at $E_{\mathrm{b}} \simeq 1.5$ eV and a blurred region around 0.5 eV.

Figure 5.5 shows the integration in k of the carpets in presented in figure 5.4, better visualising the energy-dependent shift of BB.

The comparison between different concentrations of Ge is presented in figure 5.6 for sample ST1 (31.3%) (a), ST2 (43.0%) (b), ST3 (54.2%) (c) and the reference sample GT (d). The measurements are taken at $T \simeq 77$ eV. The photon energy of 20 eV was selected for this comparison because it represents a trade-off between the possibility to be very close to the ZAU plane and to have a good resolution bands at low binding energy. Two important observations follow. Firstly, it is noteworthy how Rashba BB present an increasing broadening going towards the GeTe limit, making the separation of the Rashba sub-bands more explicit. Then, it is possible to notice how the SS with a cone-like shape progressively disappear again moving towards the pure FERSC behaviour of GT sample in favour of very marked SS at large k vectors, already detected in previous reports [22, 108]. The first consideration indicates the presence of a tunable Rashba strength. Bulk Rashba effect is a direct consequence of ferroelectricity in such compounds, so this represents and indirect proof of its presence, even for sample ST1, closer to SnTe.

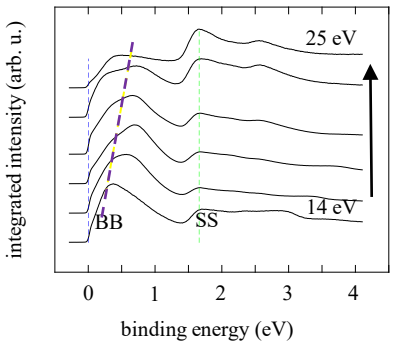

Figure 5.5: *Integrated counts for the carpets shown in figure 5.4 underlining the bulk and the surface contributions to energy bands.*

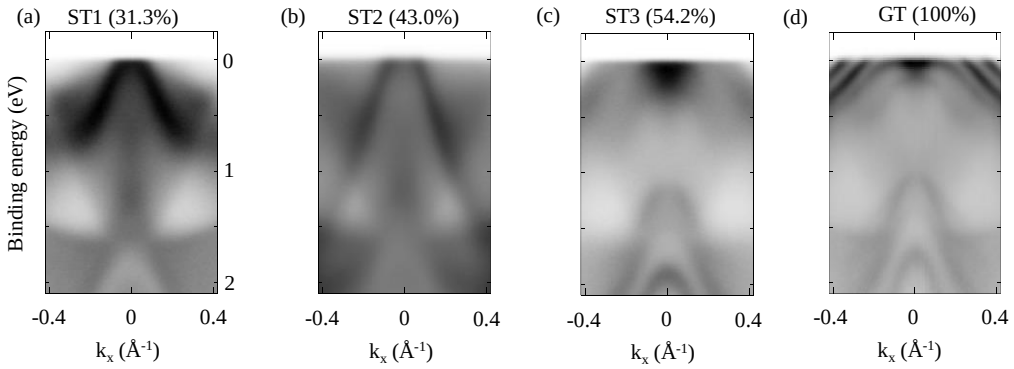

Figure 5.6: *(a-d) Carpets for the different samples ST1, ST2, ST3 with different Ge concentrations, compared to the reference of sample GT [22]. The photon energy is the same for every sample, fixed at* 20 eV.

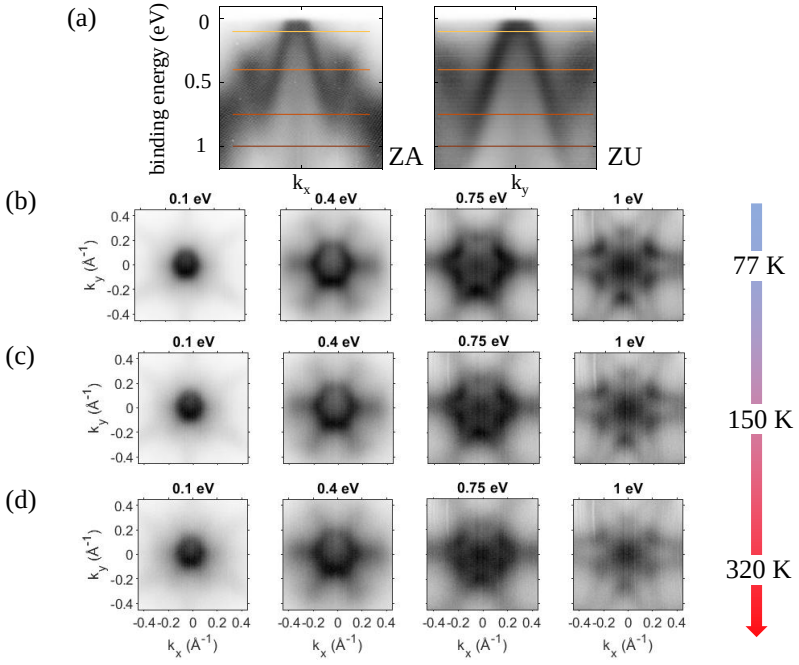

Figure 5.7: *Temperature dependent ARPES measurements. (a) Carpets along ZA and ZU directions with different energy cuts reported in the following panels; (b-c-d) Iso-energy cuts at* $0.1 - 0.4 - 0.75 - 1$ eV *at* $77 - 150 - 320$ K. *No relevant differences are displayed. The sixfold symmetry and the Rashba bulk bands are preserved.*

A further study is needed in order to understand the behaviour of such an alloy. In particular, the study of the evolution with temperature of the bands displayed before is of fundamental importance in order to establish if the doping mechanism allows to measure bulk Rashba bands also at room temperature. For this purpose, all the samples were measured up to $T = 320$ K. In figure 5.7, the results for sample ST1 are displayed.[4] In panel (a) are presented the carpets along the crystallographic directions ZA and ZU, with

[4]Data for other samples are not shown here, but they present similar results. ST1 was preferred since it is the one with a lower amount of germanium and so the one which is closest to the behaviour of bare SnTe, which has a Curie temperature of 98 K.

four iso-energy cuts in the (k_x, k_y) plane reported at three different temperatures ($T = 77 - 150 - 320$ K) in panels (b)-(c)-(d). They do not present any remarkable difference, apart from an increasing blurring of the scans, due to the decreasing of the signal-to-noise ratio of the measurement going to higher temperatures. The sixfold symmetry is evident both for bulk (the central darker hexagon) and surface states (the lighter six-pointed star). The features of bulk Rashba bands are preserved. These experimental evidences suggest that the Curie temperature of these films is increased to a temperature not smaller than room temperature.

5.2.3 Spin-resolved ARPES of bulk Rashba bands and surface states

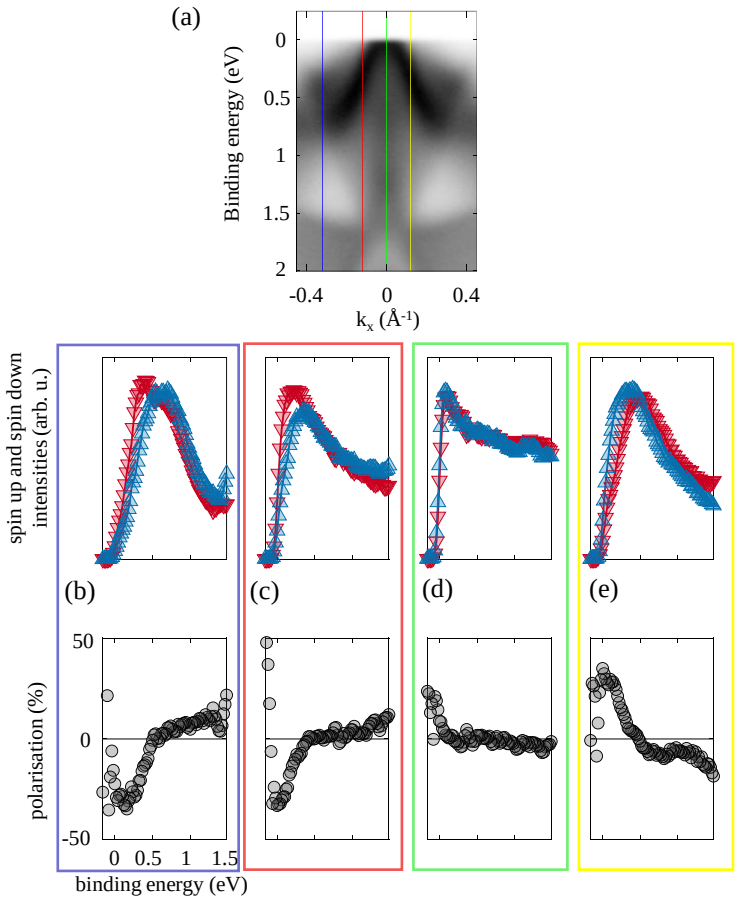

Figure 5.8: *SARPES measurements on ST1 sample. (a) Carpet at* 20 eV *and* 77 K *along the ZA direction. The coloured lines indicates the k vectors which the spin-resolved measurements were performed; (b-c-d-e) Spin dependent measurements performed with a VLEED detector, in the upper panels* I_{up} *and* I_{down} *are shown, while the spin polarisation is presented in the bottom panel, calculated with equation* $P = A/S$*, where* A *is the asymmetry and* S *the Sherman function (see chapter 3 for details).*

To further characterise the Rashba physics of the bands described in the previous section, spin-resolved measurements were performed at different points of the reciprocal space, to get information about the orientation of the Rashba contours of BB and about the polarisation of SS. The measurements were performed at fixed k_x and k_y, while the

energy is scanned from beyond the Fermi level up to $\sim$ 1.5 eV excluding the deeper region that presents blurred states whose spin is not known. The results are shown in figure 5.8 again for sample ST1 at 77 K. Panel (a) presents the carpet at 20 eV with four vertical lines denoting the k_x values which the spin lines are measured at.

Panels (b)-(c)-(d)-(e) show the spin polarised acquisitions for four fixed k_x vectors. The spin polarisation is calculated from the counts of the up and down intensities which give the asymmetry, by exploiting equation 3.13 (in the limit of reaching the Fermi edge, signals go to zero giving an unphysical effect of diverging polarisation). Panel (d) (green line) intersects Rashba bands precisely in the centre and hence it does not reveal any spin polarisation. Panels (c) and (e) (red and yellow lines) intersect Rashba bands at negative and positive k vectors, respectively. From Rashba effect theory (see section 2.2), the two parabolas present different spin polarisation and, due to spin-momentum locking, the spin direction is opposite for opposite k vector. This can be observed at $\sim$ 0.25 eV: moving from the Fermi level towards higher binding energies, the spin up polarisation appears before the spin down one and the other way round happens for opposite k vector. Finally, panel (b) shows a spin line taken where only surface states are present. Also in this case, a spin polarisation is displayed at 0.5 eV. This means that also the cone-like states are spin polarised. This observation would hint a topologically non trivial nature of such states. As a matter of fact, according to the calculations shown in the work by Plekhanov *et al.* [112], the presence of TSS which resemble the TCI properties of SnTe is sustained only up to low doping level, which is not the case for sample ST1 (31.3%) and such states were found to appear at very low binding energies, intersecting the Fermi level. Thus, it is possible to interpret them as Rashba surface states.

5.3 Discussion

The results illustrated in the former sections demonstrate the possibility to operate on SnTe doping, engineering its energy bands. In particular, the possibility to reach an intermediated state between cubic SnTe and the FERSC GeTe was shown. If ref. [112] predicted this situation tuning the distorsion parameter, an analogous result was reached by Ge-doping this material. Density functional theory (DFT) calculations were performed by co-workers of the author in order to fit the experimental data presented here. The results are reported in figure 5.9(a). As function of Ge concentration, the Rashba k vector (the k vector which the valence band is maximum at) and the Rashba parameter are plotted for bulk Rashba bands along the ZA direction. It is possible to note that – a part from the abrupt discontinuity in α_{R} (as a matter of fact, cubic SnTe ($x = 0$) does not display ferroelectricity and thus it does not support Rashba bands) – while k_{R} monotonically increases with the Ge concentration, α_{R} presents two maxima. One for very low doping concentration (5%) and the other one for bare GeTe. The minimum lays at 50%. Hence, a tuning of the Rashba effect is predicted, and through the induced modified distorsion also a tuning of the ferroelectric properties of such an alloy.

As experimentally found by ARPES, k_{R} increases, increasing the amount of germanium of the alloy. The extimation of the Rashba k vector inferred from experimental data is reported compared to DFT calculations in figure 5.9(b), demonstrating a trend comparable to the one expected. In order to estimate α_{R} a clearer ARPES signal is needed. Qualitatively, while ST1 and ST2 are in the central minimum and they do not show any

clear difference, ST3 and the GT reference presents a clear broadening of the bands, which is a net indicator of a trend comparable to the calculated one also for the Rashba parameter.

Hence, the presence of bulk Rashba effect is unambiguously demonstrated even at room temperature. Moreover, the strict link between Rashba states and ferroelectricity makes this an indirect proof of the enhancement of the Curie temperature up to room temperature with respect to bulk SnTe films. This represents an achievement dealing with SnTe which seems to display them not only at cryogenic temperatures or at the two-dimensional limit, as demonstrated so far.

What DFT calculations also show is that in the low doping regime (5-20%) the material presents a larger Rashba effect, even with respect to bare GeTe, while surface states with a non trivial topology of TCI bare SnTe survive [112]. Moreover, in this regime the energy band gap is strongly reduced and the material is no more considerable as a semiconductor. This regime was not investigated in this work, but it represents a very interesting perspective, where bulk and surface states (which in principle both could provide spin-to-charge conversion) have an important role in conduction.

This work opens the way on further studies on this new class of materials and promises future breakthroughs in the field of spin-orbitronics.

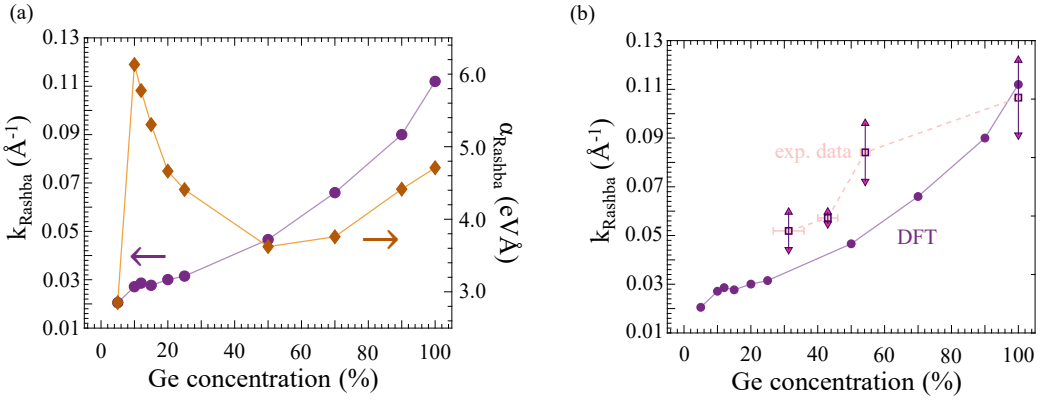

Figure 5.9: *(a) DFT calculations of the k_{Rashba} (left axis) and the Rashba parameter α_{R} (right axis) according to the Ge concentration; (b) Comparison between the calculated k_{Rashba} and the extracted value from experimental data.*

CHAPTER 6

Design of a two-dimensional spin detector based on free-standing magnetic membranes

The previous chapter finished with the analysis of some spin lines in the E-k space in order to understand the spin polarisation of Rashba bands and the chirality of their contours. Since APE beam-line is equipped with a one-dimensional VLEED detector (see chapter 3), it is possible only to fix the k vector value and scan the energy with the analyser obtaining a measurement which is actually pointwise. Figure 6.1 shows a spin map of sample ST2 (see section 5.2.1 for details on the system) composed by the collection of several spin lines at different k vectors (as the one highlighted in the figure) which nicely gives an overview along a certain crystallographic direction of the spin-resolved band structure in E-k space. Nevertheless, the measurement is very time demanding, requiring several hours for a statistically significant map. In the following, to go beyond VLEED detection, a new technology is described and a prototype device is realised.

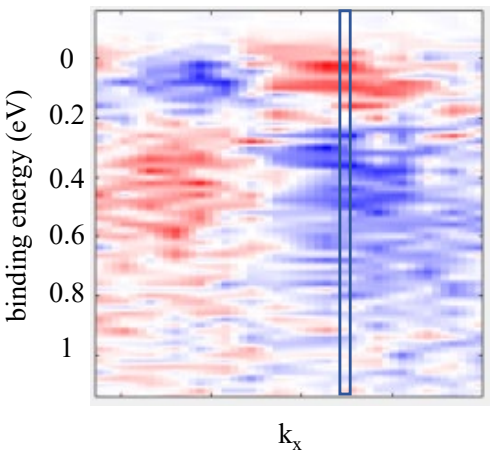

Figure 6.1: *Energy-k vector spin map of Rashba bands of ST2 sample collected with the VLEED detector of APE beam-line. A single spin line is highlighted.*

This chapter deals with the design of a two-dimensional matrix of free-standing magnetic membranes, starting from the conception of the suitable general heterostructure, to

its practical realisation and its characterisation. Even if what was realised is a proof-of-concept device, taking advantage of the several instrumentations present in Polifab facility, a comprehensive characterisation was performed thinking to the possibility of realising an integrable tool in SARPES experiments.

The chapter is organised as follows: in section 6.1 the design of the heterostructures and the deposition process employed to grow free-standing films testing two different techniques are presented, in section 6.2 a statistical analysis on several samples is presented in order to quantitatively estimate the mechanical reliability of such ultra-thin suspended devices, the mechanical and magnetic characterisations are presented in sections 6.3 and 6.4, respectively, and finally, in section 6.5 the determination of transmission and spin filtering properties is discussed. Section 6.6 draws the conclusions of this work.

6.1 Growth of free-standing magnetic films

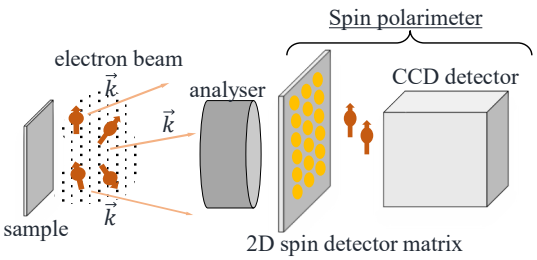

Figure 6.2: *Diagram of a spin polarimetry set-up. The electrons are extracted from the sample, they pass through the analyser, then they impinge onto 2D spin detector and finally they are counted by a CCD detector.*

The natural integration for such a device is in a spin polarimetry apparatus (see diagram in figure 6.2). What is needed is a heterostructure which allows a reasonable electron transmission which is different for spin up and spin down channels. By the well-known Lambert-Beer law, it is possible to write the probability to observe an electron traveling through a material of thickness t as:

$$T(t, E) = \exp\left(-\frac{t}{\lambda_{\mathrm{IMFP}}(E)}\right), \quad (6.1)$$

where λ_{IMFP} is the electron inelastic mean free path defined in eq. 4.3. Hence, to have a reasonable and detectable transmission, an overall thickness which does not exceed 10 nm was chosen for the heterostructure. For example, using eq. 6.1, with $t = 10$ nm, for energies of 2, 5 and 10 eV, the calculated transmission results 75.6%, 18.1% and 0.190%, respectively.

6.1.1 Design of the heterostructure and choice of the materials

The device is conceived with four general building blocks:

(i) a first layer which must guarantee a *robust mechanical support* for further layer growth and to avoid cracks and corrugations;

(ii) a *buffer layer* which is selected to allow the growth of a suitable magnetic layer on top, which sharp and flat interfaces are typically required for;

(iii) the *active magnetic material* (or stack) with magnetic anisotropy which gives an easy axis, in remanence and at room tempertaure, either in-plane (IP) or out-of-plane (OOP);

(iv) a *capping layer* to prevent the whole heterostructure from oxidation and contamination upon air exposure.

For layer (i), graphene was chosen. With respect to the similar proposal of Övergaard *et al.* of ref. [38], this choice dramatically simplifies the fabrication of the device. Indeed, the deep reactive ion etching processes on a silicon-on-insulator (SOI) substrate required in that work to reach the suspended conditions make the fabrication process very complex and composed by several steps with respect to the graphene flakes deposition, which is nowadays optimised also for industrial processes. In particular, this work takes advantage from commercial TEM grids produced by TED Pella, Inc., which provide free standing graphene membranes with different thicknesses. They are constituted by graphene sheets deposited on a copper grid of circular holes which have a diameter of 6.5 µm and a centre-to-centre distance of 12.5 µm. The grid total area is 1×2 mm (see figure 6.3(a)) while the whole sample has a circular shape with a diameter of 3 mm. Graphene is well-known to be very mechanically robust up to the monolayer (ML) limit [148]. Two set of samples were analysed, one with thickness of exactly 2 ML and the one with 7 ± 1 ML (from now indicated as 6-8 ML). Considering an interlayer spacing of $d = 0.335$ nm for graphite [148], they correspond to a thickness of ~ 0.6 nm and $\sim 1.8 - 2.4$ nm, respectively.

For layer (ii), a metallic layer which acts as seed layer for the magnetic one was chosen. In particular, the choice went to Ta, Ru or Au, also according to the deposition technique exploited. About $2 - 3$ nm are sufficient to this aim.

Layer (iii) was designed according to the desired magnetic anisotropy, in order to have a remanent magnetisation which could be IP or OOP and a sufficiently large coercive field. Co with a thickness of ~ 3 nm was chosen for the IP case, while the heterostructure composed by Ta(3)CoFeB(1)MgO(2) (thicknesses in nm)[1] was exploited for the OOP configuration. This template is a very well known multilayer with perpendicular magnetic anisotropy (PMA) [149], also very much exploited in magnetic tunneling junctions [150].

Finally, layer (iv) just prevents the magnetic (multi)layer to be oxidised. Ta, Ru or Au were chosen, with a thickness of ~ 2 nm, as for layer (ii). The general design of the device is sketched in figure 6.3(b).

6.1.2 Deposition parameters

As mentioned before, two deposition techniques were exploited and compared: MBE and magnetron sputtering. The IP heterostructures were prepared both by MBE and magnetron sputtering, while the OOP one was deposited only by magnetron sputtering.

MBE growths were performed in a UHV chamber (pressure $< 1 \times 10^{-9}$ mbar). The deposition process was performed at room temperature (RT) without any pre-treatment on the graphene substrate. The rate for Co was 0.17 nm/min (checked by a quartz microbalance). As buffer and capping layers Au was used, deposited at RT as well at a deposition rate of 0.20 nm/min (see section 4.1.1 for details about the technique).

Magnetron sputtering depositions were performed at RT too. For the IP configuration, Co was grown in DC mode with a base chamber pressure of $\sim 7 \times 10^{-9}$ mbar and an Ar partial pressure during operations of 7×10^{-3} mbar. The deposition rate (checked by a quartz microbalance) was 2.0 nm/min. As buffer and capping layers Ru was used, grown in DC mode as well and at RT. The deposition rate was 1.0 nm/min. For the OOP

[1] Here Ta acts as layer (ii). The presence of such a heavy metal is fundamental to reach PMA.

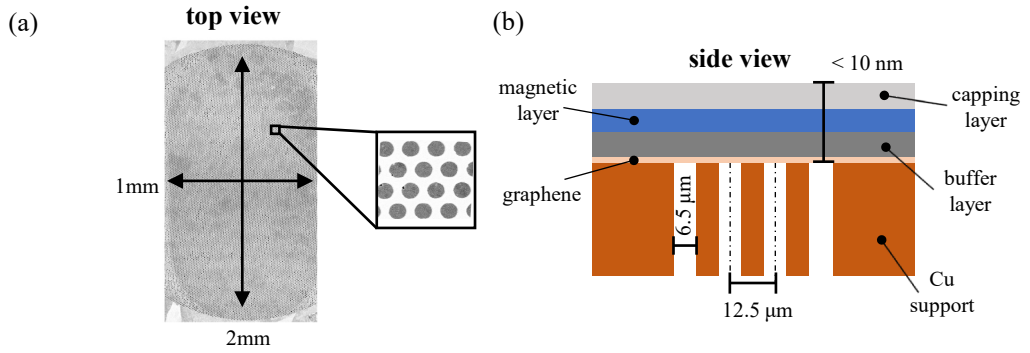

Figure 6.3: *(a) Top view of the matrix of suspended graphene membranes visualised through a scanning electron microscope. A zoom on circular graphene suspended films is shown; (b) Side view of the general scheme of the complete heterostructure which is deposited everywhere, but, since the copper support has a micrometric thickness, only the suspended regions are involved in the transmission (the scheme is not to scale).*

configuration, Ta and $Co_{0.4}Fe_{0.4}B_{0.2}$ were grown by DC sputtering, the Ar partial pressures and the deposition rates were 4×10^{-3} mbar and 4.5 nm/min for Ta, respectively, and 7×10^{-3} mbar and 1.5 nm/min for CoFeB. MgO was deposited by RF mode with Ar partial pressure of 3×10^{-3} mbar and deposition rate of 0.40 nm/min (see section 4.1.2 for details about the technique).

6.2 Mechanical reliability analysis

Even if graphene is known for its robustness, the breaking of an ultra-thin film is a possible event. For spin polarimetry applications, one needs to preserve the largest number of membranes during the whole deposition process not to compromise the measurement with pixels with an unfiltered and large signal. In fact, also if a membrane is affected by a hole which partially covers its surface, some electrons are not filtered providing a background signal to the one coming from filtered electrons which decreases the signal-to-noise ratio of the measurement.

6.2.1 Preliminary definitions and parameters of the analysis

To test the mechanical reliability scanning electron microscopy (SEM) was performed on the membranes. Three main causes are identified to contribute to the breaking of such devices. (i) Some membranes are intrinsically broken in the commercial product, due to the deposition process of the graphene itself; (ii) the samples are very small (3 mm of diameter) and hence their handling could cause fractures; (iii) the deposition process of different layers (both by MBE and magnetron sputtering) could in principle break the membrane.

In order to do a systematic study of the causes of the breaking event, a precise workflow was established in advance with two steps of SEM imaging of the samples. As depicted in figure 6.4(a), a new sample (which may report damages of type (i)) is handled for the *pre-deposition* SEM imaging (with the possibility to incur into type (ii) damages), then handled again to deposit the heterostructure and finally manipulated for the *post-*

	Deposition technique	
Graphene thickness	MBE	Magnetron sputtering
2 ML	2E	2S
6-8 ML	6E	6S

Table 6.1: *Parameters combinations, indicating the graphene thickness and the deposition technique. The number in the name of sample is the number of graphene ML (6 means 6-8 ML), while the letter indicates the deposition method (E stays for MBE (epitaxy), while S for MS (sputtering).*

deposition SEM imaging (again damages of type (ii) and type (iii)). The analysis was performed cross-checking two parameters: the number of graphene ML and the deposition technique used for the growth of the heterostructures, resulting in the four possible combinations summed up in table 6.1. To have a good statistic, data were collected from about 30 samples; about 1,700 membranes per sample were scanned for both the pre- and post-deposition SEM imaging, on average.

Before discussing the outputs of this analysis, it is necessary to state a preliminary definition of what is a *broken membrane*, to be as much rigorous as possible. When a membrane is imaged, one faces with three possible situations (reported in figure 6.4(b-d)). The film can be completely intact (panel (b)), it can report some small holes (panel (c)) or it can appear totally broken (panel (d)). Quantitatively, membrane in panel (c) reports holes for about 1.5% of the total area, while membrane in panel (d) is damaged for more than 50% of its surface and the remaining part presents back-foldings and evident corrugations. While the first one could be partially exploited, the second one is fully compromised. In the analysis which follows both membranes of panel (c) and (d) were initially considered *broken*, afterwards also the nature of the fracture was analysed.

6.2.2 Discussion

The analysis performed in the pre-deposition stage is shown in figure 6.5(a). The percentages of fully intact membranes are reported for 2 and 6-8 ML of graphene. The values are 87% $\pm$ 9.6% and 94% $\pm$ 9.0%, respectively. These data contain information about both damages of type (i) and (ii), demonstrating that the number of ML for the graphene actually matters even without any deposition process. For the post-deposition analysis the data are reported in figure 6.5(b), also in this case the difference between 2 and 6-8 ML is straightforward. The percentages are 51% $\pm$ 29% and 88% $\pm$ 17%, respectively. It is noteworthy that the average values of damages are increased by a factor of 3.7 and 3.6 for the two cases, while the standard deviation values by a factor of 3.0 and 1.9. Hence, it can be argued that samples with 2 ML, which present a very large error bar, suffer the handling procedures (damages of type (ii), which may be caused by several variables and present a more aleatory dynamics) much more than 6-8 ML samples. A difference of few monolayers of graphene affects very much mechanical reliability.

As mentioned before, at this point it is important to further investigate the nature of the fractures. Membranes which present small holes can be still processed, while completely broken membranes are not exploitable at all. To quantify this aspect the broken membranes are grouped into three cases: films which do not preserve more than a half of their surface (> 50%), membranes which report damages in the range of 20% - 50% of their surface and films which present most very small damages (< 20%). In figure 6.5(c) are

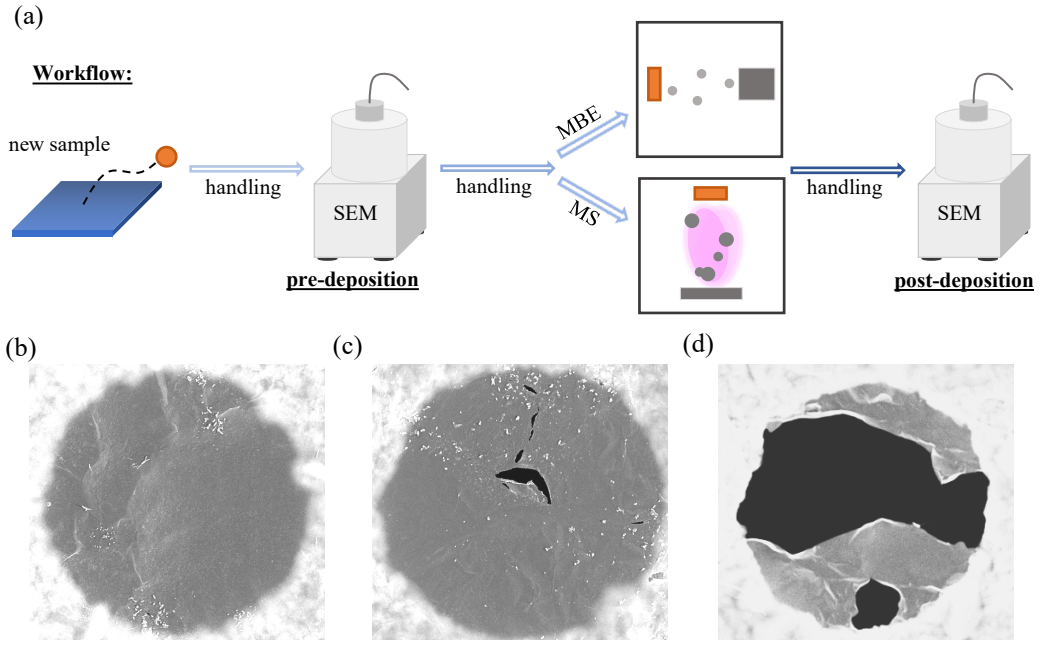

Figure 6.4: *(a) Workflow for the analysis of the mechanical reliability of free-standing membranes with two steps of SEM imaging, pre- and post-deposition; (b) Intact membrane; (c) Partially damaged membrane; (d) Completely destroyed membrane.*

presented these data. In the case of 2 ML, 33% of the broken membranes are completely destroyed, 57% partially damaged and only 10% of them present small holes. The case of 6-8 ML is different. Only 6.3% are in the category > 50%, 16% in the range 20% - 50% and 78% have just small fractures. This picture is even more drastic than the one proposed in panel (b): the number of monolayers guarantees not only a better average of intact membranes, but also the entity of the damages is reduced.

Beyond this discussion, in order to deduct the role of the deposition process a normalisation procedure was performed.[2] Data in the post-deposition imaging were normalised with respect to data of the pre-deposition imaging, defining a *survival rate* as the number of membranes preserving their integrity after the deposition process, divided by the number of membranes previously intact. The result is shown in figure 6.5(d). The four combinations of table 6.1 are plotted and the best condition (both for the average value and for the small error bar) is found to be for the samples grown by magnetron sputtering on 6-8 ML of graphene. The survival rate is 94% $\pm$ 4.0%. For what regards the comparison between the two techniques, MBE and magnetron sputtering seem to act in the opposite way for 2 ML and for 6-8 ML. The large error bar for the thinner samples makes a fair comparison impossible.

6.3 Mechanical characterisation

The SEM imaging of the membranes gives information about their condition, but it is not possible to extract any quantitative data on their robustness. For this aim, one can ex-

[2] Actually, there is also in this case an intrinsic handling passage also for this normalisation, but here it assumed to be negligible because it is substantially reduced with respect the initial one.

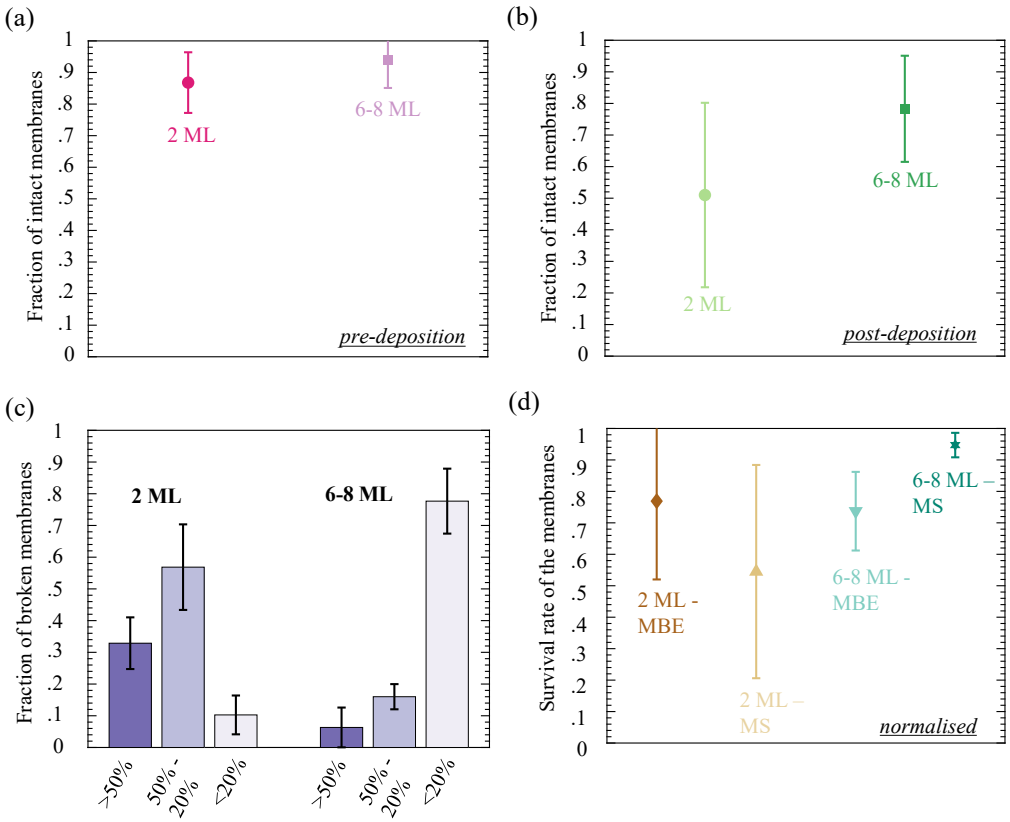

Figure 6.5: *(a-b) Pre-deposition and post-deposition statistics of the fraction of intact membranes for 2 and 6-8 ML; (c) Quantitative analysis of broken membranes for 2 and 6-8 ML showing how much their surface is affected by fractures; (d) Survival rate for the four combinations of monolayers and deposition techniques.*

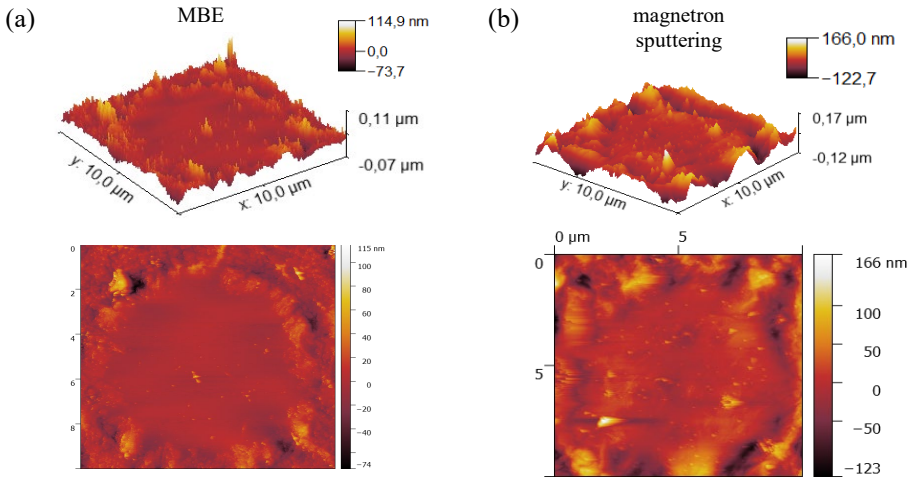

Figure 6.6: *(a) AFM topography of a membrane grown by MBE; (b) AFM topography of a membrane grown by magnetron sputtering.*

	Deposition technique	
	MBE	Magnetron sputtering
Average value	0.12 nm	0.91 nm
Standard deviation	0.16 nm	1.2 nm

Table 6.2: *Roughness parameters measured on samples 6M (Au/Co/Au) and 6S (Ru/Co/Ru) with the relative average values and standard deviations.*

ploit atomic force microscopy (AFM) to infer mechanical properties of such free-standing devices.

The role of this section is twofold: AFM was employed in two modes, firstly to measure topography of such thin films in standard tapping mode, afterwards, a force spectroscopy was performed. This second measurement consists in placing the AFM tip at the centre of the free-standing film in contact mode and, starting from a large distance where no force is sensed by the tip, the cantilever is moved close to the sample and a force is applied in order to test its mechanical resistance until the membrane breaks to retrieve the maximum load which can be applied to it. This characterisation was carried out by using a Keysight 5600LS AFM, exploiting silicon cantilevers with a tip radius of about 50 nm and an elastic constant $k = 40$ N/m.

For what concerns topography, it is useful to compare samples produced with the two different deposition techniques. Figure 6.6(a-b) shows a comparison between a 6M sample (panel (a)) and a 6S one (panel (b)). Some corrugations are revealed at the edges of the free-standing films where the membranes adhere to the sides of circular holes of the copper grid. It was noted that the free-standing layer was not perfectly stretched in the hole but presented some ripples. In spite of this observation, they do not compromise the device since the estimated tilting which they reach does not exceed $\sim$ 1.5°, with respect to the horizontal plane. The roughness was estimated as well and the results are reported in table 6.2. The process performed with MBE gave a better result in terms of roughness (0.12 nm with respect to 0.91 nm of magnetron sputtering) and guarantees a better control of the heterostructure deposition. Nevertheless, both processes are suitable for the purposes of this work, because the roughness is always smaller than the minimum layer thickness.

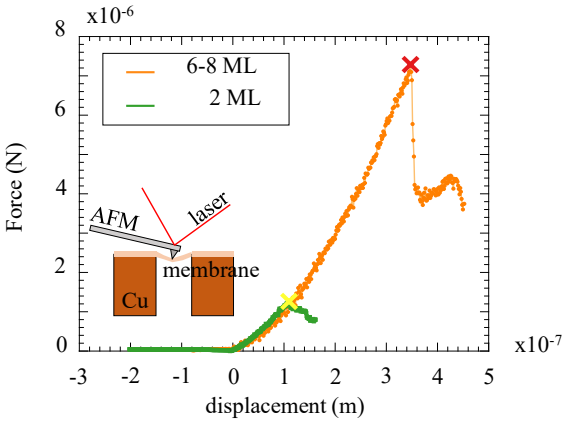

Figure 6.7: *Force versus piezoelectric displacement of the cantilever of the AFM for samples with 2 ML (green) and 6-8 ML (orange). The crosses indicate the breaking load of the membranes. The inset shows a sketch of the indentation process of the AFM tip.*

Then, the tip was positioned in the centre of the hole to perform the mechanical test in contact mode and at a constant displacement rate (the experiment is sketched in the inset of figure 6.7). Firstly, low-load measurements were done for each membrane. No hysteretical behaviour was observed, confirming that the measurements were carried out

in the elastic regime. The data collected were highly repeatable in time and every measurement was calibrated with a reference sample of Cu to infer the sensitivity of the AFM to retrieve the precise value of the force. Finally, the measurement was performed once again, but this time with the aim of deliberately provoking the fracture of the membrane. This allowed to estimate the breaking load of the device. The results are reported in figure 6.7 for samples with different number of ML (2 and 6-8), as a function of the displacement[3]. Breaking loads ($F_{\max}$) were defined as the force at which the AFM signal presents a drastic drop, meaning that the membrane is no more making any mechanical resistance. In the figure, they are marked with crosses. The curves presented the same functional form for both the samples, but a different maximum load. For sample with 2 ML it resulted $F_{\max} = 1262\,\text{nN}$, while for sample with 6-8 ML $F_{\max} = 7287\,\text{nN}$ was achieved. As expected, the thicker sample is definitely more robust. As a comparison, ref. [148] reports the value of $F_{\max} = 1770\,\text{nN}$ for 1 ML of graphene (the AFM tip of the cited reference has a radius of 16.5 nm, while the diameter of the membrane is 1.5 µm, so even if the membrane is smaller and thinner, the radius tip is less than a half with respect to the one used in this work, so that the overall pressure applied by the tip decreases, giving a higher load). This measurement confirms the good choice of graphene as a first layer, giving a high robustness to the whole system. [4]

6.4 Magnetic characterisation

For spin polarimetry applications, two properties are needed from the magnetic point of view: sufficiently high coercive field and magnetic remanence. The first one allows stability of the magnetisation vector from external perturbations during the measurements, the second one to avoid multi-domains configurations whose orientations can decrease the net spin filtering efficiency of the membranes. As written before, IP and OOP anisotropies were achieved.

The same IP (Co-based) and OOP (CoFeB-based) heterostructures were preliminarily deposited on a rigid substrate of silicon with 1 µm of thermal SiO_2 on the surface in order to check, by means of vibrating sample magnetometry (VSM), the presence of easy/hard axes along the selected directions. Co revealed IP easy axis, while Ta/CoFeB/MgO presented perpendicular magnetic anisotropy (PMA), as expected. The results are shown for comparison in figure 6.8(a-b) with solid lines.

The measurements on the suspended substrate were performed with the optical setup described in section 4.5. Exploiting Faraday effect, instead of VSM (as for the rigid substrate), only the suspended part of the film are probed, partially transparent to light. The Cu support is thick enough to prevent light to be transmitted. As explained in section

[3] In the displacement are considered both the indentation of the membrane and the elastic deformation of the cantilever. In order to estimate the maximum load which the membrane can suffer this distinction does not matter. Instead, if one wants to estimate the mechanical properties of the membrane itself, e.g., the Young modulus, this distinction is necessary (see also note [4]).

[4] Lee *et al.* in ref. [148] model their system treating the free-standing device as a clamped circular membrane, stating the following assumptions: (i) the material is supposed to have isotropic mechanical properties; (ii) the membrane is supposed to be two-dimensional (the aspect ratio between its diameter and the thickness is negligible). The first one is motivated by the sixfold rotation symmetry of graphene sheets. Within this model, the force-displacement curve can be approximated as: $F = \sigma^0_{2\text{D}}(\pi a)\,(\delta/a) + E_{2\text{D}}(q^3 a)\,(\delta/a)^3$, where F is the applied force, δ is the indentation of the tip, a is the membrane diameter, $\sigma^0_{2\text{D}}$ is the pre-tension in the film, $E_{2\text{D}}$ is the Young modulus for the two-dimensional sheet and q is defined by the equation $q := 1/(1.05 - 0.15\nu - 0.16\nu^2) = 1.02$, with the Poisson ratio $\nu = 0.165$ taken from ref. [151]. The model can be nicely applied for the 2D system but it fails in fitting the curves shown in this work so, in this case it is not possible to obtain the exact value of the Young modulus (even after taking into account the subtlety evoked in note [3]). An *ad hoc* model should be developed, but it goes beyond the scope of this thesis, where the data on the load is sufficient to justify the choice of materials.

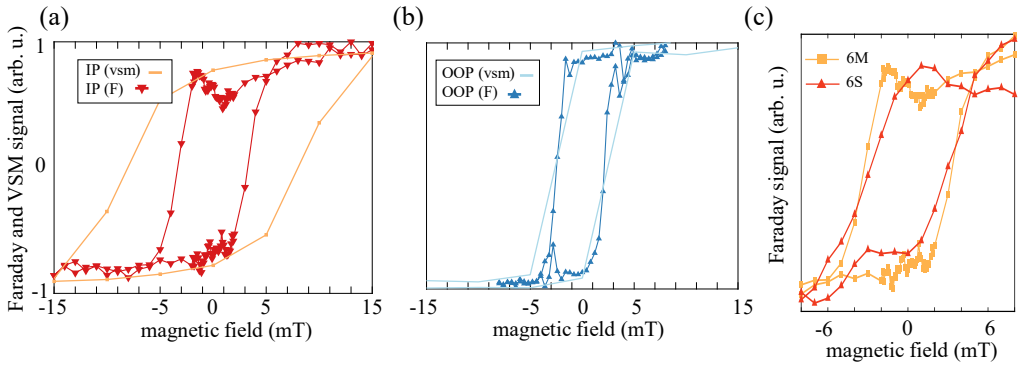

Figure 6.8: *(a-b) Faraday effect measurement of the IP (OOP) heterostructure based on Co. With solid lines the comparison with the structure deposited on the rigid substrate is shown; (c) Comparison between different samples for the IP configuration with different capping layers (Ru for 6S and Au for 6M).*

4.5, for the OOP configuration the sample was placed between the coils at $\theta = 0°$, while for the IP configuration – in order to have a projection of the magnetisation along the light path – the sample was tilted by an angle of $\theta \simeq 17°$. Hence, the magnetic moment probed through Faraday effect is proportional not to $|\mathrm{M}|$ but to $|\mathrm{M}|sin\theta$, which represents the $\sim$ 29% of the actual value.

In figure 6.8(a-b), the results for the IP (Au/Co/Au) and OOP (Ta/CoFeB/MgO) configurations are reported. A hysteresis loop is present in both the cases. The coercive field is 3.3 ± 0.070 mT and the normalised saturation remanence is 0.66 for the IP sample (panel (a)), while for the OOP structure the coercive field is 2.3 ± 0.24 mT and the normalised saturation remanence is 0.84 (panel (b)). For the IP case, the coercive field decreases of ~ 2 mT with respect to the structure deposited on the rigid substrate. This is not the case for the OOP samples. Nevertheless, the coercive fields are sufficiently high to guarantee the magnets not to be perturbed in spin polarimetry set-ups, which are typically already magnetic field-free in order to avoid any deflection in the electrons trajectories (as a comparison, it is noteworthy citing the case of VLEED detectors based on Fe(001)-p(1×1)O targets, which presents coercive fields of just ~ 0.1 mT [129]).

Also an investigation on the role of the buffer and capping layer, was performed for what concerns the IP configuration. In particular, samples 6M and 6S were measured. The comparison is shown in figure 6.8(c). The main features are maintained. Due to sharper interfaces, achieved with MBE (see former section about roughness and topography), 6M sample gives a more squared loop and it may be preferred with respect to sample 6S, even though it preserves comparable coercive fields and remanence state too. The coercive field is around 3 mT for both the samples. For what regards sample with 2 ML, they suffer of a reduced signal-to-noise ratio and to an overall smaller Faraday signal. As highlighted in section 6.2, the presence of a larger number of broken membranes affects this measurement.

6.5 Transmission and spin-filtering characterisation

6.5.1 Experiment design and definition of the set-up

Electron transmission measurements were performed exploiting the set-up exposed in details in section 4.6. The operations described below were done completely *in situ*. The characterisation was performed in order to test the feasibility of using such a device for spin filtering operations. In this sense, the following step-by-step protocol was designed in order to test the response of the magnetic layer, neglecting the effect of the buffer and the capping layer:[5]

(o) SEM characterisation of the device. The sample is imaged to count how many membranes are initially broken.

(i) Measurement of bare 6-8 graphene ML. This preliminary measurement makes possible to retrieve the energy- and thickness-dependent electron transmission from few nanometers material;

(ii) Measurement of 1.5 nm of Co. A first layer of cobalt is deposited *in situ* by MBE and a first measurement of the membrane transmission with unpolarised and polarised electron beam is performed. It allows to add another point to the thickness dependence of transmission;

(iii) Measurement of $1.5 + 2.0$ nm of Co. 2 nm of Co were added to the stack in order to perform other transmission measurements to increase the number of points of the transmission curve and to check whether the filtering properties were modified by the presence of a thicker ferromagnet;

(iv) SEM characterisation of the device. This was performed *ex situ* to test the final percentage of intact membranes.

Before steps (ii) and (iii) the device was magnetised *in situ* with a magnetic field of about ± 10 mT, definitely larger than the coercive field of 3 mT, reported before. The detection system is sketched in figure 6.9. The spin polarised electron beam is emitted from the photocathode (PC) with a certain current, defined as I_{PC}. As illustrated in section 4.6, electrons are guided by an electron gun which consists in a system of lenses with a certain energy-dependent transmission $T_{\mathrm{gun}}(E)$ [135]. Hence, the current immediately after the gun is $I_0 = I_{\mathrm{PC}} \cdot T_{\mathrm{gun}}(E)$. The beam impinges on the sample, composed by the membranes matrix, and it

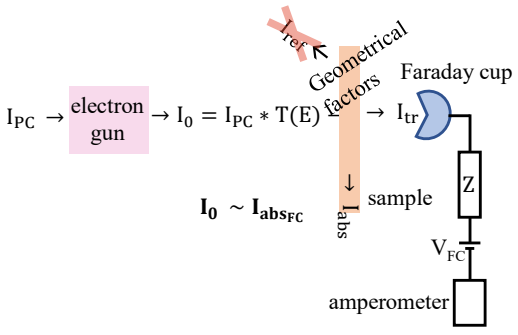

Figure 6.9: *Sketch of the experimental set-up and on the defined quantities in the text.*

[5]Here this step-by-step experiment is presented. Actually, the measurements were performed also in other configurations with samples grown with the heterostructure entirely deposited in one step and measured *in situ* and with samples where the heterostructure was exposed to air and so measured *ex situ*. The protocol presented in this section is the most reliable and sistematic one, hence it is preferred to other measurements performed.

generates an absorbed (I_{abs}), a transmitted (I_{tr}) and a reflected (I_{refl}) current. Due to the polycrystalline nature of the sample it is possible to assume that the reflected current is negligible [34]. The energy of electrons of the beam can be swept in the range $2-25$ eV. I_{abs} is in the order of few µA and can be easily detected. In order to attract and collect the transmitted electrons, a Faraday cup (FC) at $V_{\mathrm{FC}} \sim 30$ V is placed behind the sample. The detection is performed by means of an amperometer measuring the current over a very large impedance $Z \simeq 150\,\mathrm{G}\Omega$, to avoid spurious flow of the current due to V_{FC}. Every point in energy is averaged from 20 consecutive measurements.

6.5.2 Discussion of transmission measurements

Spin-integrated current signals, normalised to the maximum, are shown in figure 6.10, in order to better display the shape of the four measurements. The four lines plotted are respectively: the absorbed current from the FC without the sample (purple) and the transmitted current after steps (i) (green), (ii) (red) and (iii) (orange), defined above. All three steps do not seem to give any contribution to the transmitted current below ~ 10 V. Then, while step (i) presents the expected exponential decrease, steps (ii) and (iii) actually show an increasing behaviour which saturates for high energies.

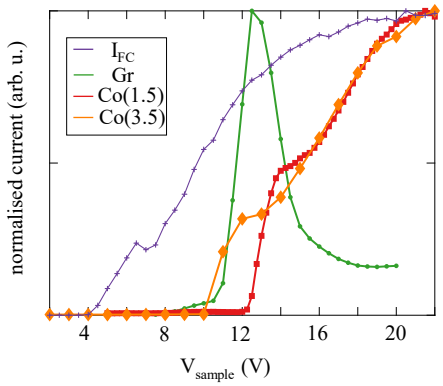

Figure 6.10: *Transmission for the reference current I_0 and for steps (i), (ii) and (iii).*

Apart from bare graphene data, the measurements gave an unexpected result. To shed light on the mechanism observed, it is possible to model the transmission of the system in order to disentangle the attenuation contributions of the device itself and the ones caused by intrinsic nature of the set-up.

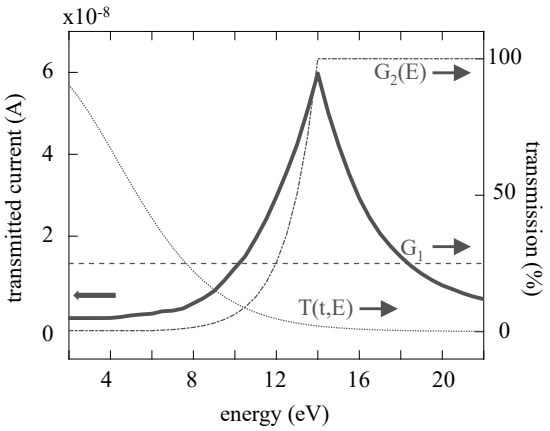

Figure 6.11: *Transmission parameters of eq. 6.2.*

First of all, one can assume that the current which leaves the electron gun is equal to the absorbed current by the FC, measured without any sample placed. This means that $I_{\mathbf{abs,FC}} \simeq I_0(E) := I_{\mathrm{PC}} \cdot T_{\mathrm{gun}}(E)$ (the notation refers to figure 6.9). In this way, it possible to write the following phenomenological expression for the current transmitted by the membranes:

$$I_{\mathrm{tr}} = I_0 \cdot (G_1 \cdot G_2(E)) \cdot T(t,E). \quad (6.2)$$

The variables in eq. 6.2 are defined as follows. $G_{1,2}$ are the intrinsic *geometrical factors*. The first one is due to the active area of the device (i.e., the ratio between the overall area of the membranes and the total area which includes the copper support)

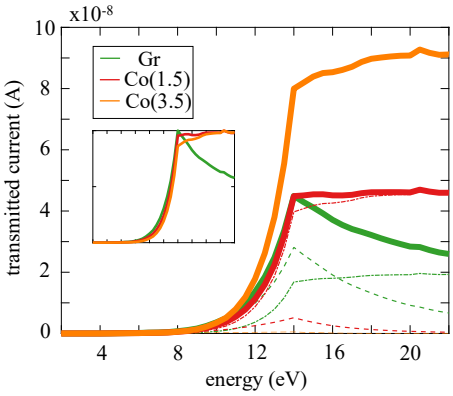

Figure 6.12: *Calculations using equation 6.2 showing transmitted currents for the two contributions (dotted lines for the N_{h} contribution and dashed lines for the $(1-N_{\mathrm{h}})$ one) and their sum (solid lines) for steps (i), (ii) and (iii). In the inset the same curves are shown normalised to the maximum to have a more straightforward comparison between the experimental data reported in figure 6.10.*

and which gives $G_1 = 25\%$. The second one is generated by the energy-dependent diameter of the electron beam ($G_2(E) := A_{\mathrm{membranes}}/A_{\mathrm{beam}}(E)$), $A_{\mathrm{beam}}(E)$ was measured as indicated in ref. [135]. $T(t,E)$ is the transmission of the free-standing films defined in equation 6.1, which is function of thickness of the membrane and of the energy. All this term and the calculated I_{tr} with I_0 as input are plotted in figure 6.11.

It is clear from figure 6.11 that this model cannot account for the experimental observation of steps (ii) and (iii). In order to improve the model, it is possible to introduce the possibility that some membrane are broken. If N_{h} is defined as the percentage of broken membranes, eq. 6.2 can be modified adding the contribution of the electrons which do not suffer any attenuation. The following equation results:

$$I_{\mathrm{tr}}^{'} = I_0 \cdot (G_1 \cdot G_2(E)) \left[(1-N_{\mathrm{h}}) \cdot T(t,E) + N_{\mathrm{h}}\right]. \tag{6.3}$$

Hence, exploiting eq. 6.3 and using the parameters of the electron gun, the measured I_0 and N_{h} from the experiments of section 6.2 as inputs,[6] the expected behaviour of the curves was simulated. The results of these simulations, for steps (i), (ii) and (iii) are presented in figure 6.12 (the inset shows the three curves normalised to the maximum to have a comparison with the measurements of figure 6.10). It is clearly visible that if the decreasing behaviour is shown by graphene only, the broken membranes are strictly dominated by broken membranes, which causes the paradoxical increased currents from step (ii) to step (iii). The observed data well explained the results experimentally found (a part from a relative shift which can be due to sample charging during the measurement).

6.5.3 Spin filtering characterisation

For what regards the spin resolution, the region of interest is the one at low energy ($\sim 3-9$ eV) where it is well-known that cobalt reveals a maximum asymmetry of $\sim 7\%$ [132]. Of course, only the first term in equation 6.3 (the one accounting for intact membranes) contributes to the asymmetric transmission of spin polarised electrons. From figures 6.10

[6] Since it is not possible to do step-by-step *in situ* SEM imaging of the devices, it is hard to have a precise estimation of N_{h} in the intermediate steps. It is possible to rely on average values which were provided in the former part of the chapter.

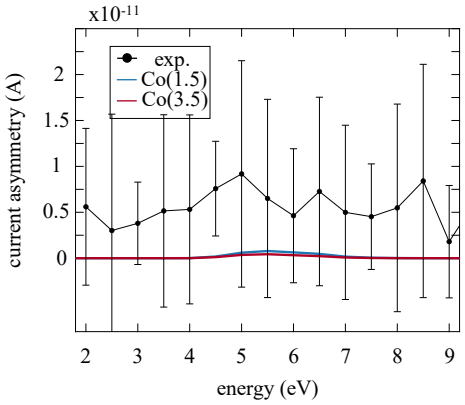

Figure 6.13: *Calculations for the spin asymmetry for step (ii) and (iii) in solid blue and red lines. In black the experimental measurement of the spin asymmetry.*

and 6.12, it is evident that in this region of interest the experimental results suffer of a more severe attenuation. The spin asymmetry between spin up and spin down channels was calculated starting from equation 6.3 and adding the asymmetry parameter taken from ref. [132] (see chapter 3 for more details). In figure 6.13 it is shown the comparison between the calculated asymmetry for cobalt film (blue and red solid lines) (taking into account the polarisation of the electrons coming out from the gun to be 0.25 (see section 4.6)) and the experimental measurement. The expected result stays in the errorbar of the measurement. So it is not possible to infer spin filtering properties from the present data.

Further investigations should move in two possible directions: firstly try to fabricate membranes on larger samples in order to increase the total area of the device to minimising effects from geometrical factor $G_2(E)$ (still maintaining the ones from G_1), otherwise a different configuration of the electrostatic lenses is needed in order to have more focused electrons where a larger fraction of the beam impinges on the sample. The model explained before allows to estimate a reasonable beam diameter in order to obtain a curve which would not be hidden by the error bar. In fact, a signal of $\sim 50\,\text{pA}$ can be obtained with a diameter of $\sim 4\,\text{mm}$, while the actual value for the set-up was $\sim 2\,\text{cm}$. This second option is under investigation and the results are still work in progress.

From the applicative perspective, data on single macroscopic membranes present in literature [40, 132] guarantee already sufficiently high asymmetry for this kind of configuration. Moreover, even if the broken membranes seems to cause a huge background, it is worth noticing that in a SARPES set-up the CCD detector would allow a pixel-by-pixel detection and hence the possibility to monitor in real time the appearance of broken films and eventually avoid to measure some points, which is not an option with a wide detector such as the Faraday cup used in the present set-up.

6.6 Conclusions

This chapter provided the design of a prototype 2D spin detector. The intent was to simplify the complex fabrication process proposed in ref. [38], exploiting the resources offered by ultra-thin graphene membranes and taking advantage from the selective transmission of electrons through a ferromagnetic layer deposited on them. The mechanical

reliability was tested over a large set of samples, with different deposition techniques and different number of graphene monolayers, resulting in a much larger reliability for 6-8 ML and with a survival rate which reach 94% in the case of magnetron sputtering deposition technique. The free-standing membranes were also characterised from the mechanical and the magnetic point of view, revealing a large maximum load (up to $\sim 7300\,\text{nN}$) for samples with 6-8 ML of graphene, a roughness always smaller than 1 nm and suitable magnetic properties with anisotropy IP (Au/Co/Au heterostructure) and OOP (Ta/CoFeB/MgO/Ta heterostructure) which basically mimic the ones on rigid substrates with coercive fields of $\sim 3\,\text{mT}$ and a sufficiently large remanence magnetisation (66% for IP samples and 84% for OOP ones).

The transmission was measured for such devices, showing the expected behaviour for samples with a small number of broken membranes. When the number of holes becomes larger, the predominant signal observed was due to unfiltered electrons. For what regards the spin asymmetry, the implementation of a more efficient focus system for the electron beam was proposed in order to make the signal detectable. Relying on previous works (on different systems), it is possible to claim that the reported spin asymmetry is sufficiently high to be employed in this new conception of spin detection.

From an industrial perspective, this chapter pushed the so-called technology readiness level (TRL) from 1 to 3.[7] The possibility to validate it in a real SARPES set-up could make it suitable in commercial set-ups such as those proposed by Specs or Scienta, thus envisaging a real market application.

[7] TRL is a methodology proposed by NASA to evaluate the readiness of a technology under development, the scale goes from 1 to 9, where 1 stands for the observation of the basic principles and 9 stands for a system which was tested in an operational environment. 3 means that the experimental proof-of-concept was provided and it is ready for a first validation

CHAPTER 7

Transport properties of GeTe films and heterostructures

7.1 Introduction

In this chapter the magnetoelectric transport properties of GeTe, the father compound of FERSC class, are investigated. As discussed in chapter 2, a lot of experimental work was performed in order to characterise both the ferroelectricity and the electronic bands nature of this material [1, 22]. Here the spin functionalities are studied from the standpoint of transport, by means of characterising its magnetoresistive properties.

If the previous two chapters were devoted mainly to spectroscopy both from the point of view of complex band structure measurements of new materials (Ge-doped SnTe, in chapter 5) and from the technical point of view, developing a 2D spin detector (chapter 6), this chapter faces again with bulk Rashba bands, but considering their direct consequences on magneto-transport. It is demonstrated how FERSC can reveal their non trivial nature also considering them in a different perspective.

As reviewed in chapter 2 in section 2.3.3, Rashba systems and topological insulators are characterised by a second order response magnetoresistive effect named bilinear magnetoelectric resistance (BMER)[1]. This manifestation of non-reciprocal charge tranport represents a new paradigm of unidirectional magnetoresistance avoiding the presence of ferromagnetic layers (contrary to the case of [152]), resulting in the following relation:

$$R(\mathbf{j}, \mathbf{B}) = -R(-\mathbf{j}, \mathbf{B}) = -R(\mathbf{j}, -\mathbf{B}). \tag{7.1}$$

As demonstrated in ref. [87], materials displaying this effect are interesting not only because they show two levels of resistance for opposite configurations of external magnetic

[1] Since the discovery of this effect is very recent, in literature there is not a unique name to refer to it. It is sometimes called unidirectional magnetoresistance (UMR) in analogy to a phenomenologically similar effect in NM/FM bilayers [152], in other cases BMER [87, 90, 153] and in other cases just bilinear magnetoresistance (BMR) [89, 93].

field [89, 91], but also because this effect could be a probe of the spin texture of such materials [90]. In 2021, BMER was also detected in GeTe and reported in ref. [94], but the complex bulk Rashba spin texture was treated as a simple two-dimensional electron gas with no hints about the hexagonal warping characterising the GeTe Hamiltonian (see eq. 2.17).

The presence of spin Hall effect in GeTe, demonstrated in ref. [1], with a spin Hall angle comparable to the one of a reference material such as Pt, makes this material interesting for spin-orbit torque devices (see chapter 2 for details). For this purpose, during this Ph.D. activity also GeTe/CoFe Hall bars were fabricated in order to detect the second order response of the resistance directly related to magnetisation oscillations and so to spin-orbit torque. The research in this topic is still ongoing and the preliminary results are not shown in this thesis.

All transport experiments were carried out at the Magnetism and Interfaces laboratory of the Department of Materials at ETH Zürich under the supervision of Dr. Paul Noël. The patterning of the devices was performed by Federico Fagiani (Ph.D. student).

The chapter is organised as follows: in section 7.2 the preparation of the sample and the design of the devices for such experiments are described; in section 7.3 the magnetoelecric measurements on GeTe films are presented, taking advantage from symmetry considerations, field and current dependences, it is possible to disentangle spurious effects, showing the presence of a second order effect which is ascribed to bilinear magnetoelectic resistance. Finally, conclusions and perspectives of this work are drawn in section 7.4.

7.2 Samples preparation

As discussed in chapters 2 and 5, GeTe can be epitaxially grown on Si(111). In order to detect BMER it was used a layer of 15 nm of GeTe which was covered *in situ* by a protective layer of $10 - 12$ nm of Si_3N_4 to prevent its oxidation.

Then, samples were patterned with a Hall bar geometry (it is shown in figure 7.1(a)) by means of optical lithography (for details on the technique and on the recipe see section 4.2). The channel of the Hall bar was equipped with three Hall branches with an overall channel length of $50 + 50$ µm, a width of 10 µm and a width of the voltage pickup lines of 3 µm [154]. The aspect ratio Z of the whole channel is $Z = 10$. For the case of GeTe films, the samples were patterned along different crystalline directions, in particular, at 0° and 30°. According to the crystal structure, the Hall bars at 0° are aligned along the ZU direction while the ones at 30° along the ZA direction.

For the measurements presented in the following, harmonic Hall detection is the experimental technique employed. All the experiments presented were performed in the dark to suppress any photo-induced effect in the GeTe layer[2] and at room temperature. Details about the set-up are explained in section 4.4.

7.3 Magnetoresistance of GeTe monolayers

7.3.1 Measurements

Firstly, the magnetoelectric properties were studied measuring the first harmonic component of the longitudinal resistance ($R_{\omega,\mathrm{L}}$). The resistivity of GeTe was probed to be

[2] GeTe is a narrow-gap semiconductor with $\epsilon_{\mathrm{gap}} = 0.6$ eV, see chapter 2.

$\rho = 384 \times 10^{-6}$ Ωcm. As depicted in figure 7.1(a), the magnetoresistance (MR) experiments were performed rotating the device immersed in a static magnetic field of 1.2 T in xy, xz and yz directions (see figure 7.1(b) for the angles definition), while injecting an AC current density along the $+x$ direction of 3.3×10^5 A/cm^2 with a frequency $f = 10$ Hz. The angular dependence of $R_{\omega,\mathrm{L}}$ is shown in figure 7.1(c). The solid lines represent fits of experimental data using sine functions. While the out-of-plane scans xz (blue) and yz (green) show the expected Lorentz MR (maximum along $\pm z$), the in-plane scan xy (red) exhibits a MR signal with maxima (minima) for $\mathbf{B} \parallel \pm\mathbf{y}$, i.e., $\varphi = \pi/2 \pm n\pi$ ($\mathbf{B} \parallel \pm\mathbf{x}$, i.e., $\varphi = \pm n\pi$). This signal does not change sign upon the inversion of the external magnetic field direction and resembles the anisotropic MR of magnetic systems. Accordingly to ref. [89], it is named as quadratic MR (QMR) and it was firstly reported for topological insulators by Taskin *et al.* in ref. [155]. Keeping the same current density the field was swept between 0 and 1.4 T. The field dependence of this signal is reported in figure 7.1(d). Black squares quantify the percentage value of QMR for every magnetic field used, according to the expression $\mathrm{QMR} = \Delta R_{xy}/R_0[\%]$, where ΔR_{xy} represent the difference between the resistance when the field is applied along x and along y ($\phi = \pm n\pi$ and $\phi = \pi/2 \pm n\pi$, respectively), while R_0 is the resistance at zero field. The solid black line represent a parabolic fit, which accounts for the expected behaviour of such an effect [89, 91].

Then, the second order response of the longitudinal and transverse (Hall) resistance ($R_{2\omega,\mathrm{L}}$ and $R_{2\omega,\mathrm{H}}$) was measured with the geometry of figure 7.1(a). As anticipated in the introduction, the intent is to observe a unidirectional behaviour which can be explained with BMER physics. This means that the procedure consists in identifying all the other spurious contributions (thermal) which must be subtracted from the signal. Their angular dependences are reported in figure 7.2 for the xy, xz and yz planes in panels (a), (b) and (c), respectively. The measurements were performed in a static magnetic field of 1.2 T and with a current density of 3.3×10^5 A/cm^2. The solid black lines are sinusoidal fits of experimental data.

It is possible to observe that $R_{2\omega,\mathrm{L}}$ displays a unidirectional behaviour for xy and yz scan: the longitudinal signal is maximum (minimum) when $\mathbf{B} \parallel +(-)\mathbf{y}$ ($\varphi = +(-)\pi/2$). This behaviour could be ascribed to BMER. Also the Hall response ($R_{2\omega,\mathrm{H}}$) shows a unidirectional behaviour for the xy and xz scans with a maximum (minimum) when $\mathbf{B} \parallel +(-)\mathbf{x}$ ($\varphi = 0(\pi)$), which can be fitted with a cosine and sine function, respectively. This angular dependence of $R_{2\omega,\mathrm{H}}$ is the signature of ordinary Nernst effect (ONE).

It is possible to write the following phenomenological expressions which account for the unidirectional behaviour observed for longitudinal and transverse second harmonic responses:

$$\begin{cases} R_{2\omega,\mathrm{L}} = R^{\max}_{2\omega,\mathrm{L}} \sin(\varphi)\sin(\theta); \\ R_{2\omega,\mathrm{H}} = R^{\max}_{2\omega,\mathrm{H}} \cos(\varphi)\sin(\theta). \end{cases} \tag{7.2}$$

Following the angular dependences calculated in appendix A, it is possible to notice that the symmetries of these two contributions (of the Hall response in xy and xz scans) trace the one of ordinary Nernst effect (ONE) induced by a temperature gradient along the z direction. The presence of such thermal effects is confirmed also looking at the longitudinal signal in xz scan, which presents a π-periodic angular dependence, typical of planar Nernst effect (PNE) with the same temperature gradient direction.

It is important to notice that in the longitudinal resistance BMER and ONE share the

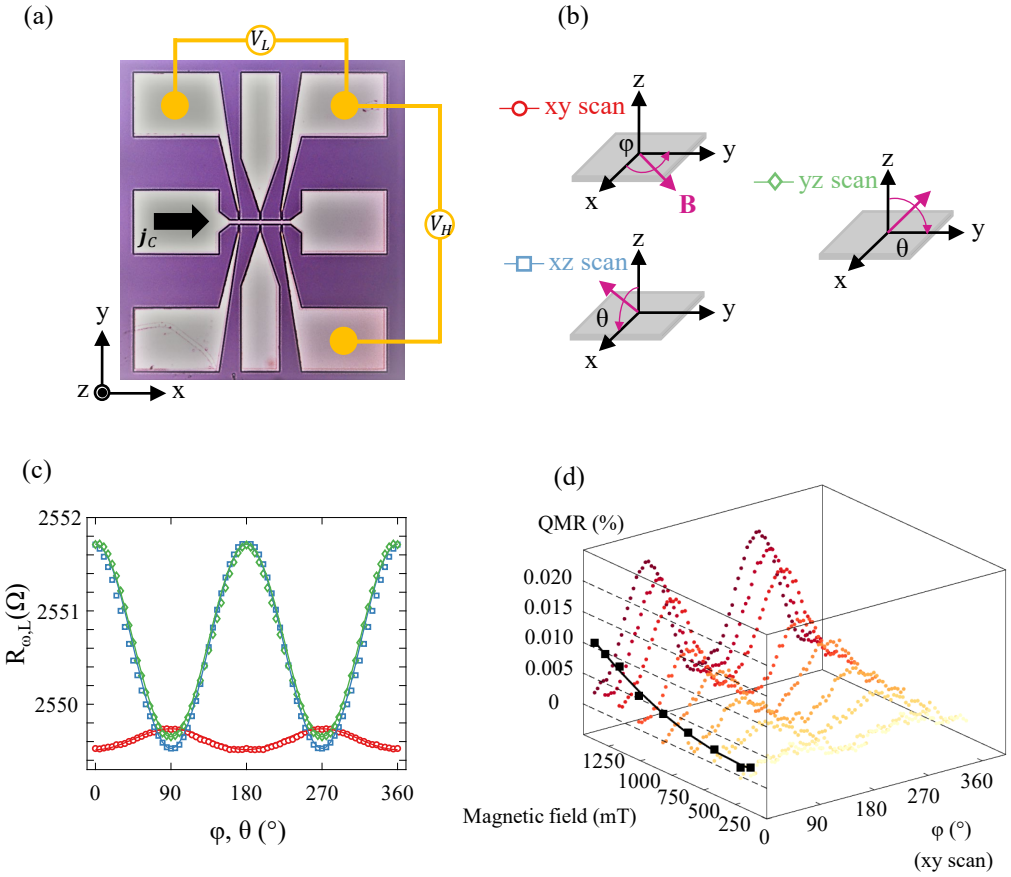

Figure 7.1: *(a) Patterned device and coordinate system.* $\mathbf{j}_C$ *is the injected current density and* V_L *is the measured longitudinal voltage, while* V_H *is the transverse Hall voltage; (b) Geometry of the angle scans.* φ *is the in-plane angle and* θ *is the out-of-plane one. The current is always injected along* $+x$*; (c) First harmonic longitudinal resistance for the three angle scans. The measurements were performed at a constant external magnetic field* $B_{ext} \simeq 1.2\,\mathrm{T}$*, while the current density injected was* $j_C = 3.3 \times 10^5\ \mathrm{A/cm^2}$*. The solid line are fits of experimental data; (d) Field and angular dependences of the QMR signal. Black data represent the QMR value for every curve, while the solid line is a parabolic fit.*

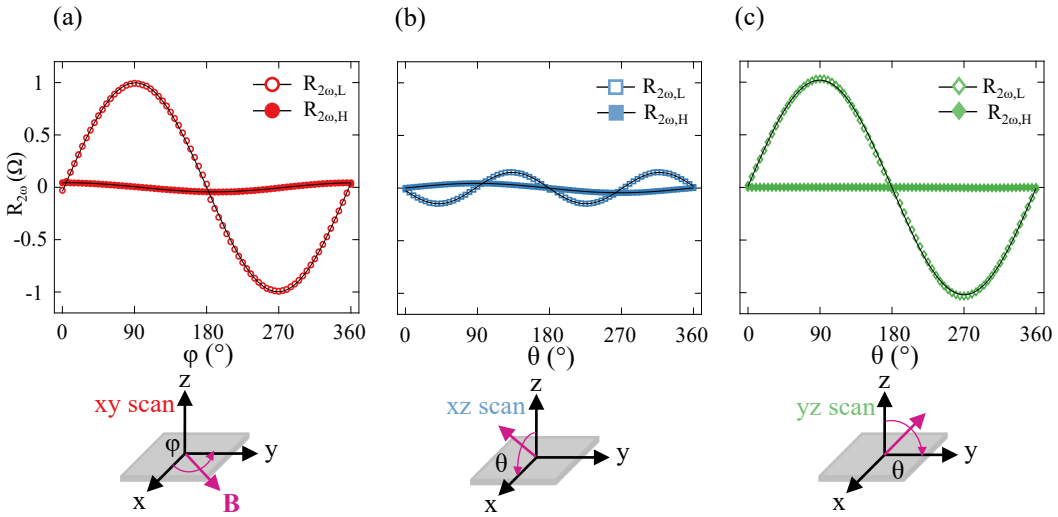

Figure 7.2: *Angular dependence of the second harmonic longitudinal (empty dots) and transverse (full dots) resistance of GeTe monolayer. (a) xy scan ($\theta = \pi/2$); (b) xz scan ($\varphi = 0$); (c) yz scan ($\varphi = \pi/2$). The magnetic field is constant and set to $B_{ext} \simeq 1.2$ T, while the injected current $j_C = 3.3 \times 10^5$ A/cm^2. The solid black lines are fitting curves of the longitudinal and transverse contribution using sine and cosine functions.*

same symmetries. Thus, it is necessary to disentangle the two signals in order to get rid of these spurious contributions. In fact, knowing the aspect ratio Z of the devices it is possible to write for ONE: $R_{2\omega,\mathrm{L}}^{\mathrm{ONE,max}} = ZR_{2\omega,\mathrm{H}}^{\mathrm{ONE,max}}$ and hence define: $R^{\mathrm{BMER,max}} = R_{2\omega,\mathrm{L}}^{\mathrm{max}} - ZR_{2\omega,\mathrm{H}}^{\mathrm{ONE,max}}$. With the geometry used, $Z = 10$.[3]

The investigation on the dependences of $R^{\mathrm{BMER,max}}$ (which means BMER for $\varphi = \pm\pi/2$ and $\theta = \pi/2$) are presented in figure 7.3, normalised at the resistance at zero field R_0. Panel (a) shows the dependence on the magnetic field of $R^{\mathrm{BMER,max}}/R_0$ at fixed current density (3.3×10^5 A/cm^2). As expected for this kind of bilinear MR, the signal is linear with the magnetic field. Panel (b) presents a comparison of the field scan between devices oriented in different crystallographic directions (the principal axes ZA and ZU). They are both linear and with a maximum relative difference of 11% at 1.27 T. For what concern the current dependence, panel (c) shows a slightly different behaviour, with a less than linear dependence of the BMER signal on the applied current, the best fit of data is with a curve of the form $R^{\mathrm{BMER,max}} \propto I^t$, with $t = 0.72$.

7.3.2 Discussion

BMER was studied measuring the dependence of this effect on the relative angle with respect to the applied magnetic field, the magnetic field magnitude and the applied current density. This second order signal shares symmetries in agreement with previous reports of BMER, together with a bilinear dependence on field and current. It was observed a slightly less than linear dependence on the current density, highlighted in panel (c) of figure 7.3. Even though there are few experimental points, it is possible to interpret this

[3] As a matter of fact, one should consider that ONE is not in principle equal along the longitudinal and the transverse direction, because the crystallographic directions are different (corresponding to ZA and ZU). The measurements shown later on, where ZA and ZU are inverted, do not show any substantial difference between the transverse resistance contributions. So, for the analysis which follows the two directions are assumed to be isotropic and the relation with the aspect ratio Z holds.

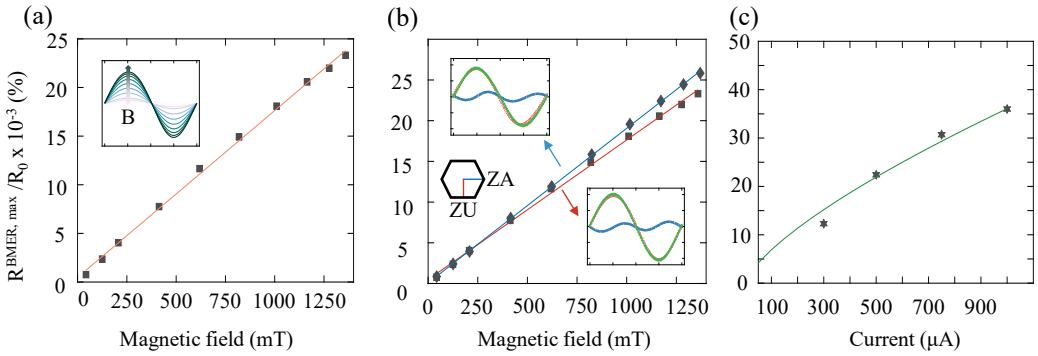

Figure 7.3: *$R^{\mathrm{BMER,max}}$ normalised at the resistance at zero magnetic field R_0 as a function of (a) the magnetic field at fixed current density (3.3×10^5 A/cm^2) (the inset shows the field dependence of the angle scans), (b) the crystallographic direction also varying the magnetic field for devices rotated 30°, corresponding to ZA and ZU directions (the two insets are the three angle scans for the ZA and ZU) and (c) the injected current at fixed magnetic field (1.2 T). The solid lines represent fits for the experimental data.*

discrepancy taking into account the possibility of the current to flow also in the substrate (Si(111)), which for high current densities acts as a shunter. Indeed, one can think the sample as a two parallel resistors (GeTe and Si channel) where, at high values of current density, the heating effect produces a decreasing of the silicon resistivity, causing a non-linear behaviour of such a channel, where the current tends to flow more easily. This can decrease the net BMER contribution.

For what regards the dependence on the crystallographic direction, even if the effect shows a small difference between ZA and ZU (11%), no *canting angle* between the scans was detected (as can be seen in the two insets of panel (b) of figure 7.3), which would be the signature of an out-of-plane spin texture [87, 90].[4] Even though ref. [21] predicts an out-of-plane contribution to the spin polarisation of the Rashba contours due to hexagonal warping, this was not detected even by SARPES measurements [22, 108]. This means that the Rashba states contributing to the conduction are actually resembling the ones of a standard Rashba system and the out-of-plane component of the spin texture is irrelevant. This is also confirmed by the absence of any non linear Hall effect, at variance with ref. [87], where *hexagonal warping* is addressed as the cause of this effect. This would suggest that states close to the valence band maximum (VBM) where k is smaller (and hence hexagonal warping is) are the main responsible for conduction. Then, the difference detected in magnitude for BMER in the two crystallographic directions could be ascribed to the slightly different Rashba parameter between ZA and ZU [21].

In this regard, recently Vaz *et al.* in ref. [93] produced a microscopic theory that allows to model BMER response of a 2DEG and, by means of the detection of BMER and QMR amplitude, to determine the Rashba parameter. This model was successfully applied for the case of 2DEG developed at the $LaAlO_3/SrTiO_3$ interface. As highlighted in ref. [94], BMER effect in GeTe is due to bulk Rashba bands, while surface Rashba components poorly contribute to this effect. In order to get a better understanding of such an effect

[4]The unidirectional behaviour in xy scan, when field is aligned along $\pm y$ is an indicator that there is an in-plane spin component locked to the momentum as in 2DEG Rashba system. If the spin texture presents also an out-of-plane component, the angle which the field and the spin expectation value are parallel at is tilted with respect to the xy plane. Hence the out-of-plane angle scan xz acquires a unidirectional behaviour (different from zero) and the other out-of-plane scan yz is shifted by a certain angle, named *canting angle*.

Material	Figure of merit η_{BMER} (cm^2/(AT))	Temperature (K)	Year	Ref.
GeTe	5.2×10^{-10}	300	2021	this work
GeTe	3.12×10^{-12}	300	2021	[94]
Ge(111)	4.2×10^{-7}	15	2020	[91]
BiTeBr	3.0×10^{-8}	2	2017	[156]
$SrTiO_3$	2.0×10^{-9}	7	2018	[90]
Bi_2Se_3	2.0×10^{-11}	60	2018	[87]
α-Sn	1.4×10^{-9}	unknown	2021	to be published[a]
$KTaO_3$	1.0×10^{-10}	2	2021	[157]

Table 7.1: *Bilinear magnetoresistance values measured in literature and compared using the figure of merit defined in eq. 7.3.*

[a]Mentioned in [91], Q. Berbedienne *et al.* (to be published).

and to address the problem of determine the Rashba parameter in such a different system, an *ad hoc* microscopic theory would be needed.

Finally, in order to make a more accurate comparison with previous results it is possible to use a suitable figure of merit η_{BMER}, as defined in ref. [91]. It could be naturally defined as:

$$\eta_{\mathrm{BMER}} = \frac{R^{\mathrm{BMER}}}{R_0 j B}. \tag{7.3}$$

For the results of this work $\eta_{\mathrm{BMER}} = 5.2 \times 10^{-10}$ cm^2/(AT). Using eq. 7.3, table 7.1 was filled to summarise BMER in other systems found in literature. The results reported in this thesis are different from the one reported in ref. [94],[5] but they are comparable with the other systems mentioned. It is worth to notice that the systems mentioned in table 7.1 are all two-dimensional systems but BiTeBr which is a polar semiconductor and all of them are measured at cryogenic temperature. Thus, GeTe represents a *unicum* because BMER directly depends on bulk states and show this unidirectional effect up to room temperature. This result could represent a starting point for the detection of such an effect in other FERSC systems.

7.4 Conclusions

The results shown in this chapter shed light on the magneto-transport properties of GeTe. The complex spin texture of such a material makes possible to observe non trivial responses when it is immersed in a magnetic field. In particular, a contribution different from standard Lorentz magnetoresistance was observed in the first order response of the longitudinal resistance, which does not change sign when the magnetic field does and scales quadratically with it. This effect is named QMR and reaches a value of 0.01% with a magnetic field of 1.3 T. Even more interesting, a contribution which scales linearly with both the current and the field was observed in the second order response. This effect has the same symmetries of other reports in literature about bilinear magnetoresistance

[5]The system measured in ref. [94] is quite different with respect the system proposed in this chapter. In particular, GeTe is remarkably thicker (64 nm) with a very low resistance and the substrate used is Al_2O_3(0001). A possible reason for the discrepancy observed can be in the different configuration of ferroelectric domains of the GeTe channel. Since the stack is quite different, also the built-in field is and the domain configuration is not known *a priori*. Since the magnetoelectric measurement probes a wide area of the Hall bar, an average signal from different domains can be detected, giving a different value of BMER.

and it is named BMER. The results were analysed in order to disentangle the contribution of thermal effects which are ubiquitous in second order responses and share the same symmetries of BMER. In order to quantify and compare the magnitude of such an effect it was defined a figure of merit, which reaches the value of $5.2 \times 10^{-10}\,\mathrm{cm}^2/(\mathrm{AT})$, higher than previous reports on such a material and comparable to other well-known two-dimensional Rashba systems and topological insulators. The behaviour of BMER with respect to crystallographic directions was investigated, as well reporting a small difference in magnitude between the two main axes ZA and ZU, ascribable to different Rashba parameters along the two directions, but excluding hexagonal warping as a possible cause of this effect and directly ascribing BMER to the spin-momentum locking of the bulk Rashba spin textures.

This opens the way to further experiments on GeTe samples in order to understand whether the polarisation affects BMER. Since the sign of the BMER amplitude is directly related to the chirality (i.e., the sign of circulation of the spins) of the Rashba bands, one could expect that changing the ferroelectric polarisation and thus inverting the spin textures it would be possible to see a sign inversion also for the BMER amplitude. This result was not achieved so far. This experiment could be realised by applying a gate voltage to the channel and exploiting the silicon substrate as a bottom contact. This represents a challenge because the difficulties to achieve the complete ferroelectric switching of the entire Hall bar channel. Nevertheless, it could be faced shrinking the dimensions of the device to $\sim 100\,\mathrm{nm}$, going in the direction of a single (ferroelectric) domain configuration. Moreover, a sufficiently thick insulating interlayer should be interposed between GeTe and the metallic gate in order to avoid any shunting effect. This could be achieved by a thicker Si_3N_4 ($50 - 100\,\mathrm{nm}$) which has reliable insulating properties and it does not cause ion migration with high applied voltage (as can happen with oxides), as already demonstrated in previous works.

Also other group-IV tellurides sharing similar band structure could present such an effect and they are interesting candidates to further investigate magneto-transport of FERSC.

CHAPTER 8

Conclusions

This work dealt with two distinct topics: from one side the investigation of the band structures and spin textures, by SARPES and magneto-transport experiments, of two group-IV tellurides belonging to ferroelectric Rashba semiconductors (FERSC) class of material, GeTe and SnTe, while on the other side the development of a two dimensional spin detector with the aim of drastically speed up SARPES measurements. These two topics are intimately related by the intrinsic necessity to study the properties of such materials by means of spectroscopic tools in order to understand the rich nature of their band structure.

In **chapter** 5 the growth and the structural characterisation of Ge-doped SnTe films was covered. The investigation of their band structure was conducted by SARPES. The doping process was needed in order to establish bulk Rashba bands in the alloy band structure. Moreover, they represent a trace of the underlying ferroelectricity of the samples which was shown to be present at least up to room temperature and down to a concentration of Ge of $\sim 31\%$. The data observed by ARPES show tunable Rashba bands (in terms of Rashba parameter α_{R} and Rashba k vector) which reflect to a tunibility of the ferroelectric properties of such alloys. The trend found in measurements was validated also by DFT calculations, performed by co-workers.

In **chapter** 6 the realisation of a prototype of a 2D spin detector was presented. The growth of free-standing magnetic films with a maximum thickness of 10 nm, consisting of Co-based and CoFeB-based heterostructures, was optimised on few monolayers of graphene, reaching a high control of roughness. The very fragile nature of suspended membranes forced the investigation of different deposition processes and graphene monolayers number in order to find the parameters to obtain the largest number of intact devices, found up to 94%. The magnetic properties mimic the ones on rigid substrate. Both in-plane and out-of-plane magnetic anisotropy were reached with a coercive field for both the configuration of ~ 3 mT. The mechanical reliability was quantified and tested with

atomic force spectroscopy finding a maximum load of 7300 nN for samples with 6-8 ML of graphene. Also transmission measurements were performed with a spin polarised electron beam, unveiling the expected exponentially decreasing behaviour for a small number of broken membranes.

In **chapter** 7 GeTe was studied from the magneto-transport point of view. Spectroscopic measurements on this material were recently performed, so this chapter was devoted to the influence of the band structure in transport properties. Its bulk Rashba effect leads to unconventional magnetoresistive effects that were detected in the first and second order responses. A quadratic magnetoresistance was observed up to 0.01% at 1.3 T in analogy to the well-known anisotropic magnetoresistance of ferromagnetic films and a bilinear behaviour (with respect current and field) was also reported to be up to 0.02% at 1.3 T. This is a direct manifestation of the complex spin texture of this material and, in particular, of spin-momentum locking. This kind of measurement represents an alternative route to infer information about electronic band structure from the macroscopic perspective of magneto-transport, which, correlated to spectroscopic characterisation, returns a more complete picture of the physics of this kind of materials.

The perspectives of this work are several. The spectroscopic data suggest that an engineering of band structure is possible in FERSC compounds and the coexistance of multiple non trivial state of matter could be achieved, giving a lot of possibilities for further investigations both on SnTe and on other components of FERSC class from the fundamental stand point and also in view of exploiting them into devices. This very rich physics makes them intriguing candidates for transport experiments and spin-obit torques devices. This represents also a challenge for theoretical calculations because the right matching of conditions could predict new materials in which these behaviours could be observed.

Moreover, the transport experiments performed on GeTe-based devices open the way to a deeper investigation of group-IV tellurides. Second order response unidirectional effects are ubiquitous in spin-orbitronics systems and much interest nowadays is devoted to non linear Hall effects. The study of this new class of materials could bring new insights in this kind of physics, possibly disclosing new phenomena which could be the bricks for the development of new devices.

Finally, the prototype spin detector realised represents a starting point for further developments and studies. The intrinsic two-dimensional detection would bring a drastic decrease of the experiments duration and an increase of the signal-to-noise ratio. The integration in a real ARPES set-up could validate in a real-life environment the performances of this scheme.

APPENDIX $\mathcal{A}$

Angular dependencies of torques and thermal effects in angle scans

In the following appendix, analytic expressions for damping-like and field-like torques are derived explicitly together with the possible thermal effects which could affect transport in the three main angle scans (i.e., along xy, xz and yz planes). The expressions which follow can be exploited for any heterostructure which displays SOT and which is subjected to Joule heating due to the injection of a current.

A.1 Spin-Orbit torques in angle scans

The second harmonic expressions for the transverse and longitudinal resistance read as follows:

$$\begin{aligned} R_{2\omega}^{\mathrm{Hall,SOT}} = &\left(R_{\mathrm{AHE}} - 2R_{\mathrm{PHE}}\cos\theta\sin\left(2\varphi\right)\right)\frac{\mathrm{d}\cos\theta}{\mathrm{d}\theta_B}\frac{B_I^{\theta}}{\cos\left(\theta_B-\theta\right)B_{\mathrm{ext}}} \\ &+ R_{\mathrm{PHE}}\sin^2\theta\frac{\mathrm{d}\sin\left(2\varphi\right)}{\mathrm{d}\varphi_B}\frac{B_I^{\varphi}}{\sin\theta_B\cos\left(\varphi_B-\varphi\right)B_{\mathrm{ext}}} \end{aligned} \tag{A.1}$$

and

$$\begin{aligned} R_{2\omega}^{\mathrm{Long,SOT}} = &\left[\left(R^x - R^z\right)\cos^2\varphi + \left(R^y - R^z\right)\sin^2\varphi\right]\frac{\mathrm{d}\sin^2\theta}{\mathrm{d}\theta_B}\frac{B_I^{\theta}}{\cos(\theta_B-\theta)B_{\mathrm{ext}}} \\ &+ \left[\left(R^x - R^y\right)\sin^2\theta\right]\frac{\mathrm{d}\cos^2\varphi}{\mathrm{d}\varphi_B}\frac{B_I^{\varphi}}{\sin\theta_B\cos(\varphi_B-\varphi)B_{\mathrm{ext}}}, \end{aligned} \tag{A.2}$$

where θ_B and φ_B are the polar and azimuthal angle identifying the direction of the external magnetic field, θ and φ regard the magnetisation direction and B_I^{θ} and B_I^{φ} are the polar

and azimuthal projection of the current-induced magnetic field (definitions of the angle are pictorially represented in figure 7.1(b)).

If the magnetisation is considered to be saturated along the field direction, $\theta \equiv \theta_B$ and $\varphi \equiv \varphi_B$. Eqs. A.1 and A.2 become:

$$\begin{aligned} R_{2\omega}^{\mathrm{Hall,SOT}} = & \left(R_{\mathrm{AHE}} - 2R_{\mathrm{PHE}} \cos\theta \sin\left(2\varphi\right)\right) \frac{\mathrm{d}\cos\theta}{\mathrm{d}\theta} \frac{B_I^{\theta}}{B_{\mathrm{ext}}} \\ & + R_{\mathrm{PHE}} \sin^2\theta \frac{\mathrm{d}\sin\left(2\varphi\right)}{d\varphi} \frac{B_I^{\varphi}}{\sin\theta B_{\mathrm{ext}}} \end{aligned} \tag{A.3}$$

and

$$\begin{aligned} R_{2\omega}^{\mathrm{Long,SOT}} = & \left[\left(R^x - R^z\right)\cos^2\varphi + \left(R^y - R^z\right)\sin^2\varphi\right] \frac{\mathrm{d}\sin^2\theta}{\mathrm{d}\theta} \frac{B_I^{\theta}}{B_{\mathrm{ext}}} \\ & + \left[\left(R^x - R^y\right)\sin^2\theta\right] \frac{\mathrm{d}\cos^2\varphi}{\mathrm{d}\varphi} \frac{B_I^{\varphi}}{\sin\theta B_{\mathrm{ext}}}. \end{aligned} \tag{A.4}$$

Depending on the angle scan considered (xy,xz or yz), the terms B_I^{φ} and B_I^{θ} have a different dependence with respect to B_{AD} and B_{FL}[1]. Considering the following directions for B_{AD} and B_{FL}:

$$\begin{cases} \mathbf{B}_{\mathrm{AD}} & = B_{\mathrm{AD}}\left(\mathbf{m} \times \hat{\mathbf{y}}\right) \\ \mathbf{B}_{\mathbf{FL}} & = B_{\mathrm{FL}}\left(\hat{\mathbf{y}}\right) \end{cases}. \tag{A.5}$$

A.1.1 xy scan

In spherical coordinates $\mathbf{B}_{\mathrm{AD}}$ and $\mathbf{B}_{\mathrm{FL}}$ read:

$$\begin{cases} \mathbf{B}_{\mathrm{AD}} & = B_{\mathrm{AD}}\left[\left(\cos\varphi\cos\theta\right)\hat{\mathbf{e}}_r - \left(\cos\varphi\sin\theta\right)\hat{\mathbf{e}}_{\theta}\right] \\ \mathbf{B}_{\mathrm{FL}} & = B_{\mathrm{FL}}\left[\sin\varphi\hat{\mathbf{e}}_r + \cos\varphi\hat{\mathbf{e}}_{\varphi}\right]. \end{cases} \tag{A.6}$$

The $\hat{\mathbf{e}}_{\mathbf{r}}$ contribution of SOT parallel is the magnetisation vector, hence it is ineffective on the magnetization dynamics. Only polar and azimuthal contributions of the SOT fields enter in the equation of SOTs.

Setting $\theta = \pi/2$ and $\varphi \in [0, 2\pi]$ and substituting in eqs. A.3 and A.4:

$$R_{2\omega}^{\mathrm{Hall,AD-SOT}} = R_{\mathrm{AHE}} \cos\varphi \frac{B_{\mathrm{AD}}}{B_{\mathrm{ext}}}, \tag{A.7}$$

$$R_{2\omega}^{\mathrm{Hall,FL-SOT}} = R_{\mathrm{PHE}} \left(2\cos^3\varphi - \cos\varphi\right) \frac{B_{\mathrm{FL}}}{B_{\mathrm{ext}}}, \tag{A.8}$$

$$R_{2\omega}^{\mathrm{Long,AD-SOT}} = 0, \tag{A.9}$$

$$R_{2\omega}^{\mathrm{Long,FL-SOT}} = 2\left(R^x - R^y\right)\left(\sin\varphi - \sin^3\varphi\right) \frac{B_{\mathrm{FL}}}{B_{\mathrm{ext}}}. \tag{A.10}$$

[1] According to the system of coordinate chosen and to angle scan direction for θ and φ – which are clockwise and counterclockwise, respectively – the resulting spherical coordinate system is left-handed. This explains the possible inconsistencies in the sign between different notations present in literature.

A.1.2 xz scan

In spherical coordinates $\mathbf{B}_{\mathrm{AD}}$ and $\mathbf{B}_{\mathrm{FL}}$ read:

$$\begin{cases} \mathbf{B}_{\mathrm{AD}} & = B_{\mathrm{AD}} \left[(\sin\theta\cos\theta(1-\cos\varphi))\,\hat{\mathbf{e}}_r - \left(\cos^2\theta\cos\varphi + \sin^2\theta\right)\hat{\mathbf{e}}_\theta + (\cos\theta\sin\varphi)\,\hat{\mathbf{e}}_\varphi \right] \\ \mathbf{B}_{\mathrm{FL}} & = B_{\mathrm{FL}} \left[\sin\varphi\hat{\mathbf{e}}_r + \cos\varphi\hat{\mathbf{e}}_\varphi \right] \end{cases}. \tag{A.11}$$

Setting $\theta \in [0, 2\pi]$ and $\varphi = 0$ and substituting in eqs. A.3 and A.4:

$$R_{2\omega}^{\mathrm{Hall,AD-SOT}} = R_{\mathrm{AHE}} \sin\theta \frac{B_{\mathrm{AD}}}{B_{\mathrm{ext}}}, \tag{A.12}$$

$$R_{2\omega}^{\mathrm{Hall,FL-SOT}} = 2R_{\mathrm{PHE}} \sin\theta \frac{B_{\mathrm{FL}}}{B_{\mathrm{ext}}}, \tag{A.13}$$

$$R_{2\omega}^{\mathrm{Long,AD-SOT}} = -\left(R^x - R^z\right)\sin(2\theta)\frac{B_{\mathrm{AD}}}{B_{\mathrm{ext}}}, \tag{A.14}$$

$$R_{2\omega}^{\mathrm{Long,FL-SOT}} = 0. \tag{A.15}$$

A.1.3 yz scan

In spherical coordinates $\mathbf{B}_{\mathrm{AD}}$ and $\mathbf{B}_{\mathrm{FL}}$ read:

$$\begin{cases} \mathbf{B}_{\mathrm{AD}} & = B_{\mathrm{AD}} \left[(\sin\theta\cos\theta\cos\varphi)\,\hat{\mathbf{e}}_r + (\cos^2\theta\cos\varphi)\,\hat{\mathbf{e}}_\theta + (\sin\varphi)\,\hat{\mathbf{e}}_\varphi \right] \\ \mathbf{B}_{\mathrm{FL}} & = B_{\mathrm{FL}} \left[\sin\theta\hat{\mathbf{e}}_r + \cos\theta\hat{\mathbf{e}}_\theta \right] \end{cases}. \tag{A.16}$$

Setting $\theta \in [0, 2\pi]$ and $\varphi = \pi/2$ and substituting in eqs. A.3 and A.4:

$$R_{2\omega}^{\mathrm{Hall,AD-SOT}} = -R_{\mathrm{PHE}} \sin(2\theta)\frac{B_{\mathrm{AD}}}{B_{\mathrm{ext}}}, \tag{A.17}$$

$$R_{2\omega}^{\mathrm{Hall,FL-SOT}} = -\frac{R_{\mathrm{PHE}}}{2} \sin(2\theta)\frac{B_{\mathrm{FL}}}{B_{\mathrm{ext}}}, \tag{A.18}$$

$$R_{2\omega}^{\mathrm{Long,AD-SOT}} = 0, \tag{A.19}$$

$$R_{2\omega}^{\mathrm{Long,FL-SOT}} = 2\left(R^y - R^z\right)\left(\sin\theta - \sin^3\theta\right)\frac{B_{\mathrm{FL}}}{B_{\mathrm{ext}}}. \tag{A.20}$$

All the angular dependences of SOT are summed up in figure A.1.

A.2 Thermal effects in angle scans

In the following the angular dependences of anomalous Nernst effect (ANE) and anisotropic magneto-thermopower (AMTEP)/planar Nernst effect (PNE) (the transverse manifestation of AMTEP) are considered in second harmonic transverse and longitudinal resistances. Considering an arbitrary temperature gradient $\nabla\mathbf{T} = (\nabla T_x, \nabla T_y, \nabla T_z)$ and a saturated magnetization along the external field direction $\hat{\mathbf{m}} = (\sin\theta\cos\varphi, \sin\theta\sin\varphi, \cos\theta)$, they have these general expressions.

ANE:

$$R_{2\omega}^{\mathrm{Long,ANE}} \propto -\nabla T_y \cos\theta + \nabla T_z \sin\theta \sin\varphi, \tag{A.21}$$
$$R_{2\omega}^{\mathrm{Hall,ANE}} \propto \nabla T_z \sin\theta \cos\varphi - \nabla T_x \cos\theta. \tag{A.22}$$

AMTEP:

$$R_{2\omega}^{\mathrm{Long,AMTEP}} \propto \nabla T_x \left(\sin^2\theta \cos^2\varphi + \sin^2\theta \sin^2\varphi\right), \tag{A.23}$$
$$R_{2\omega}^{\mathrm{Hall,AMTEP}} \propto \nabla T_y \left(\sin^2\theta \cos^2\varphi + \sin^2\theta \sin^2\varphi\right). \tag{A.24}$$

PNE:

$$R_{2\omega}^{\mathrm{Long,PNE}} \propto \nabla T_y \sin^2\theta \sin(2\varphi) + \nabla T_z \sin(2\theta) \cos^2\varphi, \tag{A.25}$$
$$R_{2\omega}^{\mathrm{Hall,PNE}} \propto \nabla T_x \sin^2\theta \sin(2\varphi) + \nabla T_z \sin(2\theta) \sin^2\varphi. \tag{A.26}$$

According to the relative angle scan the equations become:

xy scan – $\theta = \pi/2$**,** $\varphi \in [0, 2\pi]$

ANE:

$$R_{2\omega}^{\mathrm{Long,ANE}} \propto \nabla T_z \sin\varphi, \tag{A.27}$$
$$R_{2\omega}^{\mathrm{Hall,ANE}} \propto \nabla T_z \cos\varphi. \tag{A.28}$$

AMTEP:

$$R_{2\omega}^{\mathrm{Long,AMTEP}} \propto \nabla T_x, \tag{A.29}$$
$$R_{2\omega}^{\mathrm{Hall,AMTEP}} \propto \nabla T_y. \tag{A.30}$$

PNE:

$$R_{2\omega}^{\mathrm{Long,PNE}} \propto \nabla T_y \sin(2\varphi), \tag{A.31}$$
$$R_{2\omega}^{\mathrm{Hall,PNE}} \propto \nabla T_x \sin(2\varphi). \tag{A.32}$$

xz scan – $\theta \in [0, 2\pi]$**,** $\varphi = 0$

ANE:

$$R_{2\omega}^{\mathrm{Long,ANE}} \propto -\nabla T_y \cos\theta, \tag{A.33}$$
$$R_{2\omega}^{\mathrm{Hall,ANE}} \propto \nabla T_z \sin\theta - \nabla T_x \cos\theta. \tag{A.34}$$

AMTEP:

$$R_{2\omega}^{\mathrm{Long,AMTEP}} \propto \nabla T_x \sin^2\theta, \tag{A.35}$$
$$R_{2\omega}^{\mathrm{Hall,AMTEP}} \propto \nabla T_y \sin^2\theta. \tag{A.36}$$

PNE:

$$R_{2\omega}^{\mathrm{Long,PNE}} \propto \nabla T_z \sin(2\theta), \tag{A.37}$$
$$R_{2\omega}^{\mathrm{Hall,PNE}} = 0. \tag{A.38}$$

yz scan – $\theta \in [0, 2\pi]$**,** $\varphi = \pi/2$

ANE:

$$R_{2\omega}^{\mathrm{Long,ANE}} \propto -\nabla T_y \cos\theta + \nabla T_z \sin\theta, \tag{A.39}$$
$$R_{2\omega}^{\mathrm{Hall,ANE}} \propto -\nabla T_x \cos\theta. \tag{A.40}$$

AMTEP:

$$R_{2\omega}^{\mathrm{Long,AMTEP}} \propto \nabla T_x \sin^2\varphi, \tag{A.41}$$
$$R_{2\omega}^{\mathrm{Hall,AMTEP}} \propto \nabla T_y \sin^2\varphi. \tag{A.42}$$

PNE:

$$R_{2\omega}^{\mathrm{Long,PNE}} = 0, \tag{A.43}$$
$$R_{2\omega}^{\mathrm{Hall,PNE}} \propto \nabla T_z \sin(2\theta). \tag{A.44}$$

All the angular dependences of thermal effects are summed up in figure A.2.

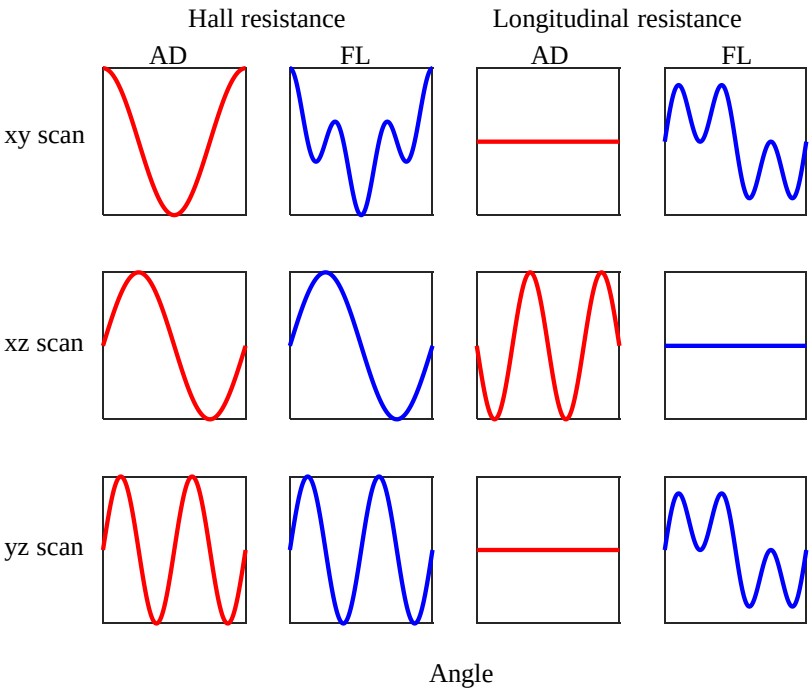

Figure A.1: *Angular dependences of damping-like and field-like SOT in Hall and longitudinal resistance.*

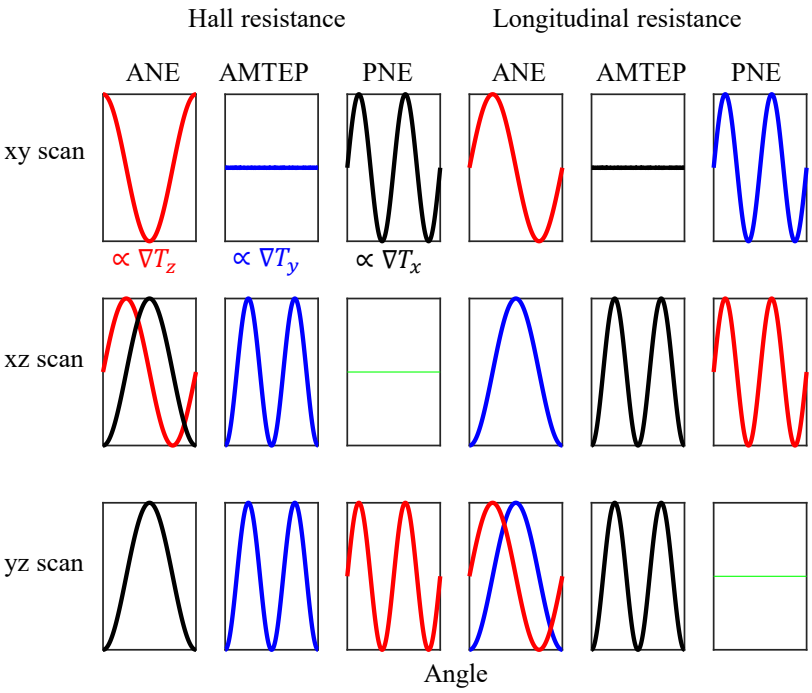

Figure A.2: *Angular dependences of thermal effects in Hall and longitudinal resistance.*

APPENDIX $\mathcal{B}$

Decapping protocol for group-IV tellurides capped with tellurium

B.1 Introduction

In the following appendix, the decapping protocol used for restore the surface of tellurium-capped group-IV tellurides is illustrated. The following procedure of re-preparation of the surface was employed both for SnTe samples measured by SARPES and for GeTe samples in order to grow proper heterostructures for transport measurements.

B.2 Decapping protocol

An *ad hoc* protocol which can be used in UHV cluster tools[1] was validated in order to remove the Te capping layer. Thermal annealing is the typical tool used for the desorption of capping layers along with surface contaminants (oxygen, organic molecules,...). The issue for this kind of sample is that annealing is also accompanied by the diffusion of oxygen from the oxidised capping layer of TeO_x towards the interface to the GeTe layer. This causes the bonding with Ge (or Sn) atoms preferentially. Then, the desorption of oxygen from the matrix requires even higher temperatures which could cause the evaporation of the group-IV telluride layer. Hence, a different method is used, with the following recipe is followed:

(i) **Oxide removal.** A soft rastering Ar sputtering is firstly performed on the sample with ions at energy of $1.1 - 1.4\,\text{keV}$ at an angle of $60°$ between the beam and the sample and with a partial pressure of Ar of $2 \times 10^{-8}\,\text{mbar}$. The efficiency of the process can be checked comparing XPS spectra before and after the process, looking

[1] as the one present in Polifab facility, described in section 4.1.1, as well the one used at APE beam-line at Elettra synchrotron.

at the intensities of oxygen and carbon and at the chemical shift of Te_{3d} doublet, that is indicative of the Te oxidation state.

(ii) **Desorption of Te capping.** The desorption is performed with a thermal annealing in UHV at $\sim 250\,^{\circ}C$ until the chamber recovers its base pressure ($\sim 1 \times 10^{-10}$ mbar). This temperature allows also to maintain a highly ordered surface and the correct stoichiometry of the sample.

(iii) **Check for crystallinity and stoichiometry.** The crystallographic quality can be checked with diffraction tools, such as low energy electron diffraction (LEED), reflection high-energy electron diffraction (RHEED) or by spectroscopic tools such as X-ray photoelectron diffraction (XPD). All of them retrieve the lattice order of the crystal and give information about the quality of the film. The sample stoichiometry is measured by XPS, comparing the normalised intensities[2] of the peaks of Ge_{3d}/Sn_{4d} with the one of Te_{4d}.

[2]The intensities are normalised by the cross-section, the inelastic mean free path of electrons and the transmission of the analyser. All these parameters depend on the kinetic energy of the photoemitted electrons and then on the photon energy of the source, which could be synchrotron radition as well as produced by Al or Mg targets.

List of Figures

1.1 Ferroelectric Rashba semiconductors main properties. 4
1.2 State-of-art spin detectors performances comparison. 6

2.1 Ferroelectricity general description. 11
2.2 Physics of Rashba effect and examples of well-known materials. 14
2.3 Ordinary and spin Hall effects 14
2.4 Spin-to-charge conversion phenomena. 16
2.5 Physics of bilinear magnetoelectric resistance in a Rashba system. 17
2.6 Spin-orbit torques generation in a FM/NM system. 18
2.7 Germanium telluride Brillouin zone and band structure. 20
2.8 Band engineering of tin telluride band structure tuning the distorsion parameter. 21

3.1 Mechanisms of the interaction between spins and magnetic materials 27
3.2 Sketch of the basic principle of Mott detection. 27
3.3 Schematics of 2D spin detectors. 29

4.1 Deposition and characterisation cluster tool present in Polifab facility. . . . 32
4.2 Optical lithography workflow. 35
4.3 Hall bar geometry imaged with optical microscope. 36
4.4 Scheme of a typical ARPES experiment. 39
4.5 Optical set-up for the measurement of Faraday effect in free-standing films. 41
4.7 spin-polarised electron gun and GaAS photocathode working principle. . . 43
4.6 Absorbed current spectroscopy of the oxidated iron reference samples. . . . 43

5.1 Characterisation after the re-preparation protocol of GeTe substrate and of Ge-doped SnTe films. 47
5.2 XPS measurements for the doping characterisation of the alloy $Sn_{1-x}Ge_xTe$. 48
5.3 Bulk and surface Brillouin zone of SnTe. 49
5.4 ARPES measurements with different photon energies. 50
5.5 Integrated counts for photon energy dependent carpets of sample ST1. . . . 50

5.6 ARPES measurements with different Ge concentrations. 51
5.7 Temperature dependent ARPES measurements. 51
5.8 SARPES characterisation of bulk Rashba bands and topological surface states. 52
5.9 DFT calculations of the Rashba k vector and of the Rashba parameter as a function of the Ge concentration. 54

6.1 2D spin-resolved map. 55
6.2 Spin polarimeter diagram. 56
6.3 Spin detector design. 58
6.4 Workflow definition and SEM imaging of the membranes. 60
6.5 Mechanical reliability analysis through SEM imaging. 61
6.6 AFM topography for MBE and magnetron sputtering samples. 61
6.7 AFM force spectroscopy measurements. 62
6.8 Magnetic properties measured by Faraday effect. 64
6.9 Spin filtering characterisation set-up schematic. 65
6.10 Spin filtering measurements. 66
6.11 Calculation of the transmission factors. 66
6.12 Spin filtering simulations. 67
6.13 Spin asymmetry measurement. 68

7.1 First harmonic longitudinal resistance of GeTe monolayer. 74
7.2 Angular dependence of the second harmonic longitudinal and transverse resistance of GeTe monolayer. 75
7.3 Field, current and crystallographic direction dependence of the BMER signal. 76

A.1 Angular dependences of SOT in Hall and longitudinal resistance. 86
A.2 Angular dependences of thermal effects in Hall and longitudinal resistance. 86

List of Tables

1.1 State-of-art spin detectors performances. 6

5.1 SnTe sample list. 49

6.1 Free-standing samples notation. 59
6.2 AFM measurements of roughness parameters. 62

7.1 BMER signals in literature. 77

Bibliography

[1] Sara Varotto et al. “Room-temperature ferroelectric switching of spin-to-charge conversion in germanium telluride”. In: *Nature Electronics* (2021), pp. 1–8.

[2] Marco Asa et al. “Epitaxy and controlled oxidation of chromium ultrathin films on ferroelectric BaTiO3 templates”. In: *Journal of Crystal Growth* 558 (2021), p. 126012.

[3] Marta Ghirardello et al. “An investigation into the synthesis of cadmium sulfide pigments for a better understanding of their reactivity in artworks”. In: *Dyes and Pigments* 186 (2021), p. 108998.

[4] Sara Varotto et al. “Investigation of charge-to-spin conversion in GeTe”. In: *Spintronics XI*. Vol. 10732. International Society for Optics and Photonics. 2018, p. 107320C.

[5] Wolfgang Pauli. “Über den Einfluß der Geschwindigkeitsabhängigkeit der Elektronenmasse auf den Zeemaneffekt”. In: *Zeitschrift für Physik* 31.1 (1925), pp. 373–385.

[6] Wolfgang Pauli. “Exclusion principle and quantum mechanics”. In: *Writings on physics and philosophy*. Springer, 1994, pp. 165–181.

[7] Albert Einstein. “Experimenteller nachweis der ampereschen molekularströme”. In: *Naturwissenschaften* 3.19 (1915), pp. 237–238.

[8] Victor Galitski and Ian B Spielman. “Spin–orbit coupling in quantum gases”. In: *Nature* 494.7435 (2013), pp. 49–54.

[9] R Winkler et al. *Spin-Orbit Coupling in Two-Dimensional Electron and Hole Systems*. Vol. 41. Springer, 2003.

[10] Aurelien Manchon et al. “New perspectives for Rashba spin–orbit coupling”. In: *Nature materials* 14.9 (2015), pp. 871–882.

[11] Martin Leijnse and Karsten Flensberg. “Introduction to topological superconductivity and Majorana fermions”. In: *Semiconductor Science and Technology* 27.12 (2012), p. 124003.

[12] Bernard Dieny, Ronald B Goldfarb, and Kyung-Jin Lee. *Introduction to magnetic random-access memory*. John Wiley & Sons, 2016.

[13] Aurelien Manchon et al. “Current-induced spin-orbit torques in ferromagnetic and antiferromagnetic systems”. In: *Reviews of Modern Physics* 91.3 (2019), p. 035004.

[14] Can Onur Avci et al. “Current-induced switching in a magnetic insulator”. In: *Nature materials* 16.3 (2017), pp. 309–314.

[15] Peter Wadley et al. “Electrical switching of an antiferromagnet”. In: *Science* 351.6273 (2016), pp. 587–590.

[16] Sasikanth Manipatruni et al. “Scalable energy-efficient magnetoelectric spin–orbit logic”. In: *Nature* 565.7737 (2019), pp. 35–42.

[17] Silvia Picozzi. "Ferroelectric Rashba semiconductors as a novel class of multifunctional materials". In: *Frontiers in Physics* 2 (2014), p. 10.

[18] Yu A Bychkov and Emmanuel I Rashba. "Oscillatory effects and the magnetic susceptibility of carriers in inversion layers". In: *Journal of physics C: Solid state physics* 17.33 (1984), p. 6039.

[19] K Ishizaka et al. "Giant Rashba-type spin splitting in bulk BiTeI". In: *Nature materials* 10.7 (2011), pp. 521–526.

[20] MS Bahramy, R Arita, and N Nagaosa. "Origin of giant bulk Rashba splitting: Application to BiTeI". In: *Physical Review B* 84.4 (2011), p. 041202.

[21] Domenico Di Sante et al. "Electric control of the giant Rashba effect in bulk GeTe". In: *Advanced materials* 25.4 (2013), pp. 509–513.

[22] Christian Rinaldi et al. "Ferroelectric control of the spin texture in GeTe". In: *Nano letters* 18.5 (2018), pp. 2751–2758.

[23] Hania Djani et al. "Rationalizing and engineering Rashba spin-splitting in ferroelectric oxides". In: *npj Quantum Materials* 4.1 (2019), pp. 1–6.

[24] Jagoda Sławińska et al. "Giant spin Hall effect in two-dimensional monochalcogenides". In: *2D Materials* 6.2 (2019), p. 025012.

[25] JF Scott. "Applications of modern ferroelectrics". In: *science* 315.5814 (2007), pp. 954–959.

[26] Victor M Edelstein. "Spin polarization of conduction electrons induced by electric current in two-dimensional asymmetric electron systems". In: *Solid State Communications* 73.3 (1990), pp. 233–235.

[27] Jairo Sinova et al. "Spin hall effects". In: *Reviews of modern physics* 87.4 (2015), p. 1213.

[28] Federico Bottegoni et al. "Spin-Hall voltage over a large length scale in bulk germanium". In: *Physical review letters* 118.16 (2017), p. 167402.

[29] K Uchida et al. "Observation of the spin Seebeck effect". In: *Nature* 455.7214 (2008), pp. 778–781.

[30] Ioan Mihai Miron et al. "Perpendicular switching of a single ferromagnetic layer induced by in-plane current injection". In: *Nature* 476.7359 (2011), pp. 189–193.

[31] Paul Noël et al. "Non-volatile electric control of spin–charge conversion in a SrTiO 3 Rashba system". In: *Nature* 580.7804 (2020), pp. 483–486.

[32] Mei Fang et al. "Tuning the interfacial spin-orbit coupling with ferroelectricity". In: *Nature communications* 11.1 (2020), pp. 1–8.

[33] E Kisker, R Clauberg, and W Gudat. "Electron spectrometer for spin-polarized angle-and energy-resolved photoemission from ferromagnets". In: *Review of Scientific Instruments* 53.8 (1982), pp. 1137–1144.

[34] Riccardo Bertacco et al. "Spin and energy analysis of electron beams: Coupling a polarimeter based on exchange scattering to a hemispherical analyzer". In: *Review of scientific instruments* 73.11 (2002), pp. 3867–3871.

[35] Taichi Okuda et al. "A new spin-polarized photoemission spectrometer with very high efficiency and energy resolution". In: *Review of Scientific Instruments* 79.12 (2008), p. 123117.

[36] Chiara Bigi et al. "Very efficient spin polarization analysis (VESPA): new exchange scattering-based setup for spin-resolved ARPES at APE-NFFA beamline at Elettra". In: *Journal of synchrotron radiation* 24.4 (2017), pp. 750–756.

[37] Fuhao Ji et al. "Multichannel exchange-scattering spin polarimetry". In: *Physical review letters* 116.17 (2016), p. 177601.

[38] T Övergaard et al. "Free-standing magnetic nano-membranes for electron spin-filtering applications". In: *arXiv preprint arXiv:1709.03838* (2017).

[39] G Schönhense and HC Siegmann. "Transmission of electrons through ferromagnetic material and applications to detection of electron spin polarization". In: *Annalen der Physik* 505.5 (1993), pp. 465–474.

[40] D Oberli et al. “Total scattering cross section and spin motion of low energy electrons passing through a ferromagnet”. In: *Physical review letters* 81.19 (1998), p. 4228.

[41] GC Burnett, TJ Monroe, and FB Dunning. “High-efficiency retarding-potential Mott polarization analyzer”. In: *Review of scientific instruments* 65.6 (1994), pp. 1893–1896.

[42] Dehong Yu et al. “Characterisation and application of a SPLEED-based spin polarisation analyser”. In: *Surface Science* 601.24 (2007), pp. 5803–5808.

[43] A Winkelmann et al. “High efficiency electron spin polarization analyzer based on exchange scattering at Fe/ W (001)”. In: *Review of Scientific Instruments* 79.8 (2008), p. 083303.

[44] M Kolbe et al. “Highly efficient multichannel spin-polarization detection”. In: *Physical review letters* 107.20 (2011), p. 207601.

[45] Joseph Valasek. “Piezo-electric and allied phenomena in Rochelle salt”. In: *Physical review* 17.4 (1921), p. 475.

[46] Joseph Valasek. “Piezo-electric activity of Rochelle salt under various conditions”. In: *Physical Review* 19.5 (1922), p. 478.

[47] Shepard Roberts. “Dielectric and piezoelectric properties of barium titanate”. In: *Physical Review* 71.12 (1947), p. 890.

[48] James F Scott and Carlos A Paz De Araujo. “Ferroelectric memories”. In: *Science* 246.4936 (1989), pp. 1400–1405.

[49] RD King-Smith and David Vanderbilt. “Theory of polarization of crystalline solids”. In: *Physical Review B* 47.3 (1993), p. 1651.

[50] R Resta. “Polarization as a berry phase”. In: *Europhysics News* 28.1 (1997), pp. 18–20.

[51] Manuel Bibes and Agnès Barthélémy. “Towards a magnetoelectric memory”. In: *Nature materials* 7.6 (2008), pp. 425–426.

[52] Nicola A Spaldin, Sang-Wook Cheong, and Ramamoorthy Ramesh. “Multiferroics: Past, present, and future”. In: *Phys. Today* 63.10 (2010), pp. 38–43.

[53] S Das et al. “Observation of room-temperature polar skyrmions”. In: *Nature* 568.7752 (2019), pp. 368–372.

[54] Susan Trolier-McKinstry and Peter Muralt. “Thin film piezoelectrics for MEMS”. In: *Journal of Electroceramics* 12.1 (2004), pp. 7–17.

[55] P Muralt. “Ferroelectric thin films for micro-sensors and actuators: a review”. In: *Journal of micromechanics and microengineering* 10.2 (2000), p. 136.

[56] André Chanthbouala et al. “A ferroelectric memristor”. In: *Nature materials* 11.10 (2012), pp. 860–864.

[57] Karin M Rabe et al. “Modern physics of ferroelectrics: Essential background”. In: *Physics of Ferroelectrics* (2007), pp. 1–30.

[58] Daniel Sando, A Barthélémy, and M Bibes. “BiFeO3 epitaxial thin films and devices: past, present and future”. In: *Journal of Physics: Condensed Matter* 26.47 (2014), p. 473201.

[59] Nicola A Spaldin. “A beginner’s guide to the modern theory of polarization”. In: *Journal of Solid State Chemistry* 195 (2012), pp. 2–10.

[60] AF Devonshire. “Theory of ferroelectrics”. In: *Advances in physics* 3.10 (1954), pp. 85–130.

[61] Premi Chandra and Peter B Littlewood. “A Landau primer for ferroelectrics”. In: *Physics of ferroelectrics* (2007), pp. 69–116.

[62] Hendrik Antoon Kramers. “Théorie générale de la rotation paramagnétique dans les cristaux”. In: *Proc. Acad. Amst* 33.6 (1930).

[63] Beomyoung Kim et al. “Spin and orbital angular momentum structure of Cu (111) and Au (111) surface states”. In: *Physical Review B* 85.19 (2012), p. 195402.

[64] Gene Dresselhaus. "Spin-orbit coupling effects in zinc blende structures". In: *Physical Review* 100.2 (1955), p. 580.

[65] Liang Fu and Charles L Kane. "Topological insulators with inversion symmetry". In: *Physical Review B* 76.4 (2007), p. 045302.

[66] Liang Fu, Charles L Kane, and Eugene J Mele. "Topological insulators in three dimensions". In: *Physical review letters* 98.10 (2007), p. 106803.

[67] MG Vergniory et al. "A complete catalogue of high-quality topological materials". In: *Nature* 566.7745 (2019), pp. 480–485.

[68] Yuqi Xia et al. "Observation of a large-gap topological-insulator class with a single Dirac cone on the surface". In: *Nature physics* 5.6 (2009), pp. 398–402.

[69] David Hsieh et al. "A topological Dirac insulator in a quantum spin Hall phase". In: *Nature* 452.7190 (2008), pp. 970–974.

[70] Anne Barfuss et al. "Elemental topological insulator with tunable Fermi level: Strained α-Sn on InSb (001)". In: *Physical review letters* 111.15 (2013), p. 157205.

[71] Liang Fu. "Topological crystalline insulators". In: *Physical Review Letters* 106.10 (2011), p. 106802.

[72] Y Tanaka et al. "Experimental realization of a topological crystalline insulator in SnTe". In: *Nature Physics* 8.11 (2012), pp. 800–803.

[73] Robert Karplus and JM Luttinger. "Hall effect in ferromagnetics". In: *Physical Review* 95.5 (1954), p. 1154.

[74] Mikhail I D'Yakonov and VI Perel. "Possibility of orienting electron spins with current". In: *Soviet Journal of Experimental and Theoretical Physics Letters* 13 (1971), p. 467.

[75] JE Hirsch. "Spin hall effect". In: *Physical review letters* 83.9 (1999), p. 1834.

[76] Yuichiro K Kato et al. "Observation of the spin Hall effect in semiconductors". In: *science* 306.5703 (2004), pp. 1910–1913.

[77] J-C Rojas-Sánchez et al. "Spin pumping and inverse spin Hall effect in platinum: the essential role of spin-memory loss at metallic interfaces". In: *Physical review letters* 112.10 (2014), p. 106602.

[78] Luqiao Liu et al. "Spin-torque switching with the giant spin Hall effect of tantalum". In: *Science* 336.6081 (2012), pp. 555–558.

[79] Qiang Hao, Wenzhe Chen, and Gang Xiao. "Beta (β) tungsten thin films: Structure, electron transport, and giant spin Hall effect". In: *Applied Physics Letters* 106.18 (2015), p. 182403.

[80] Jairo Sinova et al. "Universal intrinsic spin Hall effect". In: *Physical review letters* 92.12 (2004), p. 126603.

[81] Axel Hoffmann. "Spin Hall effects in metals". In: *IEEE transactions on magnetics* 49.10 (2013), pp. 5172–5193.

[82] J Smit. "The spontaneous Hall effect in ferromagnetics I". In: *Physica* 21.6-10 (1955), pp. 877–887.

[83] Luc Berger. "Side-jump mechanism for the Hall effect of ferromagnets". In: *Physical Review B* 2.11 (1970), p. 4559.

[84] Sergey D Ganichev et al. "Spin-galvanic effect". In: *Nature* 417.6885 (2002), pp. 153–156.

[85] Pietro Gambardella and Ioan Mihai Miron. "Current-induced spin–orbit torques". In: *Philosophical Transactions of the Royal Society A: Mathematical, Physical and Engineering Sciences* 369.1948 (2011), pp. 3175–3197.

[86] JC Rojas Sánchez et al. "Spin-to-charge conversion using Rashba coupling at the interface between non-magnetic materials". In: *Nature communications* 4.1 (2013), pp. 1–7.

[87] Pan He et al. "Bilinear magnetoelectric resistance as a probe of three-dimensional spin texture in topological surface states". In: *Nature Physics* 14.5 (2018), pp. 495–499.

[88] Steven S-L Zhang and Giovanni Vignale. "Theory of bilinear magneto-electric resistance from topological-insulator surface states". In: *Spintronics XI*. Vol. 10732. International Society for Optics and Photonics. 2018, p. 1073215.

[89] Anna Dyrdał, Józef Barnaś, and A Fert. "Spin-Momentum-Locking Inhomogeneities as a Source of Bilinear Magnetoresistance in Topological Insulators". In: *Physical review letters* 124.4 (2020), p. 046802.

[90] Pan He et al. "Observation of out-of-plane spin texture in a SrTiO 3 (111) two-dimensional electron gas". In: *Physical review letters* 120.26 (2018), p. 266802.

[91] T Guillet et al. "Observation of large unidirectional Rashba magnetoresistance in Ge (111)". In: *Physical review letters* 124.2 (2020), p. 027201.

[92] Yuejie Zhang et al. "Large Magneto-Electric Resistance in the Topological Dirac Semimetal alpha Sn". In: *arXiv preprint arXiv:2107.03472* (2021).

[93] Diogo Castro Vaz et al. "Determining the Rashba parameter from the bilinear magnetoresistance response in a two-dimensional electron gas". In: *Physical Review Materials* 4.7 (2020), p. 071001.

[94] Yan Li et al. "Nonreciprocal charge transport up to room temperature in bulk Rashba semiconductor α-GeTe". In: *Nature communications* 12.1 (2021), pp. 1–8.

[95] Arne Brataas, Yu V Nazarov, and Gerrit EW Bauer. "Finite-element theory of transport in ferromagnet–normal metal systems". In: *Physical Review Letters* 84.11 (2000), p. 2481.

[96] VP Amin and MD Stiles. "Spin transport at interfaces with spin-orbit coupling: Phenomenology". In: *Physical Review B* 94.10 (2016), p. 104420.

[97] Can Onur Avci et al. "Interplay of spin-orbit torque and thermoelectric effects in ferromagnet/normal-metal bilayers". In: *Physical Review B* 90.22 (2014), p. 224427.

[98] Kevin Garello et al. "Symmetry and magnitude of spin–orbit torques in ferromagnetic heterostructures". In: *Nature nanotechnology* 8.8 (2013), pp. 587–593.

[99] Bernard Dieny et al. "Opportunities and challenges for spintronics in the microelectronics industry". In: *Nature Electronics* 3.8 (2020), pp. 446–459.

[100] Qiming Shao et al. "Roadmap of spin-orbit torques". In: *IEEE Transactions on Magnetics* (2021).

[101] Eva Grimaldi et al. "Single-shot dynamics of spin–orbit torque and spin transfer torque switching in three-terminal magnetic tunnel junctions". In: *Nature nanotechnology* 15.2 (2020), pp. 111–117.

[102] Hao Wu et al. "Room-temperature spin-orbit torque from topological surface states". In: *Physical review letters* 123.20 (2019), p. 207205.

[103] Aaron D LaLonde et al. "Lead telluride alloy thermoelectrics". In: *Materials today* 14.11 (2011), pp. 526–532.

[104] KL Chopra and SK Bahl. "Amorphous versus crystalline GeTe films. I. Growth and structural behavior". In: *Journal of Applied Physics* 40.10 (1969), pp. 4171–4178.

[105] SK Bahl and KL Chopra. "Amorphous versus crystalline GeTe films. III. Electrical properties and band structure". In: *Journal of Applied Physics* 41.5 (1970), pp. 2196–2212.

[106] Takayuki Kato and Keiji Tanaka. "Electronic properties of amorphous and crystalline Ge2Sb2Te5 films". In: *Japanese journal of applied physics* 44.10R (2005), p. 7340.

[107] H-S Philip Wong et al. "Phase change memory". In: *Proceedings of the IEEE* 98.12 (2010), pp. 2201–2227.

[108] Marcus Liebmann et al. "Giant Rashba-Type Spin Splitting in Ferroelectric GeTe (111)". In: *Advanced Materials* 28.3 (2016), pp. 560–565.

[109] Volker L Deringer, Marck Lumeij, and Richard Dronskowski. "Ab initio modeling of α-GeTe (111) surfaces". In: *The Journal of Physical Chemistry C* 116.29 (2012), pp. 15801–15811.

[110] J Goldak et al. "Structure of alpha GeTe". In: *The Journal of Chemical Physics* 44.9 (1966), pp. 3323–3325.

[111] Zaiyao Fei et al. “Ferroelectric switching of a two-dimensional metal”. In: *Nature* 560.7718 (2018), pp. 336–339.

[112] Evgeny Plekhanov et al. “Engineering relativistic effects in ferroelectric SnTe”. In: *Physical Review B* 90.16 (2014), p. 161108.

[113] Kai Liu et al. “Intrinsic origin of enhancement of ferroelectricity in SnTe ultrathin films”. In: *Physical review letters* 121.2 (2018), p. 027601.

[114] KLI Kobayashi et al. “Carrier-concentration-dependent phase transition in SnTe”. In: *Physical Review Letters* 37.12 (1976), p. 772.

[115] Masashi Iizumi et al. “Phase transition in SnTe with low carrier concentration”. In: *Journal of the Physical Society of Japan* 38.2 (1975), pp. 443–449.

[116] Na Wang et al. “Microscopic origin of the p-type conductivity of the topological crystalline insulator SnTe and the effect of Pb alloying”. In: *Physical Review B* 89.4 (2014), p. 045142.

[117] Kai Chang et al. “Discovery of robust in-plane ferroelectricity in atomic-thick SnTe”. In: *Science* 353.6296 (2016), pp. 274–278.

[118] Walther Gerlach and Otto Stern. “Der experimentelle nachweis der richtungsquantelung im magnetfeld”. In: *Zeitschrift für Physik* 9.1 (1922), pp. 349–352.

[119] Walther Gerlach and Otto Stern. “Das magnetische moment des silberatoms”. In: *Zeitschrift für Physik* 9.1 (1922), pp. 353–355.

[120] Nevill Francis Mott. “The scattering of fast electrons by atomic nuclei”. In: *Proceedings of the Royal Society of London. Series A, Containing Papers of a Mathematical and Physical Character* 124.794 (1929), pp. 425–442.

[121] Joachim Kessler. *Polarized electrons*. Vol. 1. Springer Science & Business Media, 1985.

[122] Joachim Stöhr and Hans Christoph Siegmann. “Magnetism”. In: *Solid-State Sciences. Springer, Berlin, Heidelberg* 5 (2006).

[123] DL Abraham and H Hopster. “Spin-polarized electron-energy-loss spectroscopy on Ni”. In: *Physical review letters* 62.10 (1989), p. 1157.

[124] Wolfgang Weber et al. “Spin motion of electrons during reflection from a ferromagnetic surface”. In: *Physical Review B* 66.10 (2002), p. 100405.

[125] Timothy J Gay and FB Dunning. “Mott electron polarimetry”. In: *Review of scientific instruments* 63.2 (1992), pp. 1635–1651.

[126] Noah Sherman. “Coulomb scattering of relativistic electrons by point nuclei”. In: *Physical Review* 103.6 (1956), p. 1601.

[127] HA Tolhoek. “Electron polarization, theory and experiment”. In: *Reviews of modern physics* 28.3 (1956), p. 277.

[128] J Kessler. “Electron spin polarization by low-energy scattering from unpolarized targets”. In: *Reviews of Modern Physics* 41.1 (1969), p. 3.

[129] Riccardo Bertacco and Franco Ciccacci. “Oxygen-induced enhancement of the spin-dependent effects in electron spectroscopies of Fe (001)”. In: *Physical Review B* 59.6 (1999), p. 4207.

[130] Y Lassailly et al. “Spin-dependent transmission of low-energy electrons through ultrathin magnetic layers”. In: *Physical Review B* 50.17 (1994), p. 13054.

[131] N Rougemaille et al. “Spin-dependent electron transport in ferromagnetic bilayers: Application to three-dimensional spin detectors”. In: *Journal of applied physics* 91.10 (2002), pp. 8408–8410.

[132] Henri-Jean Drouhin and Nicolas Rougemaille. “Spin filtering in ferromagnetic bilayers”. In: *Journal of applied physics* 91.12 (2002), pp. 9948–9951.

[133] Ruining Wang et al. “Toward truly single crystalline GeTe films: The relevance of the substrate surface”. In: *The Journal of Physical Chemistry C* 118.51 (2014), pp. 29724–29730.

[134] Riccardo Bertacco et al. "Epitaxial growth and characterization of layered magnetic nanostructures". In: *Applied surface science* 252.5 (2005), pp. 1754–1764.

[135] Matteo Cantoni and Riccardo Bertacco. "High efficiency apparatus for spin polarized inverse photoemission". In: *Review of scientific instruments* 75.7 (2004), pp. 2387–2392.

[136] Milton Ohring. *Materials science of thin films*. Elsevier, 2001.

[137] C Grant Willson, Ralph R Dammel, and Arnost Reiser. "Photoresist materials: a historical perspective". In: *Metrology, Inspection, and Process Control for Microlithography XI*. Vol. 3050. International Society for Optics and Photonics. 1997, pp. 38–51.

[138] Marc J Madou. *Fundamentals of microfabrication: the science of miniaturization*. CRC press, 2018.

[139] Hans Lüth. *Solid surfaces, interfaces and thin films*. Vol. 4. Springer, 2001.

[140] M Pl Seah and WA Dench. "Quantitative electron spectroscopy of surfaces: A standard data base for electron inelastic mean free paths in solids". In: *Surface and interface analysis* 1.1 (1979), pp. 2–11.

[141] Baiqing Lv, Tian Qian, and Hong Ding. "Angle-resolved photoemission spectroscopy and its application to topological materials". In: *Nature Reviews Physics* 1.10 (2019), pp. 609–626.

[142] Grant R Fowles. *Introduction to modern optics*. Courier Corporation, 1989.

[143] Daniel T Pierce et al. "The GaAs spin polarized electron source". In: *Review of Scientific Instruments* 51.4 (1980), pp. 478–499.

[144] Yusuke Tanaka et al. "Two types of Dirac-cone surface states on the (111) surface of the topological crystalline insulator SnTe". In: *Physical Review B* 88.23 (2013), p. 235126.

[145] Chen-Hui Yan et al. "Growth of topological crystalline insulator SnTe thin films on Si (111) substrate by molecular beam epitaxy". In: *Surface science* 621 (2014), pp. 104–108.

[146] Mahmood Hassan et al. "Molecular beam epitaxy of single phase GeMnTe with high ferromagnetic transition temperature". In: *Journal of crystal growth* 323.1 (2011), pp. 363–367.

[147] Frédéric Bonell et al. "Growth of twin-free and low-doped topological insulators on BaF2 (111)". In: *Crystal Growth & Design* 17.9 (2017), pp. 4655–4660.

[148] Changgu Lee et al. "Measurement of the elastic properties and intrinsic strength of monolayer graphene". In: *science* 321.5887 (2008), pp. 385–388.

[149] S Ikeda et al. "A perpendicular-anisotropy CoFeB–MgO magnetic tunnel junction". In: *Nature materials* 9.9 (2010), pp. 721–724.

[150] H Sato et al. "Perpendicular-anisotropy CoFeB-MgO magnetic tunnel junctions with a MgO/-CoFeB/Ta/CoFeB/MgO recording structure". In: *Applied Physics Letters* 101.2 (2012), p. 022414.

[151] OL Blakslee et al. "Elastic constants of compression-annealed pyrolytic graphite". In: *Journal of applied physics* 41.8 (1970), pp. 3373–3382.

[152] Can Onur Avci et al. "Unidirectional spin Hall magnetoresistance in ferromagnet/normal metal bilayers". In: *Nature Physics* 11.7 (2015), pp. 570–575.

[153] Pan He et al. "Nonlinear planar Hall effect". In: *Physical review letters* 123.1 (2019), p. 016801.

[154] Lukas Neumann and Markus Meinert. "Influence of the Hall-bar geometry on harmonic Hall voltage measurements of spin-orbit torques". In: *AIP Advances* 8.9 (2018), p. 095320.

[155] AA Taskin et al. "Planar Hall effect from the surface of topological insulators". In: *Nature communications* 8.1 (2017), pp. 1–7.

[156] T Ideue et al. "Bulk rectification effect in a polar semiconductor". In: *Nature Physics* 13.6 (2017), pp. 578–583.

[157] Luis M Vicente-Arche et al. "Spin–charge interconversion in KTaO3 2D electron gases". In: *Advanced Materials* 33.43 (2021), p. 2102102.